Graphene on Metal Surfaces and Hexagonal Boron Nitride

Dissertation

zur

Erlangung der naturwissenschaftlichen Doktorwürde
(Dr. sc. nat.)

vorgelegt der

Mathematisch-naturwissenschaftlichen Fakultät

der

Universität Zürich

von

Silvan Roth
von Buchholterberg (BE)

Promotionskomitee

Prof. Dr. Jürg Osterwalder
Prof. Dr. Thomas Greber
Dr. Oliver Gröning

Zürich 2013

Abstract

In this thesis, procedures for chemical vapor deposition growth of graphene on rhodium and on hexagonal-boron nitride were developed. The systems were further characterized by angular resolved photoemission spectroscopy and scanning tunneling microscopy.

A single atomic layer of graphite, so called graphene has gathered a lot of attention nowadays. Due to its high carrier mobility it has great potential for future electronics. Another application for graphene is related to its chemical inertness. It can serve as template for single molecule deposition.
With these applications in mind, it is necessary to find suitable production methods to fabricate high quality, large scale graphene. Among various fabrication methods, chemical vapor deposition has turned out to be a possible route to meet the demanded criteria of graphene fabrication. The growth and characterization of graphene on Rh(111) and hexagonal-boron nitride are the content of this thesis.
Graphene grown by chemical vapor deposition of 3-pentanone on Rh(111) leads to a largescale, uniform growth of graphene. A unique corrugation of the graphene layer is observed, which contains three depressions and a hill site within the unit cell. These three pockets have a diameter of roughly 1 nm and have therefore high potential to act as adsorption sites for single molecules.
In contrast to the strongly bonded graphene on Rh(111), graphene on h-BN shows weak interaction with the substrate. Growing graphene on h-BN demands different process parameters, since the metal surface is passivated by the h-BN layer, i. e. it requires higher activation energy (temperature) and higher pressure.
The bonding of graphene to the h-BN/Cu(111) is weak enough, that the graphene and the h-BN layer keep their intrinsic lattice constant during the formation which differs by 1.6%. This results in formation of a large moiré pattern with a lattice constant of 15.4 nm. The mismatch is also represented in the electronic band structure,where two Brillouin zones of different diameter are found for the two layers.

The corrugated h-BN nanomesh on Rh(111) as a substrate for graphene formation exhibits a unique behavior during the formation process. Other than in the case of h-BN/Cu(111), the h-BN layer here undergoes a change during the graphene formation process. An intercalation of carbon between the h-BN layer and Rh and a diffusion of carbon into the Rh bulk leads to a weakening of the bonding and the h-BN layer looses its corrugated nanomesh character. In a second CVD process, graphene can be grown on this flat h-BN substrate.

Zusammenfassung

In dieser Arbeit wurden Verfahrwen für chemische Gasphasenabscheidung von Graphene auf Rhodium und auf hexagonalem Bornitrid entwickelt. Die Systeme wurden durch winkelaufgelöste Photoemissionsspektroskopie und Rastertunnelmikroskopie charakterisiert.

Eine einzige Atomlage Graphit, genannt Graphen, hat eine Menge Aufmerksamkeit in den letzten Jahren erhalten. Aufgrund seiner hohen Ladungsträgermobilität hat es ein grosses Potenzial für Elektronikbauteile der Zukunft. Eine weitere Anwendung für Graphen führt auf seine chemische Inertheit zurück. Es kann als Unterlage für die Ablagerung einzelner Moleküle dienen. Mit Hinblick auf diese Anwendungen ist es notwendig, geeignete Herstellungsverfahren zu finden, um qualitativ hochwertiges, grossflächiges Graphen herzustellen. Unter den verschiedenen Herstellungsverfahren, hat sich die chemische Gasphasenabscheidung als ein möglicher Weg erwiesen. Das Wachstum und die Charakterisierung von Graphen auf Rh(111) und hexagonalem - Bornitrid sind der Inhalt dieser Arbeit.

Chemische Gasphasenabscheidung unter Verwendung von 3-Pentanon auf Rh(111) führt zu einem grossen und gleichmässigen Wachstum von Graphen. Eine einzigartige Korrugation der Graphenschicht wird beobachtet, welche drei Vertiefungen und einen Hügel in ihrer Einheitszelle aufweist. Diese drei Mulden haben einen Durchmesser von etwa 1 nm und könnten daher als Adsorptionsstellen für einzelne Moleküle dienen.
Im Gegensatz zum stark gebundenen Graphen auf Rh(111), zeigt Graphen auf h-BN weniger Interaktion mit dem Substrat. Das wachsen von Graphen auf h-BN verlangt unterschiedliche Prozessparameter, da die Metalloberfläche durch die h-BN Schicht passiviert wird. Das Wachstum benötigt höhere Aktivierungsenergie (Temperatur) und höheren Druck.
Die Bindung von Graphen zum h-BN/Cu(111) Substrat ist schwach genug, dass die Graphen- und die h-BN Schicht ihre intrinsische Gitterkonstante beibehalten während des Wachstums, welche sich um 1.6% unterscheidet. Dies führt zur Bildung eines grossen Moirémusters mit einer Gitterkonstanten von 15.4 nm. Diese Fehlanpassung wiederspiegelt sich auch in der elektronischen Bandstruktur, dies fürt zu zwei Brillouin Zonen unterschiedlichen Durchmessers für die beiden Schichten.
Graphen auf dem korrugierten h-BN Nanomesh Substrat weist eine einzigartiges Verhalten während des Bildungsprozesses auf. Im Gegensatz zu h-BN/Cu(111) erfährt das h-BN Substrat eine Änderung während des Graphen Entstehungsprozesses. Eine Interkallation von Kohlenstoff zwischen der h-BN Schicht und Rh führt zu einer Schwächung der Bindung wodurch die h-BN Schicht ihren korrugierten Nanomesh Charakter verliert. In einem zweiten CVD-Verfahren, kann Graphen auf diesem flachen h-BN Substrat gewachsen werden.

Contents

Chapter 1

Motivation

The complexity modern technology constantly demands faster electronics and larger amount of memory. Conventional silicon based electronics still dominate the present markets. However, its capability is limited. For further improvements, new materials are desired, with new electronic properties. Graphene based electronics may offer a possibility to new electronics, which are faster and therefore have great potential in the future [1, 2]. The mobility of electrons in few layer graphene was found to be up to $15,000 cm^2/Vs$ at 300 K [3]. This value is about ten times higher than the values found for doped silicon [4]. Further it was found that the mobility in these graphene flakes does not depend on temperature, which leads to the conclusion that scattering on defects is still the dominant limitation in graphene electron transport. To further improve graphene based electronics, and to make fully use of intrinsic properties of graphene, it is essential to reduce the defect density.

In order for graphene to be used on a regular base, production methods are required which deliver high quality graphene sheets with a reasonable yield. Depending on the substrate, many different routes for graphene fabrications are possible, such as exfoliation from graphite [3], carbon segregation from bulk materials [5], catalytic chemical vapor deposition on various metals [6], and non catalytic growth on dielectric substrates Oshima2000. The goal is to develop growth methods for high quality graphene, which can be upscaled to high quantity fabrication, and therefore open the door for graphene to be used as a standard material in future technology.

Chapter 2

Introduction

2.1 sp^2-bond networks

sp^2 hybridization describes a chemical bond between atoms where one s-orbital hybridizes with two p-orbitals. This results in a planar trigonal bond geometry with a separation angle of 120° [7]. The most famous representative from this group is the benzene (C_6H_6) molecule, which is the building block of graphite. The three sp^2-orbitals of each C-atom overlap with the sp^2-orbitals from the neighboring C-atoms, and form so called σ-bonds. The remaining valence electron is not playing a role in this σ-bond system, but remains in a π-orbital perpendicular to the molecules plane. These orbitals from the three adjacent C-atoms overlap and form a highly delocalized electron state, the π-system, which spans over the entire plane. In Fig. 2.1, the geometry of the atomic orbitals is illustrated on a schematic benzene molecule.

2.1.1 Graphite

As mentioned above, sp^2-hybridized systems can exist over large areas, forming large honeycomb networks. Such planes can be found stacked above each other, and form large three dimensional structures such as graphite. The inter-plane bonding in graphite is of van der Waals type, and therefore weak compared to the covalent in-plane bonds, which makes graphite a soft material, often used as lubricant. The inter-plane distance of graphite is found to be 3.3 Å[8]. Due to the extended π-orbitals, which exhibit high electron mobility, graphite is an excellent electric conductor in the in-plane direction. The out of plane conductance of graphite is rather low.

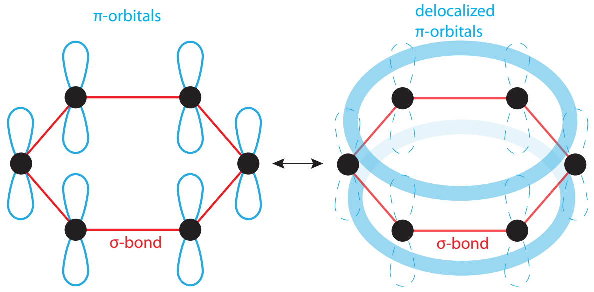

Figure 2.1: $sp^2 - orbitals$ Primitive building block of a sp^2-hybridized electron system. The atoms s- and p-orbitals form the in-plane σ-bonds, while the out of plain p-orbitals form a delocalized π-orbital system.

Hexagonal Boron Nitride

Similar to graphite, where the honeycomb lattice is build from carbon atoms is hexagonal-Boron Nitride (h-BN). In an alternating fashion, boron and nitrogen atoms form a similar sp^2 hybridized system. Due to the different electron affinity of boron and nitrogen, the bonds are less symmetric then in graphite. The two non-equivalent atoms in the unit cell lead to different electronic properties than in graphite, i. e. the material becomes insulating (see Sec. 2.2).
The building block for h-BN is Borazine $(HBNH)_3$, a hexagonal molecule consisting of B and N atoms in its central ring structure.

2.2 Graphene

Since Graphite consists of single layer honeycomb carbon planes, one can imagine that it is possible to isolate a single layer from bulk graphite. This idea however was believed to be in contradiction to the theory of Landau, published 1937 [9]. Misinterpreting this work leads to the conclusion of strictly two dimensional materials being thermodynamically unstable. Therefore it was believed that such a material in it's free standing form does no exist. Nevertheless in 1946, Wallace calculated the electronic band structure of graphite and graphene for the first time using a tight binding model [10]. A detailed analysis of the theoretical band structure model will be introduced later in this thesis (see Sec. 2.2). Even though the band structure of graphene was theoretically described, it was not mentioned further that the linear dispersion around the $\overline{K}-$point of graphene leads directly to zero-effective-mass electrons. This unique feature was described first by DiVincenzo and Mele 1984 [11]. Experimentally, a first preparation and characterization of a single layer graphene, grown on Lanthanum Hexaboride (100) was already realized by Oshima and co-workers [12] at that time. By that time, single layer carbon was still treated as an unwanted contamination on clean surfaces. Further investigation of the this addlayers properties were not of interest at that time.

Lately graphene gained interest again, when Geim and co-workers in 2004 reported the isolation off few layer graphene from bulk graphite [3]. By using scotch tape to peel of layers from bulk graphite, and further repeating this step, to make the layers thinner and thinner, single and few layer graphene flakes were produced. Measurements showed for the first time that this graphene had the properties of a two dimensional structure, not behaving like a three dimensional material anymore.
The unique properties of graphene are directly related to the linear electron band dispersion around the $\overline{K}$ point of the Brillouin zone. In the following paragraph, the derivation of the band structure is explained.

Band structure of Graphene

A first description of the band structure of graphene dates back to 1946 by Wallace [10]. A tight binding approach was used to solve the Schrödinger equation

$$H\,\Psi = E\,\Psi \tag{2.1}$$

The graphene honeycomb structure as shown in Fig. 2.2 contains two hexagonal sub-lattices A and B, with carbon atoms C_A and C_B, respectively. The primitive lattice vectors can be defined as

$$a_1 = \left(\frac{\sqrt{3}a}{2}, \frac{a}{2}\right), a_2 = \left(\frac{\sqrt{3}a}{2}, -\frac{a}{2}\right) \tag{2.2}$$

which leads to the reciprocal lattice vectors

$$b_1 = \left(\frac{2\pi}{\sqrt{3}a}, \frac{2\pi}{a}\right), b_2 = \left(\frac{2\pi}{\sqrt{3}a}, -\frac{2\pi}{a}\right). \tag{2.3}$$

The bond length for the covalent C-C bond in graphite is 1.42 Å. The lattice constant of the hexagonal lattice is therefore 2.46 Å.
The simple Hamiltonian below can be used to describe a hexagonal lattice. It consists of four terms of which two are equal. The terms H_{AA} and H_{BB} describe the energies of the according sub-lattices, while the H_{AB} terms describe the interference of the two sub-lattices.

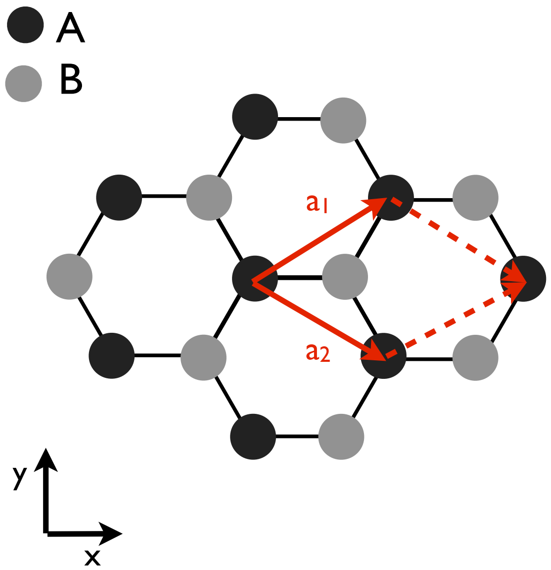

Figure 2.2: **graphene lattice** Schematic illustration of a hexagonal graphene lattice with two hexagonal sub-lattices A (black) and B (gray). The unit cell with the primitive lattice vectors a_1 and a_2 is shown in red.

$$H = \begin{pmatrix} H_{AA} & H_{AB} \\ H_{AB} & H_{BB} \end{pmatrix} \tag{2.4}$$

The Eigenvalue problem

$$\begin{pmatrix} H_{AA} & H_{AB} \\ H_{AB} & H_{BB} \end{pmatrix} \Psi = E\,\mathbb{I}\,\Psi \tag{2.5}$$

connected with this Hamiltonian leads to the Eq.

$$det \begin{pmatrix} H_{AA} - E & H_{AB} \\ H_{AB} & H_{BB} - E \end{pmatrix} = 0 \tag{2.6}$$

The solution of this equation returns the well known graphene band structure

$$E(k)\pm = \pm\sqrt{\gamma_0^2(1 + 4\,cos^2\frac{k_y a}{2} + 4\,cos\frac{k_y a}{2} + 4\,cos\frac{k_x\sqrt{3}a}{2})} \tag{2.7}$$

with the bonding π-band E_- and the anti bonding π^*- band E_+.
The two $\pi-$bands (π and π^*) meet in the six distinct high symmetry $\overline{K}$ points of the Brillouin zone. The bands around the intersection point have the shape of two opposing

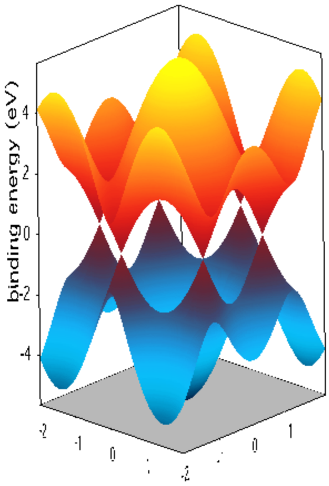

Figure 2.3: **Graphene band structure** Tight binding model for the $\pi-$ band of graphene. The lower $\pi-$band (blue) and the upper π^*-band (red) meet in the six Dirac points.

cones, so-called Dirac cones. The six intersections are called the Dirac points. Around the Dirac point, the energy dispersion relation $E(\mathbf{k})$ is a linear function. The matrix elements of Eq. 2.6 can easily be related to the properties of graphene. The terms $H_{AA} - E$ and $H_{BB} - E$ are the energies of the sublattices E_A and E_B. Due to symmetry of the two sublattices, there is no difference in the energies E_A and E_B at the $\overline{K}$, meaning

$$E_A - E_B = 0. \tag{2.8}$$

However, this is only the case, when the graphene layer is free standing and does not experience any external perturbation. If an additional perturbation acts on the graphene layer, such that the symmetry is broken between the two sublattices, $E_A - E_B$ is no longer zero. The difference of the two sublattice energies now defines a band gap

$$E_A - E_B = E_g. \tag{2.9}$$

The band gap E_g increases as the asymmetry of the sublattices gets larger.

Such a sublattice asymmetry can be induced in graphene by its supporting substrate. The lattice mismatch between graphene and nickel on the (111) surface is small ($a_g = 2.46$ Å, $a_{Ni(111)} = 2.49$ Å), which allows the graphene layer to adopt the lattice constant of the substrate, and forming a (1×1) structure [13]. The p_z-orbitals of one of the graphenes sublattice C-atoms overlap and start to hybridize with the Ni $3d-$orbitals. This leads to a lowering of the energy of the $\pi-$band of graphene. A graphene layer grown on the Ni(111) surface therefore exhibits a band gap as large as 3 eV [14]. The in-plane $\sigma-$bands are not effected by this hybridization and therefore remain at their original energy level.

2.3 Photoelectron Spectroscopy

2.3.1 The Photoelectric Effect

Photoelectron Spectroscopy is based on the photoelectric effect, which was first discovered by Heinrich Hertz in 1887 [15]. Since then, photoemission spectroscopy has developed into a powerful tool for surface analysis. The phenomena of electrons being emitted from a metal surface when exposed to radiation of high energetic light remained unexplained until 1905 when Albert Einstein published his work about the quantization of light [16]. It was understood that electrons absorb defined quanta of light, photons, and can therefore overcome the workfunction of the metal surface and be photoemitted from the metal. The photoelectric effect is nowadays used to investigate the electronic structure of materials. The kinetic energy of the emitted electrons is described by the Equation:

$$E_{kin} = h\nu - \Phi - |E_b| \tag{2.10}$$

where $h\nu$ is the energy of the photon, Φ the workfunction, and E_b the binding energy of the electron's initial state. While the workfunction and the photon energy are known quantities in a photoemission experiment, measuring the kinetic energy of the photoelectrons leads directly to the binding energy of the emitted electrons.

This allows us to calculate the initial energy E_i which the electron has in its initial state $|\Psi_i\rangle$ inside the solid. The transition to a final state $|\Psi_f\rangle$ is described by Schrödinger's equation

$$-\frac{\hbar^2}{2m} \triangle \Psi + V\Psi = i\hbar\frac{\delta\Psi}{\delta t} \tag{2.11}$$

The Hamiltonian can be written as

$$H = -\frac{1}{2m}((\frac{\hbar}{i} \bigtriangledown - \frac{e}{c}\mathbf{A})^2 + V) \tag{2.12}$$

Assuming the Hamiltonian H to be separable into an unperturbed part H_0 and an interaction term H_{int}, it can be written as

$$H_0 = -\frac{\hbar^2}{2m} \triangle + V, \tag{2.13}$$

and

$$H'_{int} = -\frac{e\hbar}{imc}\mathbf{A}\bigtriangledown = -\frac{e}{mc}\mathbf{A}\cdot\mathbf{p}. \tag{2.14}$$

Fermi's Golden Rule then describes the transition rate W_{if} from the initial state Ψ_i to the final state Ψ_f via

$$W_{if} \propto \sum_{i,f} \frac{2\pi}{\hbar} \mid \langle\Psi_i| H'_{int} |\Psi_f\rangle \mid^2 \delta(E_f - E_i - h\nu). \tag{2.15}$$

The photoexcited electron in its final state Ψ_f can be treated approximately like a free electron, following the relation $E_F = \frac{\hbar^2 \mathbf{k}^2}{2m}$. The component of its k-vector parallel to the surface of the solid $\mathbf{k}_{\|}$ can be described as

$$\mathbf{k}_{\|} = \frac{1}{\hbar}\sqrt{2m_e E_{kin}}\sin\Theta. \tag{2.16}$$

Instrumentation

To determine the electronic structure of a material, i. e. the electron binding energies, one needs to measure the kinetic energies of a photoemitted electrons. A hemispherical electron analyzer as shown in Fig. 2.4 is one possibility to distinguish electrons by their kinetic energy. Electrons emitted from the sample travel through the analyzer which contains two concentric hemispherical metal plates, floated on different electrostatic potentials. Thus, the created electric field forces electrons on circular trajectories described by the Eq.

$$r = \frac{m \cdot v^2}{q \cdot E}. \tag{2.17}$$

In order to scan the kinetic energies of the detected electrons, a variable retarding potential is applied at the entrance to the analyzer, where the photoemitted electrons are retarded to the kinetic energy required to pass through the analyzer, (pass energy) Fig. 2.4.

A schematic illustration of the experimental setup can be seen in Fig. 2.5. A detailed description can be found elsewhere [17].

2.3.2 Ultraviolet and angle resolved photoemission spectroscopy

The photon energy range for UV light lies between 5 eV and 100 eV. High photon flux within a table top sized photon source can be established with a He discharge lamp. The He Iα (21.2 eV) and the He IIα (40.8 eV) excitation lines can be used to emit electrons from surfaces. With photons in this energy range, core levels of strongly bound electrons can not be accessed. On the other hand, loosely bound valance electrons can be photoemitted with UV light. Since these electrons are not strongly bound, they show $\mathbf{k}$ dependent dispersion, resulting from the band structure. Ultraviolet photoemission spectroscopy is an ideal tool to determine the electronic band structure of materials.

Fig. 2.6 shows a normal emission He I α ($h\nu$ =21.2 eV) photoemission spectrum of a clean Cu(111) surface. At a binding energy of 0.4 eV, the Cu surface state is visible. The high intensity peaks between 2 eV and 4 eV of binding energy are the d-bands of copper.

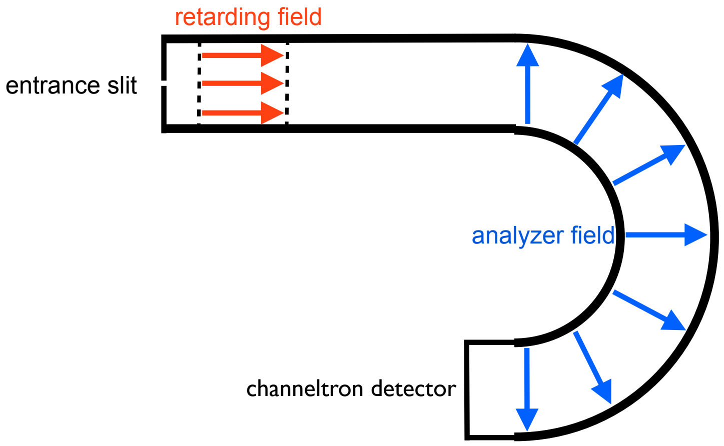

Figure 2.4: **Hemispherical electron analyzer** Schematic drawing of a hemispherical electrostatic electron analyzer. Electrons first pass through a retarding electric field, which can be varied when performing an energy scan. The retarded electrons travel between the two hemispheres through a radial electric field. The electric field and the radius in the analyzer defines the pass energy (kinetic energy of the electrons required to travel on a circular trajectory between the hemispheres) of the electrons.

2.3.3 X-Ray Photoemission Spectroscopy

Light with photon energies of 100 eV up to 10 keV are referred to as X-rays. Photoemission with X-ray excited photoelectrons, i.e. **X**-ray **P**hotoemission **S**pectroscopy (XPS) is sensitive for core level electrons. The binding energies of core levels are characteristic for each element. Therefore XPS has established itself to be a powerful tool to determine the composition of materials. When using X-rays with photon energies in the range between 1000 eV and 2000 eV (MgK_α : 1253.6 eV, AlK_α : 1486.6 eV) the inelastic mean free path of the excited electrons inside the material is limited and in the order of 1 nm - 2 nm. Therefore, only electrons from the top ten atomic layers can be emitted, which makes it the method of choice when investigating the chemical composition of surfaces. The surface sensitivity can be increased when the electrons are forced to travel longer distances inside the solid before being photoemitted. This can be achieved when measuring the electrons emitted at a large polar angle.

2.3.4 XPD

X-ray photoemission spectroscopy sheds light on the chemical composition of the top most layers of a sample. Combining this technique with the concept of the angular photoemission

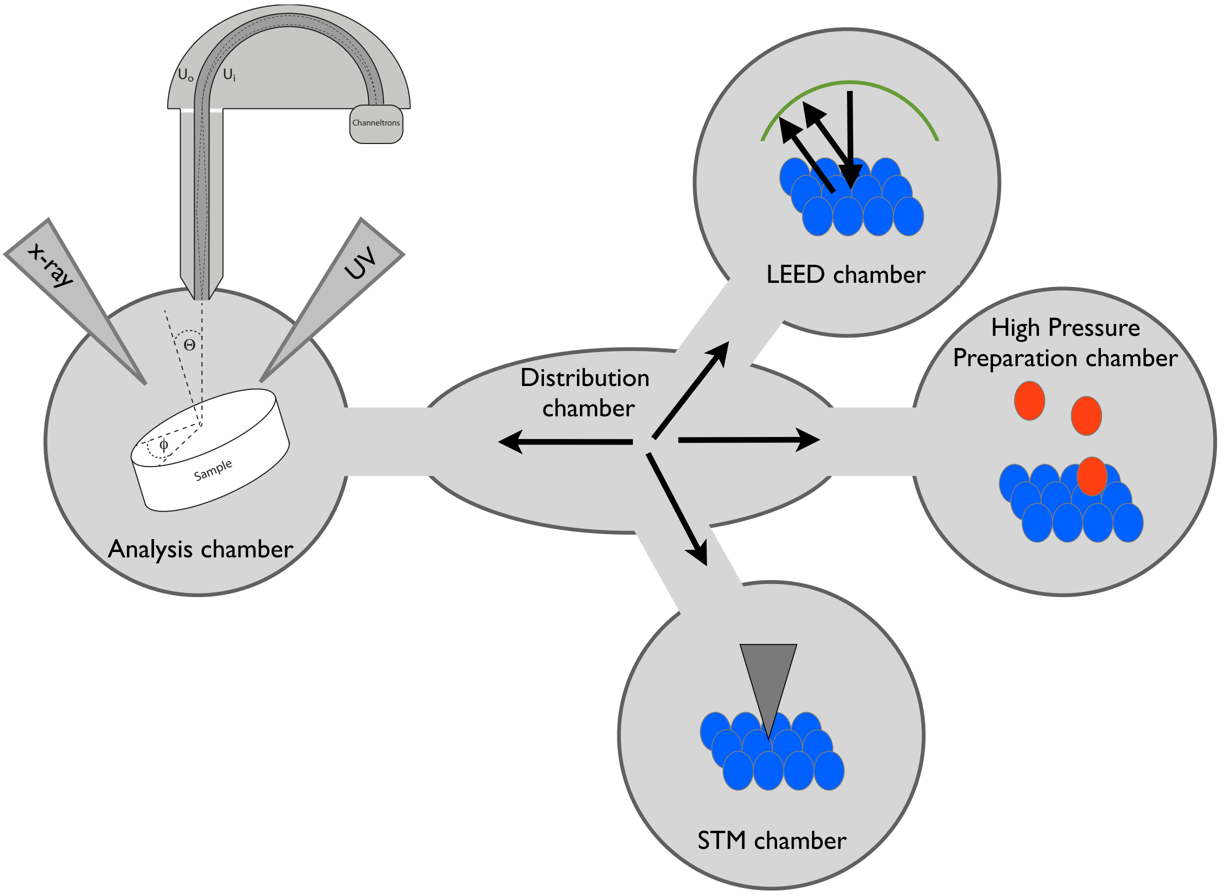

Figure 2.5: **Electron Spectrometer for Chemical Analysis** Schematic drawing of the ESCA setup used for the experiments. The instrument contains 5 main chambers. The analysis chamber, with a hemispherical electron analyzer and a 5 axis sample positioning system with three translation axes (x, y, z) and two rotational axes (θ polar angle, ϕ azimuthal angle). LEED chamber for low energy electron diffraction. A preparation chamber which allows pressures up to 2.5 mbar. A room temperature STM chamber with a Park Scientific STM. Via the distribution chamber, the samples can be moved under vacuum conditions from one chamber to another.

distribution can reveal details about the spacial ordering of the elements. This can be done by measuring the anisotropy of a core level photoemission over the whole hemisphere above the sample. The modulation in this signal is caused by diffraction of the initial wave of photoelectrons traveling through the crystal. At kinetic energies of the photoelectrons of hundreds of eV, the scattering amplitude of electron -atom scattering is highly anisotropic. An electron scattering off a neighboring atom is most likely to be scattered in the forward direction. Fig. 2.8 shows the Rh 3d 5/2 XPD pattern from a Rh(111) surface, under MgK$_\alpha$

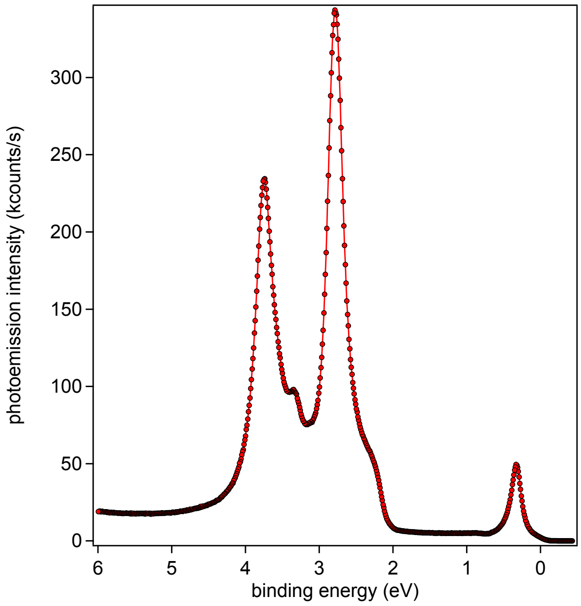

Figure 2.6: **UV photoemission spectrum** He Iα ($h\nu$ =21.2 eV) exited photoemission spectrum from a Cu(111) surface in normal emission. The spectrum is dominated by the copper d-bands between 2-4 eV binding energy. In addition the copper surface state at a binding energy of 0.4 eV is visible.

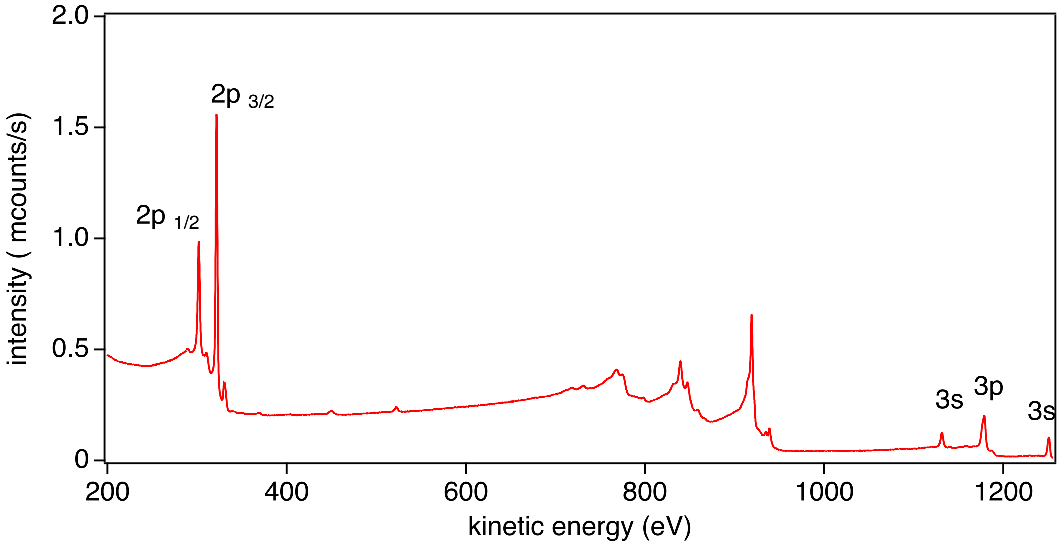

Figure 2.7: **X-ray Photoelectron Spectrum from Rh(111)** XPS spectrum of a Cu(111) surface under monochromatized AlK$_\alpha$ radiation.

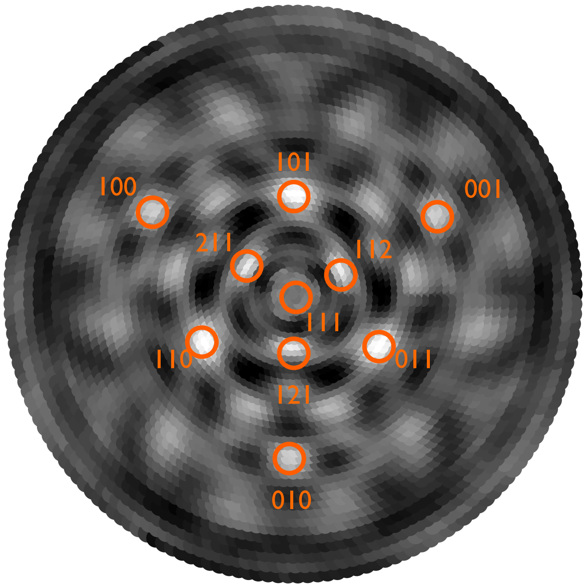

Figure 2.8: **X-ray Photoelectron Diffraction** Diffraction pattern of the Rh 3d 5/2 core level from Rh(111) with a kinetic energy of 943.5 eV, for polar angles between 0° to 82°. The data are displayed in a stereographic projection. The main scattering directions are indicated.

radiation.

2.4 STM

A complementary method to photoemission and photoelectron diffraction is Scanning Tunneling Microscopy (STM). The technique was invented by IBM researchers Gerd Binnig and Heinrich Rohrer [18] and later honoured with the Nobel price in physics in 1986. An atomically sharp metal tip is brought within tunneling distance to the sample surface. A voltage is applied between tip and sample. A small tunneling current can then be measured when the wave functions of the tip states and the sample states overlap. The tunneling current can be described as

$$I \propto e^{-2\sqrt{2m_e(V_b-E)/\hbar^2}d}, \tag{2.18}$$

where V_b is the height of the tunneling barrier, E the energy of the electrons, m_e the electron mass, and d the width of the tunneling barrier. The current therefore undergoes an exponential change with the distance d, which makes the method very sensitive to variations in heights. Fig. 2.9 shows a schematic setup of an STM. A control unit moves the tip via piezo electric crystals across the sample surface. The tunneling current is used in

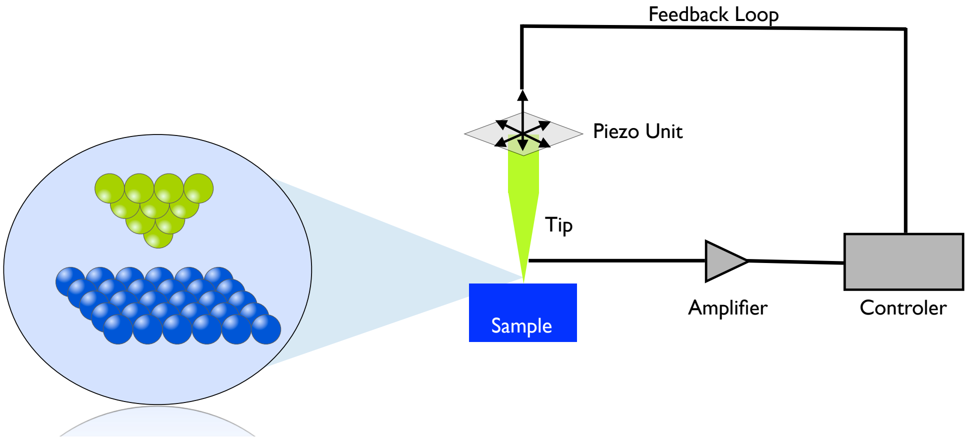

Figure 2.9: **Scanning Tunneling Microscope** Schematic setup of a STM. An atomically sharp tip is moved across the sample surface within the electron tunneling distance via a piezo unit. A voltage can be applied between tip and sample, which leads to a current. The tunneling current is amplified and recorded. The control unit sends a feedback signal to the piezo electric crystal unit, depending on the desired scan mode.

a feedback loop to control the distance between tip and sample. The STM can be run in two different modes. In a constant current mode, the tip height above the surface is varied in order to keep the tunneling current constant while scanning the tip across the surface. In the second mode, constant height mode, the absolute tip height is kept constant across the surface. Therefore the tunneling current changes and carries the information about the tunneling probability.

2.5 Photoemission on Graphene Layers

First photoemission experiments on graphene or monolayer graphite, respectively, were carried out by Himpsel et al. [19] in 1982, and Nagashima and co-workers in 1994 [14]. In the later, the graphene layer was grown by chemical vapor deposition of ethylene on a Ni(111) surface. The band dispersion of the graphene $\pi-$band showed a large gap of 3 eV at the $\overline{K}$ point of the Brillouin zone. The large band gap was assigned to the interaction of the graphene $\pi-$orbitals with the Ni $3d$ states. By intercalation of Alkali metals such as Na, Cs and K, the spacing and therefore the interaction between the overlayer and the metal substrate could be reduced, and a reduction of the band gap to 0.7 eV in the case of Cs was observed.

The same effect was observed for h-BN when the nickel substrate was replaced by weaker interacting metal substrates, such as Pd(111) and Pt(111) [20]. Further studies by Dedkov et al. have shown that by intercalation of Cu in the graphene/Ni interface, the interaction between graphene and the substrate is even further reduced [21]. A system with a very weak interaction of graphene and its substrate was shown for the first time by the group of Oshima and co-workers where they managed to grow and characterize a graphene layer on h-BN on Ni(111), [22, 23]. Due to the weak photoemission intensity of the graphene adlayer compared to the Ni $d-$bands around the $\overline{K}$ point, it was not possible to determine the band structure of the graphene layer around this region. Nevertheless it was concluded from the broadening of the LEED diffraction spots, that the graphene layer grows in an incommensurate fashion on h-BN/Ni(111). The energetically preferred incommensurate growth of the graphene layer is an indication of a very weak graphene/substrate interaction, since a stronger bonding would lead to a commensurate structure.

Besides graphene grown by the CVD technique on various substrates, graphene produced from thermal decomposition of the SiC(0001) surface has been intensively studied by photoelectron spectroscopy [24, 25, 26, 27, 28, 29]. It was found that the conical energy band dispersion is heavily distorted around the Dirac point. Coupling effects from electron-electron, electron-phonon and electron-plasmon interaction arise. At energies 200 meV below E_F the band structure exposes a kink, due to electron-phonon interaction.

Chapter 3

Synthesis of epitaxial Graphene on Rhodium from 3-Pentanone

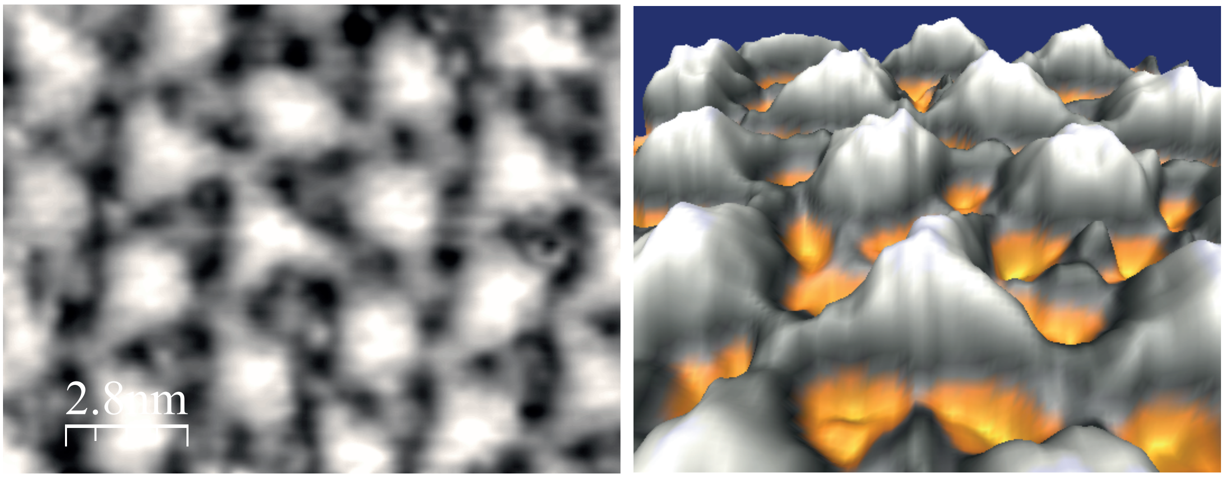

The Following Chapter is a modified version of the manuscript publishes in Surface Science:
S. Roth, J. Osterwalder, and T. Greber, *Synthesis of epitaxial Graphene on Rhodium from 3-Pentanone*, Surface Science **605**, L 17-19, 2011
and
S. Roth, J. Osterwalder, and T. Greber, *Corrigendum to: Synthesis of epitaxial graphene on rhodium from 3-pentanone[Surf. Sci. 605 (2011) L17][1]*, Surface Science **619**, 119, 2014

Abstract

The synthesis of high quality single layer graphene on rhodium, $g/\mathrm{Rh}(111)$, is reported. The graphene layers are grown at 1060 K by low pressure chemical vapor deposition (CVD) using 3-pentanone as a precursor molecule. The presented growth technique shows an easy high quality production method for epitaxial graphene monolayers. The chemical composition and structural properties of such self-assembled monolayers were characterised by x-ray photoelectron spectroscopy (XPS) and low energy electron diffraction (LEED). Scanning Tunneling Microscopy (STM) confirms the formation of a 3 nm super cell and a unique surface morphology which establishes the potential of $g/\mathrm{Rh}(111)$ as a template for molecules.

3.1 Introduction

The application of graphene in future electronic devices [30] or its use as a template for molecular self assembly [31] demands high quality production methods of this material of the day. Growing graphene by chemical vapor deposition on various substrates is a booming field of research, since it is a possible route towards mass production of such layers [32]. The growth of graphene on Rh(111) has been demonstrated [6, 33, 34, 35] as well as on other metal substrates such as Ni [36], Cu [6, 32], Ir [37], or Ru [38, 39, 40]. On substrates with carbon in the bulk such as Ru [38, 41] or SiC [42] graphene can be formed by segregation from the bulk. For the growth of graphene on rhodium, various precursors have been used. Müller et al. exposed a clean rhodium surface ex-situ to liquid acetaldehyde $H_3 - C(O)H$ or acetone $CH_3 - C(O) - CH_3$ and then annealed the sample in ultra high vacuum to 1000 K which leads to a single layer graphene [33]. An all in situ preparation was realized by ethene C_2H_4 at a pressure of $p = (2 - 3) \cdot 10^{-8}$ mbar at a sample temperature of 970 K for 1 hour [6]. Under higher pressure $p = 3 \cdot 10^{-7}$ mbar the graphene layer can be formed within three minutes [34]. Here we report the use of a higher ketone like 3-pentanone as a precursor molecule, which yields better layers than we obtained by the use of the ethene precursor [43].

3.2 Experimental Section

The experiments have been performed in a modified VG ESCAlab (Electron Spectroscopy for Chemical Analysis) [17] under ultrahigh vacuum conditions. For XPS studies a monochromatised Al K_α x-ray source was used, providing photons with an energy of 1486.6 eV. The scanning tunneling microscopy experiments were carried out in a Park Scientific microprobe VPII instrument, attached to the same ultrahigh vacuum system, using W tips. The Rh(111) single crystal was cleaned with repetitive cycles of Ar sputtering at a pressure of $p = 5 \cdot 10^{-5}$mbar with an ion current density between $0.6 - 0.4$ μA/cm^2 and annealing up to 1030 K. After each cycle an additional oxygen treatment was performed to burn residual carbon contaminations. The oxygen exposure was gradually reduced after each cleaning cycle from 29 to 6 Langmuir (1 Langmuir = $1 \cdot 10^{-6}$ Torr$\cdot$ s). The remaining oxygen was removed by flashing the crystal to a temperature of 1156 K. Before introducing 3-pentanone to the UHV system it was further purified by freezing/melting/pumping cycles. The graphene layer was formed by chemical vapor deposition of 3-pentanone at a pressure of $p = 2 \cdot 10^{-7}$mbar, at a sample temperature of 1060 K. After a 10 min. exposure, corresponding to about 90 Langmuir, the sample was gradually cooled down (30 K/ min) to room temperature.

3-pentanone is a carbohydrate ketone with the structural formula

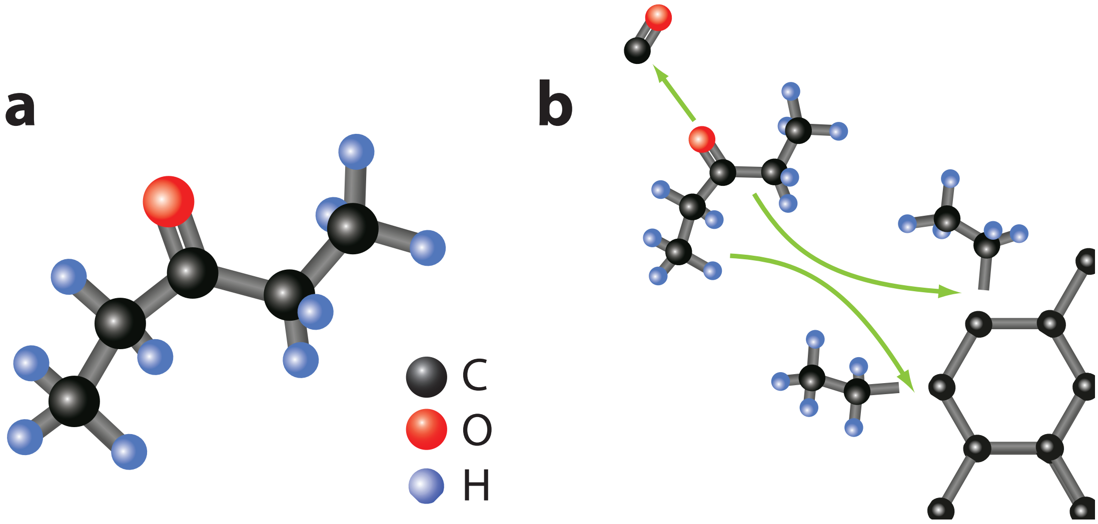

Figure 3.1: a) Sketch of the 3-pentanone molecule, which has been used as a precursor to grow graphene. b) Tentative illustration of the graphene formation process. The pentanone molecules break into radicals on the hot rhodium surface. $C-C$ units build graphene, while at 1000 K the remaining $C=O$ and hydrogens do not stick on the surface.

$CH_3-CH_2-CO-CH_2-CH_3$. An illustration of the molecule can be seen in Fig. 3.1. The molecule was chosen due to its favorable geometry, and bond strength hierarchy. The $C=O$ double bond is strongest and not expected to be broken during the reaction. Since the $C-H$ bonds (4.3 eV) and the CH_3-CH_2 bonds (3.8 eV) are stronger than the $C_2H_5-C(O)C_2H_5$ bond (3.5 eV) we expect that this is the predetermined breaking point which releases upon dissociation of 3-pentanone two C_2H_5 radicals that act as dimer building blocks for graphene, while the carbonyl and the hydrogen desorb in the form of CO and H_2 and are pumped away. On clean Rh(111) the CO and the H_2 desorption temperatures are 510-540 K [44] and 410-490 K [44], respectively. A tentative illustration of this process is sketched in Fig. 3.1 b). The details of the graphene formation process were not further studied within this work, though the resulting high quality single layer graphene sheets are an a posteriori justification of 3-pentanone to be an excellent precursor molecule for graphene growth.

3.3 Results and Discussion

In Fig. 3.2 Al K_α x-ray photoelectron spectra of a g/Rh(111) preparation are shown. The overview in Fig. 3.2 a) indicates that the surface consists of carbon and rhodium. In order to estimate the surface coverage, we compare the system to the h-BN nanomesh, a single h-BN layer on Rh(111) [45]. The growth of this layer is self terminated and therefore a

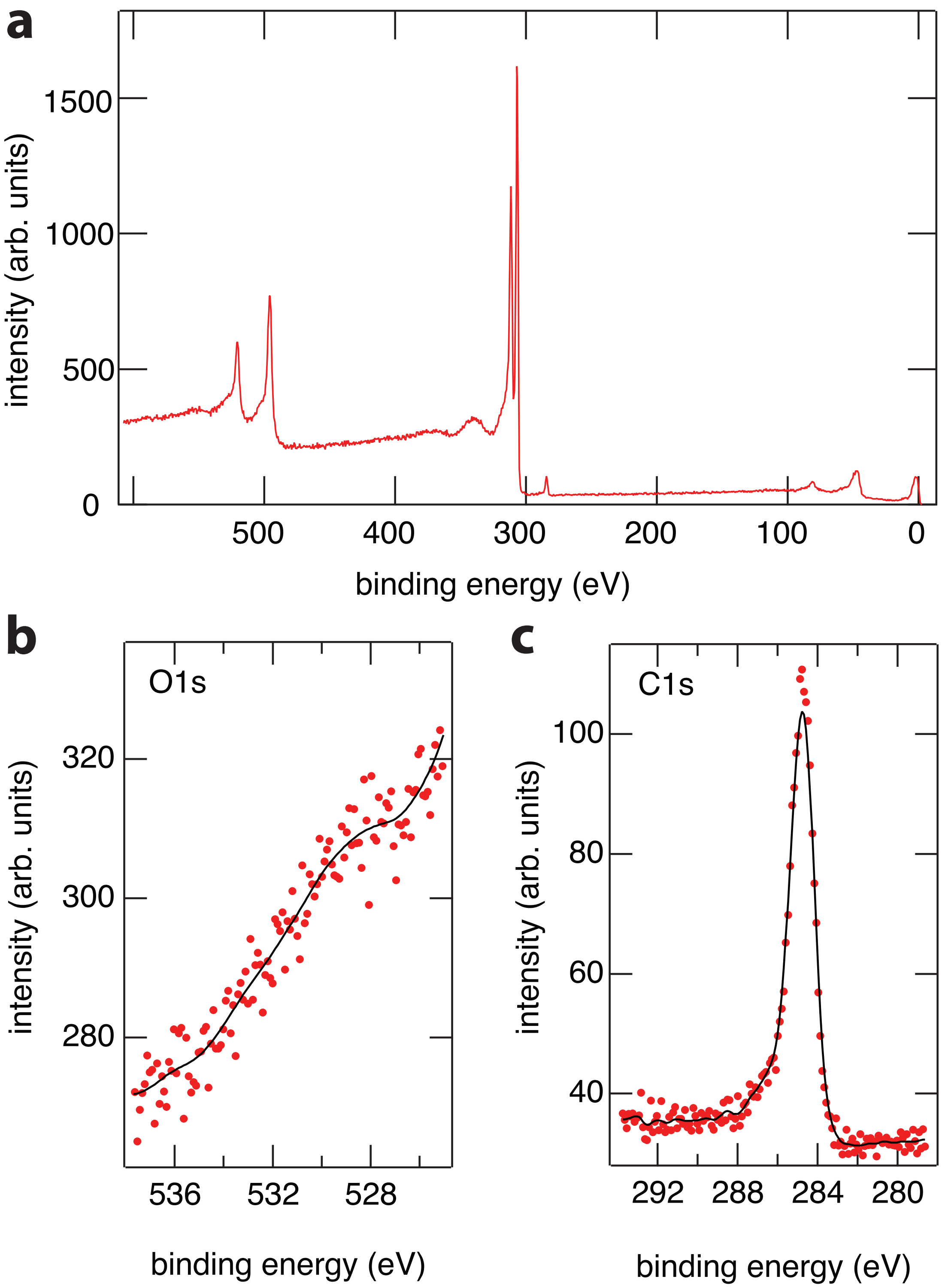

Figure 3.2: Al $K_\alpha(\hbar\omega = 1486.6$ eV) x-ray excited photoemission of a graphene layer on rhodium: (a) survey spectrum. (b) close up on the O 1s core level. The shoulder at a binding energy of 529 eV corresponds to an intrinsic excitation of rhodium. (c) close up on the C 1s core level spectrum. The black solid lines are a guide to the eye (10 point smooth).

good single layer reference.

The photoemission intensity of a clean Rh(111) surface can be estimated as

$$I_{Rh} = \Phi \cdot A \cdot n_{Rh} \cdot \sigma_{Rh} \cdot \frac{1}{d_{Rh}} \int_{0}^{-\infty} e^{-\frac{1}{\lambda_{Rh}} z} dz \tag{3.1}$$

where Φ is the photon flux, A the illuminated area, n_{Rh} is the atomic density of Rh, σ_{Rh} the photoionization cross section, λ_{Rh} the inelastic electron mean free path, and d_{Rh} the inter layer distance in Rh. This leads to

$$I_{Rh} = \Phi \cdot A \cdot n_{Rh} \cdot \sigma_{Rh} \cdot \frac{\lambda_{Rh}}{d_{Rh}}. \tag{3.2}$$

To compare photoemission intensities of elements, we define a normalized intensity A_{Rh} as

$$A_{Rh} = \frac{I_{Rh}}{n_{Rh} \cdot \sigma_{Rh}}. \tag{3.3}$$

Similar to Rh, we define a normalized intensity for a single layer h-BN $A_{BN} = (A_B + A_N)$, as well as for a overlayer graphene A_C:

$$A_{BN} = \frac{I_{BN}}{n_{BN} \cdot \sigma_{BN}} \tag{3.4}$$

$$A_C = \frac{I_C}{n_C \cdot \sigma_C} \tag{3.5}$$

If the atomic ratio (of a single layer h-BN on Rh(111) as determined by XPS) $(A_B+A_N)/A_{Rh}$ of 0.43 is normalized with the unit cell sizes of h-BN (a_{BN}= 2.50 Å) and graphene (a_g= 2.46 Å), respectively, we find (from the graphene atomic ratio $(2A_C)/A_{Rh}$ of 0.40) a carbon coverage that corresponds to 0.90±0.05 layers of graphene.

Since the reported scanning tunneling microscopy data indicate full graphene coverage (Fig. 3.4), we propose the difference between the above XPS and the STM result to be related to different photoelectron attenuations across h-BN and graphene, respectively. Assuming 1 monolayer of graphene, we get for electrons from the Rh 3d5/2 level at a kinetic energy of 1180 eV a 10 % higher attenuation, as compared to h-BN. This may be related to the 3.3 % higher atom density in graphene, and to the fact that graphene allows for more low energy electron-hole pair excitations.

In Fig. 3.2 b) and c) the O 1s and the C 1s core levels are shown. The C 1s spectrum displays a peak at a binding energy of 284.8 eV. This is in agreement with the high resolution XPS data on g/Rh(111) of Preobrajenski et al. [6]. Our instrumental resolution of 0.5 eV does not resolve the double peak in the C 1s spectrum that indicates high and low regions of

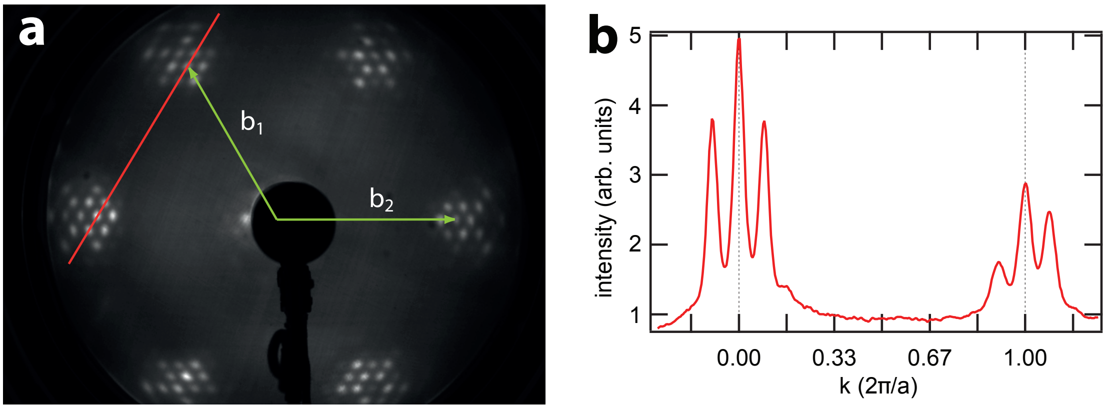

Figure 3.3: a) LEED image of a graphene layer on Rh(111) at a kinetic energy of 80.3 eV. The reciprocal 1 × 1 lattice vectors b_1 and b_2 are indicated. b) Intensity profile along the indicated line in (a). The Rh-Rh nearest neighbor distance is a= 0.269 nm.

g/Rh(111) [6]. No signature of CO is found, neither a O 1s signal nor a C 1s carbonyl-peak between 285.5 and 286 eV binding energy [46]. The small shoulder in the O 1s region is a loss satellite 9 eV below the Rh $3p_{1/2}$ line, which is also found in Auger spectra [47]. The XPS results are a first indication for the decomposition of 3-pentanone and the desorption of the carbonyls and hydrogen when it is brought in contact with the hot rhodium surface, and the formation of a single layer of graphene.

In a next step we investigated the long range order of the structure by low energy electron diffraction (LEED). In Fig. 3.3 a) the LEED pattern of a graphene layer on Rh(111) is shown, recorded at a kinetic energy of 80.3 eV. The rhodium principal spots are surrounded by the superstructure spots that can be expressed with fractions of the principal spot distances. The high epitaxial quality of the graphene layer is reflected in the additional higher order superstructure spots around the first order spots. The intensity profile along the indicated line is shown in Fig. 3.3 b). The lattice constant $N \cdot a_{sub}$ of the graphene superstructure is given by the ratio between the distance of the superlattice and the substrate spots. N is found to be 11.2 ± 0.5, which corresponds with $a_{sub} = 0.269$ nm to a super lattice constant of 2.93 ± 0.13 nm. This is in agreement with a commensurate 12 × 12 on 11 × 11 periodicity of the superstructure as reported in [33].

The exposure of rhodium to 3-pentanone leads to a large area growth of single layer graphene. Fig. 3.4 a) shows a constant current scanning tunneling microscopy (STM) image over a large area of the graphene layer that was synthesised on rhodium (111) [48]. The growth is nearly free of defects. The layer has a unique surface corrugation, which has previously been observed [33, 34, 35], and which is different from other transition metals such as Ru [38, 40, 49] or Ir [50]. Fig. 3.4 b) shows a close up of the graphene unit cell.

The unit cell is marked with a red rhombus. The superlattice constant is measured to be 3 nm, and is in agreement with an 11 × 11 unit cell. At the given tunneling voltage of 1 V, the corrugation, i.e. peak to peak amplitude is 0.12 nm. It is determined from a histogram of the vertical tip positions in Fig. 3.4 b). A special feature in the corrugation of the g/Rh(111) supercell are three pockets with a diameter of roughly 1 nm (green circles). This additional structure was identified to have a low local work function [34], and it will be interesting to further explore the influence of this feature on the template function [31], which is, based on these details, expected to be different to that of e.g. g/Ru(0001).

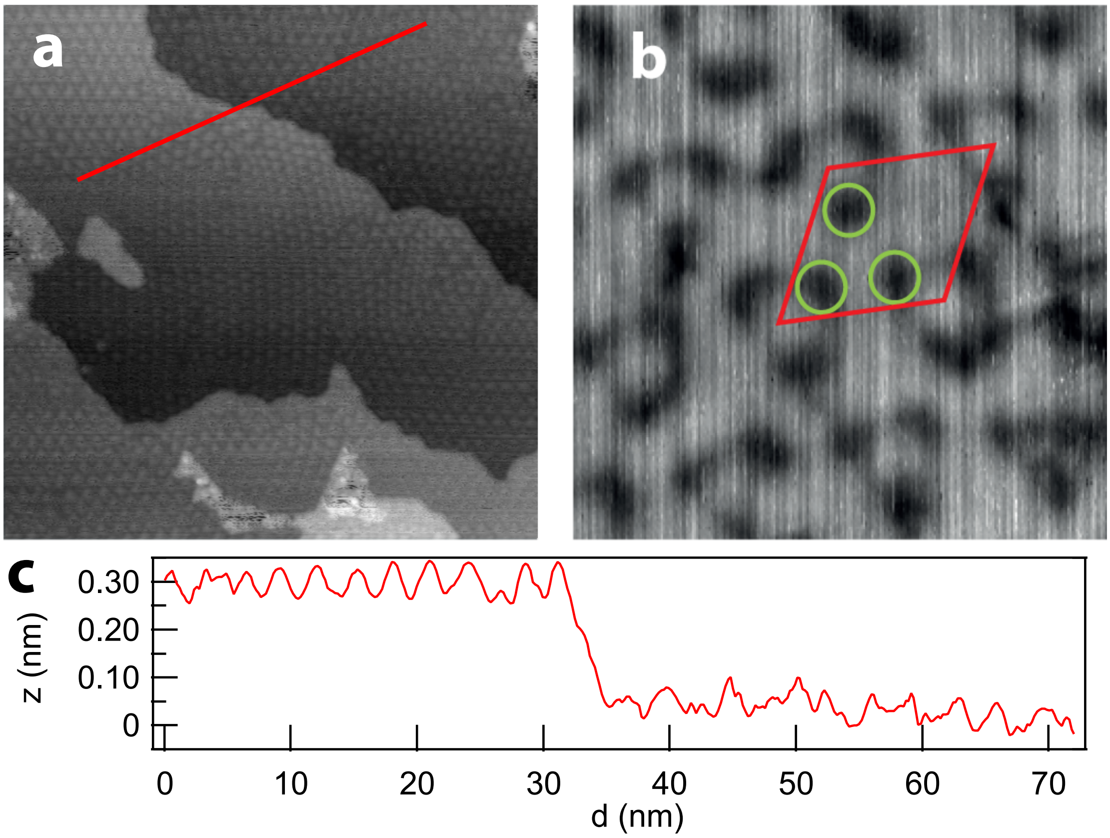

Figure 3.4: Constant current STM image of a graphene layer on Rh(111). I_{tunnel} = 1 nA, V_{tunnel} = 1 V, scanning direction: vertical. (a) large area 100 × 100 nm, (b) close up: 10 × 10 nm. Areas close to the Rh substrate are dark. The corrugation at these tunneling conditions is 0.12 nm. (c) shows a hight profile along the indicated line in (a).

A C 1s x-ray photoelectron diffraction pattern was recorded from g/Rh(111), Fig. 3.5a. The pattern is dominated by six circular fringes at grazing polar emission angles. They result from in-plane scattering in the graphene layer. Forward scatterering peaks in the region of θ=23 °, which would correspond to forward scattering from a second graphene layer are not found. The recorded XPD pattern is in good agreement with the single scattering calculation in Fig. 3.5b. The calculations are based on a unit cell based on coordinates obtained from DFT calculations [51], Fig. 3.5c.

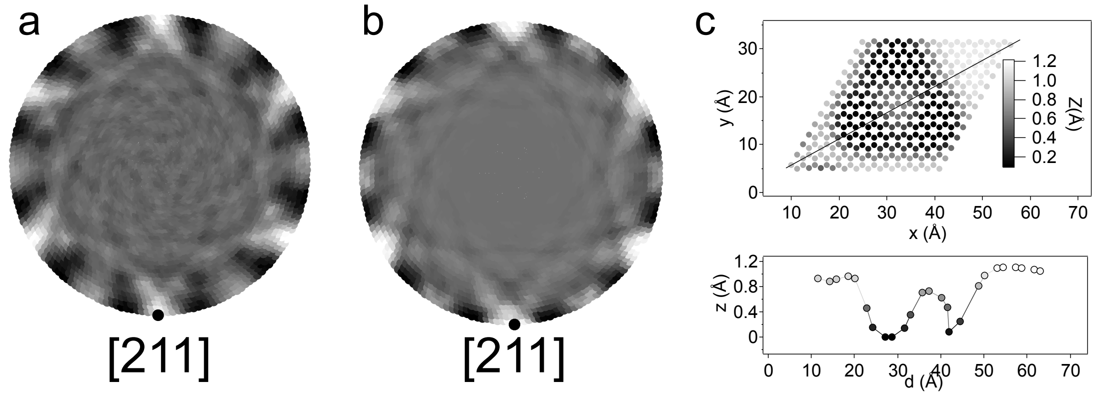

Figure 3.5: X-ray photoemission diffraction pattern shown in stereographic projection recorded under MgK$_\alpha$ radiation (hν=1253.6 eV) (a). (b) Corresponding single scattering simulation from the graphene unit cell in (c). (c) schematic atomic model obtained by DFT calculation of a graphene monolayer on a Rh (111) surface with a height profile along the indicated line

3.4 Graphene etching by Borazin exposure with simultaneous h-BN formation

Graphene layers as well as h-BN layers show great stability. They are stable in air, as well as resistant to high temperatures under UHV conditions [52]. Nevertheless, exposing a graphene layer grown on the Rh(111) surface to boranzine $(HBNH)_3$ under formation conditions for h-BN nanomesh on Rh(111) leads to an etching and replacment of the graphene layer by an h-BN layer. Figure 3.6b shows integrated XPS intensities of C 1s, B 1s, and N 1s core levels of a graphene layer subsequently exposed to borazine. After each borazine exposure at 1070 K, the C 1s signal decreases, while the B 1s, and N 1s signals increase. The intensity ratio between N1s and B 1s remains constant at $\frac{N1s}{B1s} = 3.8 \pm 0.3$ (see inset) which is in agreement with the 1:1 stochiometry. The constant ratio during the growth is consistent with a picture where h-BN grows in islands, and does not substitute C atoms by either B or N preferably. This assumption is further supported by the graphene / h-BN lateral hetero junctions seen in the STM picture in Fig. 3.8. Even though the periodicity of the g/Rh(111) and the h-BN/Rh(111) superstructures are similar, 2.9 nm and 3.2 nm, respectively, their superstructures shows different corrugations and are therefore clearly distinguishable.

The surface transition from graphene to h-BN is also reflected in the electronic bandstructure. Figure 3.6a shows a series of normal emission UPS spectra taken consecutively after each borazine exposure. The photoemission spectra show a splitting of the $\sigma-$ and the $\pi-$bands after the borazine exposures. With increasing nanomesh coverage, the well known band splitting becomes visible.

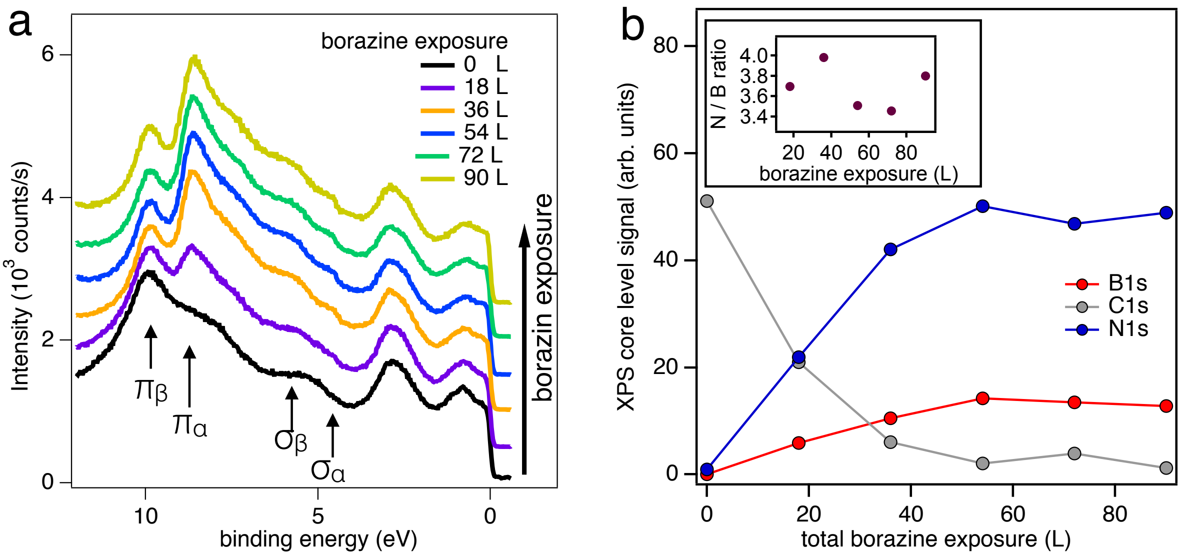

Figure 3.6: **Sequential borazine exposure** He IIα photoemission spectra (a) and integrated XPS intensities for B 1s, C 1s and N 1s core levels (b) for sequential borazine exposure of a single layer graphene on Rh(111).

The split $\sigma-$ and $\pi-$bands do not shift in binding energy during the formation process and arise at binding energies similar the ones from complete h-BN layers (Fig. 3.7). This again supports the model of an isolated island growth mechanism of h-BN rather than a local substitution of single atoms.

3.5 Conclusions

In summary it has been shown that epitaxial graphene monolayers can be grown by means of chemical vapor deposition of 3-pentanone on Rh(111). A highly regular, corrugated

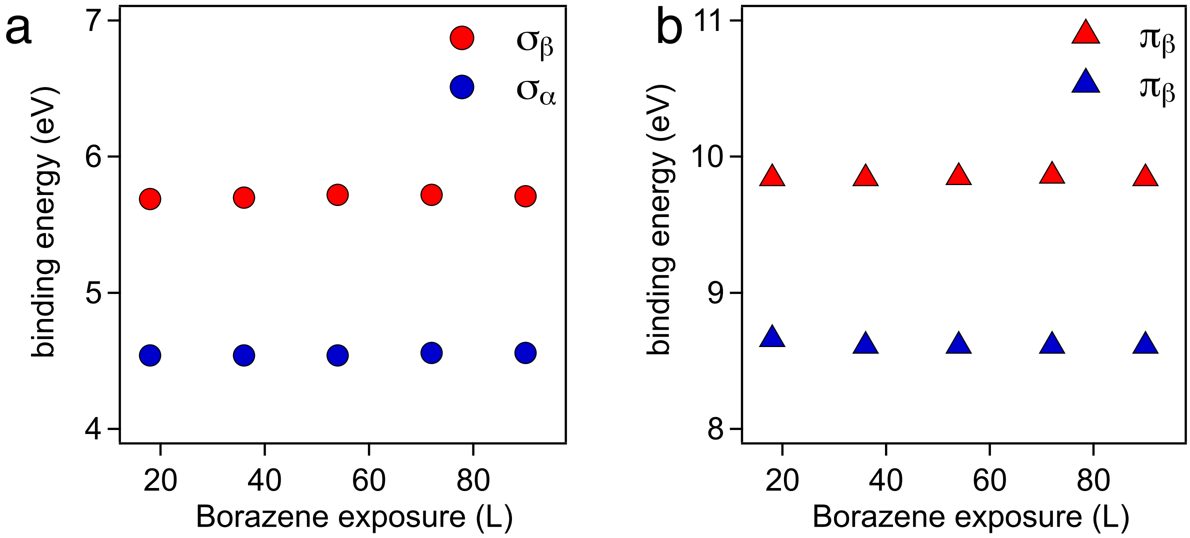

Figure 3.7: **Electronic band positions** Binding energies of the $\sigma-$bands (a) and the $\pi-$bands (b) after each borazine exposure. The band positions remain constant with increasing $h-$BN coverage.

superlattice was observed with a lattice constant of 2.93 ± 0.13 nm. XPS data indicate a single graphene layer on the rhodium surface. The corrugation of the graphene layer has three pocket-like areas, which could act as a molecule traps, when using graphene on rhodium as a template for molecular self-assembly [31]. Given the favorable performance of 3-pentanone as a precursor molecule, we expect that it will also apply for other substrates. Upon exposure of g/Rh(111) to borazine, an etching of graphene along with a simultaneous growth of h-BN is observed. This mechanism opens the door for controlled structuring of in-plane arrangements of insulating and conducting sp^2 structures [53].

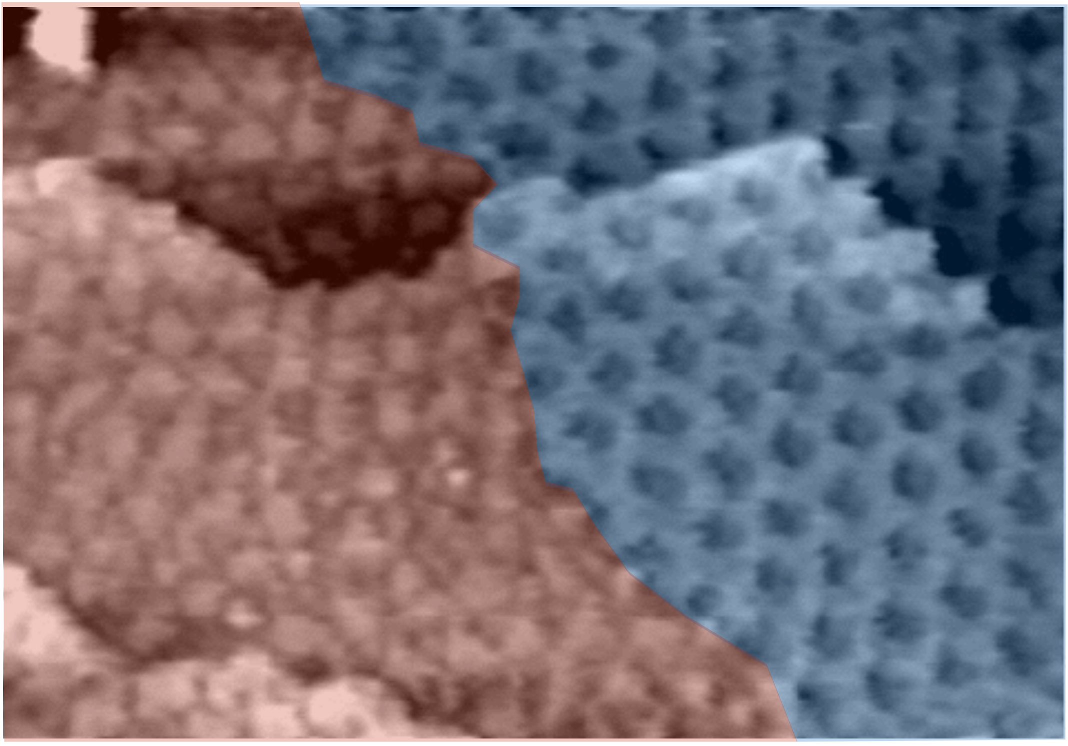

Figure 3.8: **In-plane heterojunction** Constant current STM image of an in-plane graphene/h-BN hetero junction on Rh(111). The graphene area is colored red, and the h-BN area is colored blue. $I_{tunnel} = 1$ nA, $V_{tunnel} = 1$ V, scanning direction vertical, scanning field 50 × 30 nm.

Chapter 4

Graphene / hexagonal boron nitride heterostack on Cu(111)

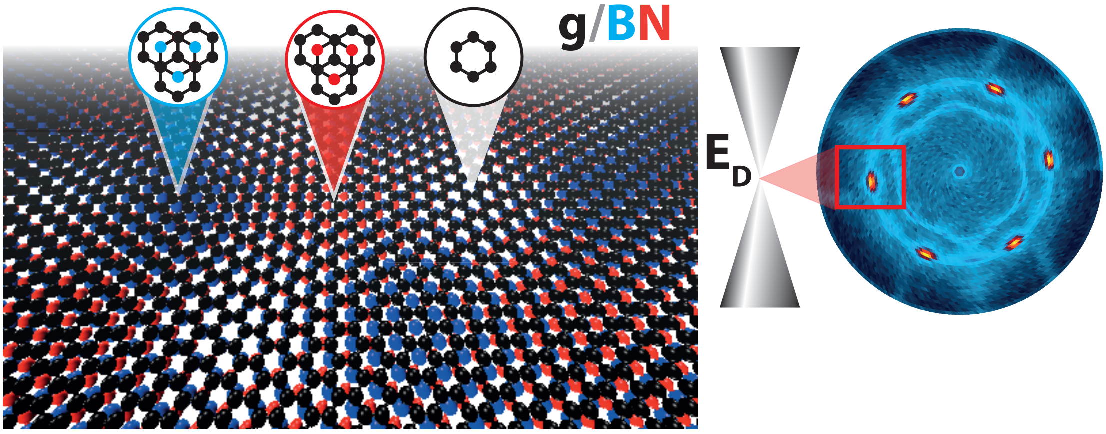

The following Chapter contains a modified version of the manuscript published in Nano Letters:

S. Roth, F. Matsui, T. Greber, and J. Osterwalder, *Chemical vapor deposition and characterization of aligned and incommensurate graphene / hexagonal boron nitride heterostack on Cu(111)*, Nano Letters **13**, 2668-2675, 2013

Abstract

Two limiting factors for a new technology of graphene-based electronic devices are the difficulty of growing large areas of defect-free material, and the integration of graphene with an atomically flat and insulating substrate material. Chemical vapor deposition (CVD) on metal surfaces, in particular on copper, may offer a solution to the first problem, while hexagonal boron nitride (h-BN) has been identified as an ideal substrate material. The bottom-up growth of graphene/h-BN stacks on copper surfaces appears therefore as a promising route for future device fabrication. As an important step, we demonstrate the consecutive growth of well aligned graphene on h-BN, both as single layers, by low-pressure CVD on Cu(111) in an ultra-high vacuum environment. The resulting films show a largely predominant orientation, defined by the substrate, where the graphene lattice aligns parallel to the h-BN lattice, while each layer maintains its own lattice constant. The lattice mismatch of 1.6 % between h-BN and graphene leads to a moiré pattern with a periodicity of about 15.4 nm, as observed with scanning tunneling microscopy. Accordingly, angle-resolved photoemission data reveal two slightly different Brillouin zones for electronic states localized in graphene and in h-BN, reflecting the vertical decoupling of the two layers. The graphene appears n-doped, and shows no gap opening at the $\overline{K}$ point of the two-dimensional Brillouin zone.

Graphene is a single-layer sp^2 hybridized honeycomb carbon network, which shows outstanding stability, crystalline perfection and electronic properties. Using single graphene sheets exfoliated from graphite samples, a great potential for applications in future electronics has been demonstrated in recent years [30]. However, samples produced in this way are tiny and have to be transferred onto a suitable insulating substrate for device fabrication. Therefore the method can hardly be upscaled. Moreover, key properties, like the electron mobility [3] or the long ballistic mean free path [54], are limited by the structural and electronic roughness of the substrate [55, 56].

Two different routes have so far been followed in order to upscale the production of single-layer graphene. Controlled graphitisation of Si-terminated SiC(0001) in an argon atmosphere of 1 bar was shown to produce graphene layers on the wafer scale, with relatively large domain sizes and good mobilities [5]. The second route involves large-area synthesis of single-layer graphene films on copper foils [32, 57] by chemical vapor deposition (CVD), which is self-terminating at the single-layer stage due to the catalytic involvement of the metal surface. The method has been extended soon after to the direct roll-to-roll production of 30-inch graphene films for transparent electrodes [58]. In order to exploit the unique properties of the graphene layers, the copper foil or thin film has to be etched away by chemical means, and the graphene layer needs to be transferred onto an insulating substrate. The polycrystalline nature of the copper substrates limits the structurally coherent domain size within the graphene monolayer.

Hexagonal boron nitride (h-BN) has been a natural candidate substrate for graphene-based electronic devices, due to its insulating nature and close structural relationship [59, 60]. Its individual layers exhibit the same honeycomb network, here heteroatomic, with a lattice mismatch of 1.6% [61, 62], and the material has a large energy gap of about 6 eV [63]. Indeed, by building devices using exfoliation techniques, it could be shown that graphene on h-BN exhibits the best electronic properties demonstrated so far [64]. Consequently, various groups have explored the consecutive epitaxial growth of graphene on h-BN. Already in the year 1996, the Oshima group reported the hetero-epitaxial growth of monolayer graphene on monolayer h-BN on Ni(111) [22, 23, 65]. Their two-step low-pressure CVD growth method involved high-temperature exposure of the atomically clean nickel surface to benzene-like borazine $(HBNH)_3$ to form the h-BN layer, and subsequent much higher exposure to benzene in order to grow the graphene layer. The characterization of these films by low-energy electron diffraction (LEED) showed that most parts of the surface are covered with graphene flakes with their lattices oriented in the same way as the underlying h-BN layer, while other, rotated domains are present as a minority species. Scanning tunneling microscopy (STM) images showed atomic corrugations that were vaguely interpreted in terms of two incommensurate layers [65], but were not more conclusive. More recently, a similar system was studied by angle-resolved photoemission spectroscopy (ARPES) [66]. Here, the low-pressure CVD growth of the graphene layer was preceded by an extra step in which Au atoms were intercalated between the h-BN monolayer and the Ni(111) surface. This resulted in an effective decoupling of the double layer from the substrate, confirmed by the appearance of a gap-less and linearly dispersing graphene π band within the h-BN band gap, passing through the Fermi level near the $\overline{K}$ point of the two-dimensional Brillouin zone. Further studies included the single-layer g/h-BN growth on Ru(0001) [67], as well as large-area growth of few-layer g/h-BN stacks on graphite or copper foils [68]. In both cases the typical Raman signature of graphene was demonstrated.

In all previous studies of g/h-BN hetero-growth, there was no conclusive structural characterization of the double layer, nor how the structural relationship is reflected in the electronic bands. The structural issue has been addressed in a recent study by the group of LeRoy by using exfoliated samples of graphene and h-BN in order to form the double layer [69]. STM images showed very flat surfaces and the appearance of different moiré patterns, depending on the relative orientation of the individual graphene and h-BN flakes. This Chapter demonstrates the growth of well-aligned g/h-BN double layers by two-step low-pressure CVD on Cu(111) and uses x-ray photoelectron diffraction (XPD), LEED and STM for structural analysis as well as ARPES for a precise characterization of the electronic structure.

The exposure of the hot Cu(111) surface ($T = 1050$ K) to borazine ($p = 5 \cdot 10^{-6}$ mbar) results in the formation of a single h-BN layer [70, 71]. The orientation of this layer is guided by the Cu surface during the growth procedure. As a consequence, the h-BN lattice is oriented almost parallel to the surface lattice of the substrate. The LEED pattern in Fig. 4.1a shows the hexagonal arrangement of six principal diffraction spots, with the three-fold symmetry of the Cu(111) surface still reflected in the spot intensities (see also intensity distribution in Fig. 4.1d). A closer look at the LEED spots (Fig. 4.1c) reveals a slight difference for the in-plane reciprocal lattice vectors $g_{(BN)}$ and $g_{(Cu)}$. The difference of $1.9 \pm 0.1\%$ agrees well with a lattice mismatch of 1.8% found for this system in a recent low-temperature STM study based on the analysis of moiré patterns [71]. Fig. 4.1c further indicates that the h-BN lattice is not aligned precisely with the Cu(111) lattice, but that there is a small angular spread (FWHM$= 2.5°$). Again, this confirms the results by Joshi et al. [71] where all observed moiré patterns could be reproduced with a relative angular spread of 3°.

The h-BN layer is stable up to high temperatures [52], which allows the consecutive CVD growth of a graphene layer on top. Upon exposure of the h-BN/Cu(111) surface to 3-pentanone at a temperature of 1100K and a pressure of $p = 2.2$mbar, the principle diffraction spots in the LEED pattern persist, indicating the formation of a graphene layer that

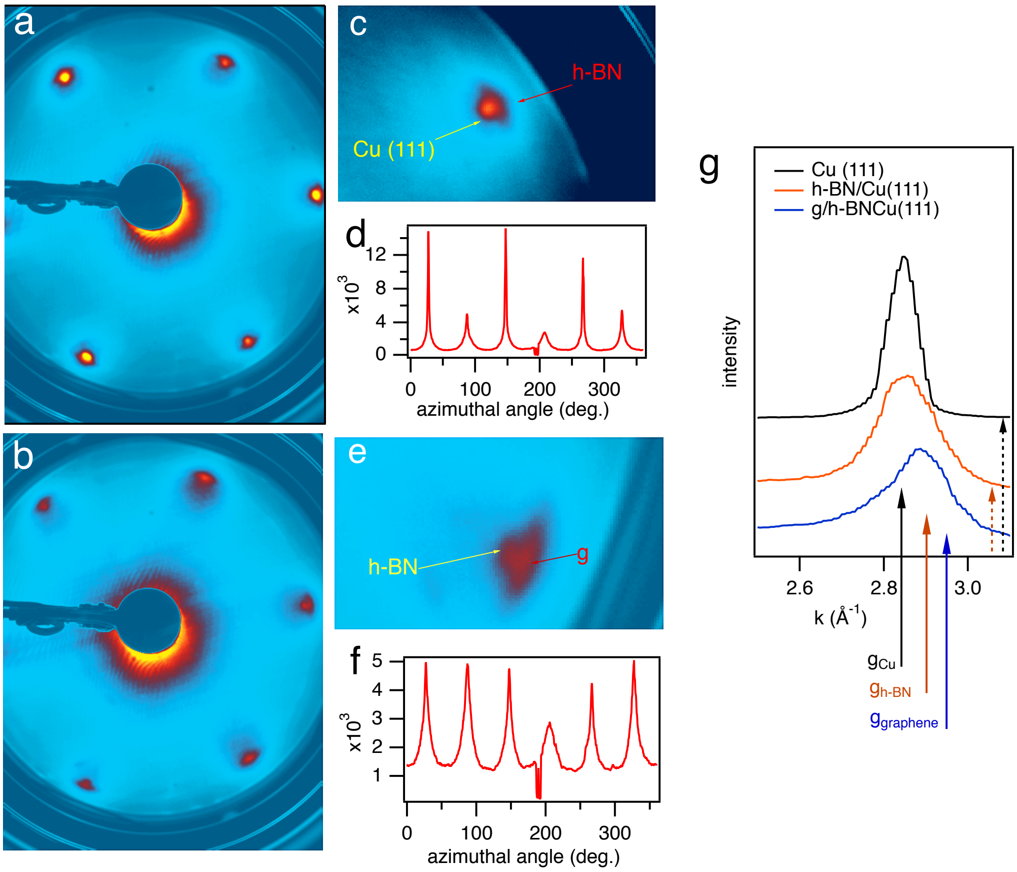

Figure 4.1: **Layer orientation** LEED patterns at an electron energy of 70 eV taken from a single layer of h-BN on Cu(111) (a), and from a single-layer g/h-BN/Cu(111) stack (b). Panel (c) zooms in to a principle spot of (a), while (e) zooms in to a spot in (b), showing the contributions from substrate and h-BN layer, and from the g/h-BN stack, respectively. (d) and (f) give intensity distributions along circular paths in (a) and (b), respectively, containing all six principle spots. (g) radial cuts through the LEED spots for each preparation stage (offsets indicated).

is predominantly aligned with the underlying h-BN layer (Fig. 4.1b). The spot intensities show here a six-fold symmetry, i.e. the substrate no longer influences the diffraction (see also intensity distribution shown in Fig. 4.1f). The spots have become significantly broader (FWHM = 10°), with a concomitant increase of diffuse scattering. A weak ring of intensity is observed along a circle containing all principle spots, indicating the presence of a small area fraction of randomly rotated domains. This is in accordance with the results of Kawasaki et al. [65], but the contribution of a distinct phase rotated by 30°, which was observed in their work, is very small in our data. The relative intensity of the ring with respect to the principal spots depends strongly on the preparation parameters. Lower substrate temperatures during the growth process consistently led to highly disoriented growth of the h-BN and the graphene layers (data not shown).

The single-layer character and the stacking order of the h-BN and graphene layers are established by XPS. Spectra of the 1s core levels of boron, nitrogen and carbon are shown in Fig. 4.2 a. For the preformed h-BN layer the coverage is determined by comparing the B 1s and the N 1s intensities to that of the Cu 2p core level of the substrate. The coverage values obtained from B 1s (1.16 ML) and from N 1s (1.05 ML), using theoretical cross section values [72] and an electron inelastic mean free path of 16.9 Å [73] for the substrate photoelectrons, are consistent with a nearly stoichiometric and self-terminated growth of a single h-BN layer. For the subsequent growth of the graphene layer, the catalytic activity of the bare metal surface is absent [32, 74]. The CVD process therefore requires much higher precursor pressures, and reaching single-layer coverage needs to be controlled via pressure, substrate temperature and exposure time. For the films discussed in this work the preparation temperature was chosen 40 K higher than for graphene growth using 3-pentanone on Rh(111) (T = 1060 K) [75]. In order to clarify the stacking order of the two layers, core level intensities were measured as a function of polar emission angle. The

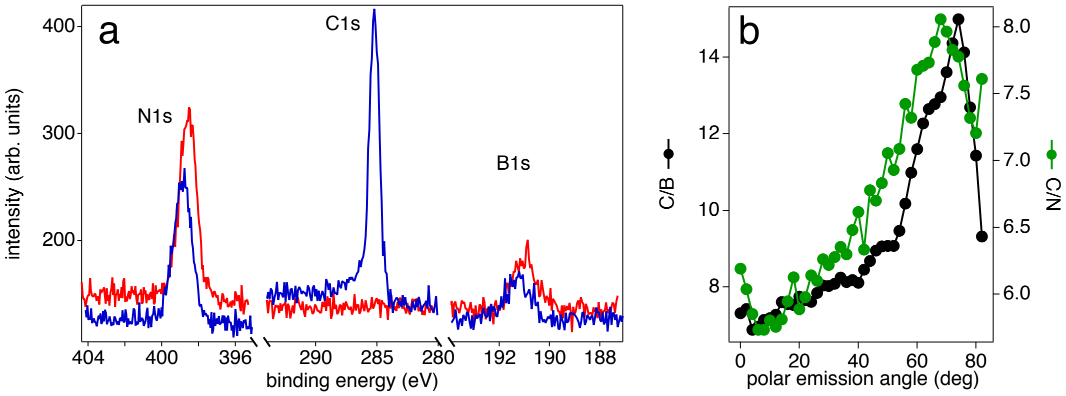

Figure 4.2: **Single layer characterization and stacking order** (a) Al Kα excited XPS normal emission spectra of nitrogen, carbon and boron 1s core levels from the single-layer h-BN/Cu(111) system (red) and the single-layer g/h-BN/Cu(111) stack (blue). Intensities of different core levels are to scale, with arbitrary offsets. (b) Ratios of C 1s to B 1s intensities (black) and C 1s to N 1s intensities (green) as a function of polar emission angle.

photoemission intensity ratios of C 1s / B 1s and C 1s / N 1s are shown in Fig. 4.2b. Both ratios show a significant increase towards higher polar angles. Photoelectrons emitted from the h-BN layer are more and more attenuated due to their longer pathlengths through the graphene layer at more grazing emission angles. This behaviour clearly supports the g/h-BN/Cu(111) stacking order. The graphene layer thickness determined via the attenuation of the B 1s and N 1s core level intensities is 1.0 ±0.1 ML. Attenuation factors were 0.85 for B 1s and 0.81 for N 1s for emission along the surface normal, which is in fair agreement with the attenuation for bulk graphite reduced to a thickness d of a single layer: using the relation $I(d) = I_0 \cdot e^{-\frac{d}{\lambda}}$, with d=3.3 Å and the inelastic mean free paths λ_i of 22 Å for B 1s and 19 Å for N 1s [76] for electrons in graphite at the corresponding kinetic energies (1295.6 eV for B 1s and 1088 eV for N 1s), an attenuation for B 1s of 0.86 and for N 1s of 0.82 is found. After the graphene CVD growth the h-BN coverage as calculated with the procedure described above showed no significant change.

We have extended these core-level studies to measurements of full hemispherical intensity distributions in order to record the corresponding x-ray photoelectron diffraction (XPD) patterns. Such data can reveal the local structural environment of typical photoemitters within a surface or a thin film sample [77, 78]. The B 1s and N 1s XPD patterns shown in Fig. 4.3a and b were recorded from the complete g/h-BN/Cu(111) stack. Both data sets show pronounced diffraction features mainly for the shallow emission angles along the rim of the plots. These features are associated with strong forward scattering enhancement along in-plane near-neighbour directions, as well as interference fringes from first-order diffraction [78]. Both diffraction patterns are in fact very similar to those from a h-BN monolayer alone [79]. This is very surprising in view of the stacking order established above: carbon atoms within the graphene layer on top of the h-BN layer should be expected to produce strong additional forward scattering peaks for lower polar angles, i.e. closer to the center of the plots. However, only weaker features are observed in these regions, which can be assigned to complex interference structures from in-plain scattering of the photoemitted electrons. They can be reproduced by multiple scattering cluster (MSC) calculations from a single free-standing layer of h-BN, as is shown in Fig. 4.3d and e [80, 81].

The absence of extra forward-scattering features in the B 1s and N 1s data could mean that the carbon layer is disordered. However, the C 1s XPD pattern displayed in Fig. 4.3c shows a well-developed diffraction pattern, rather similar in fact to that of the N 1s signal. A multiple-scattering cluster calculation for a free-standing graphene film, shown in Fig. 4.3f, describes this pattern quite well. From these data we conclude that the graphene layer is well ordered, with its lattice well aligned with the underlying h-BN layer. The absence of distinct forward scattering peaks in the XPD patterns from the underlying h-BN layer can only be rationalized by the incommensurate growth of the graphene layer, whereby the

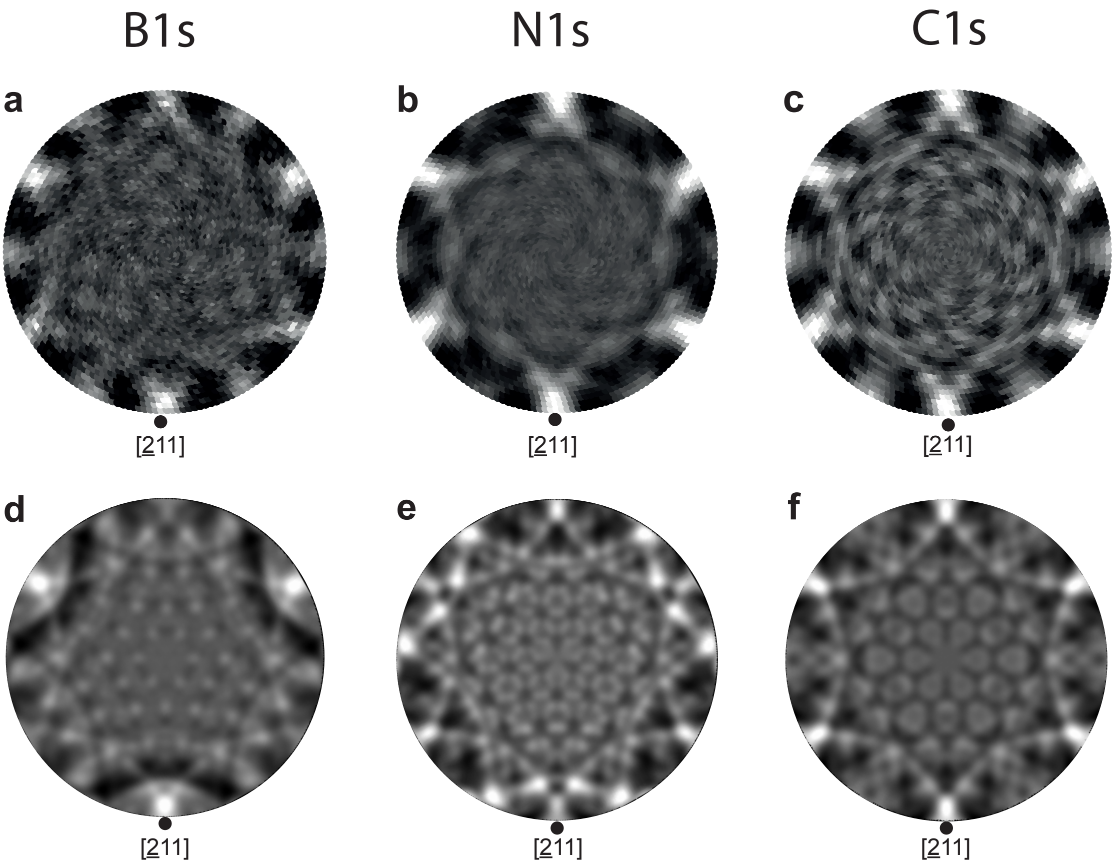

Figure 4.3: **X-ray Photoelectron diffraction** Stereographic representation of experimental (top row) and theoretical (bottom row) photoelectron diffraction patterns of B 1s, N 1s and C 1s core levels, displayed in a linear gray scale for polar emission angles between 0° and 82°. The experimental data are taken from a g/h-BN/Cu(111) stack, while the MSC calculations were performed with a free standing h-BN layer and a free standing graphene layer, respectively, containing 120 atoms each.

local registry of the C atoms with respect to the B and N atoms is lost.

The different lengths of the B-N bond in h-BN and the C-C bond in graphene cause a lattice mismatch of 1.6% between graphene ($a_g = 2.46$ Å) and h-BN ($a_{BN} = 2.50$ Å). When the two lattices are superimposed, moiré patterns arise with a periodicity depending on the relative orientation of the two layers [69]. STM images of the g/h-BN/Cu(111) stack are shown in Fig. 4.4a. Flat terraces with typical dimensions of 50 - 100 nm are observed. On most terraces a shallow modulation of the surface topography is found, corresponding to a regular moiré pattern with an average periodicity of 8.96 nm (see also zoom-in in Fig.

4.4b and profile in c). The superposition of the well aligned graphene and h-BN lattices results in a moiré periodicity of 15.4 nm, which corresponds to the length of 62.5 graphene unit cells. This value can be reconciled with the observed 8.96 nm periodicity by realizing that regions in this moiré pattern, where carbon atoms are situated on top of either N or B atoms or both, form a periodicity of 8.9 nm (see Fig. 4.4d). From these data, together with the XPS/XPD results, we conclude that most of the Cu(111) surface is covered by a double layer of well aligned h-BN and graphene lattices, with domain sizes of the order of 100 nm, limited by the terrace sizes of the Cu(111) substrate. 4.4a reveals also a peculiar type of defect on this heterolayer, taking the form of straight bands of uniform width (ca. 9 nm) and and lengths of up to 150 nm, with a height of ca. 8 Å. They could be folded graphene structures, so-called grafolds, that have recently been discussed and also experimentally observed in transferred graphene sheets [82].

In the following it is discussed how the structural arrangement of the g/h-BN/Cu(111) stack is reflected in the electronic bands associated with the individual sp^2-bonded layers. The band dispersion of the h-BN layer on Cu(111) along the $\overline{\Gamma K}$ direction is shown in Fig. 4.5a. The ARPES data were measured with He IIα excitation (photon energy $h\nu = 40.8$ eV), where the photoelectric cross section of the π band is much larger than that of the σ band which dominates ARPES data taken at the He Iα photon energy [83]. The h-BN π band is the prominent feature that disperses from a binding energy of 9.01 eV at the $\overline{\Gamma}$ point up to about 2.96 eV at the $\overline{K}$ point, mingling with the manifold of Cu 3d states [84] that shine through the boron nitride layer between 2.0 eV and ca. 4.5 eV. The sharp and fast dispersing band appearing between the Fermi energy and 2 eV binding energy is the *sp* band of the Cu substrate. The boron nitride σ bands are vaguely visible, dispersing downwards from 4 eV at the $\overline{\Gamma}$ point, where they are degenerate, to a maximum binding energy of about 12 eV at the $\overline{K}$ point. The high intensity of the π band and the sharpness of both, the π and the σ bands, testify the high quality of the h-BN layer. Upon formation of the graphene layer, an additional band appears in the ARPES data (Fig. 4.5b), while the Cu related bands are strongly attenuated by the extra layer of carbon atoms. The new band shows linear dispersion and crosses the Fermi energy near the $\overline{K}$ point of the surface Brillouin zone, as is expected for the π band of single-layer graphene. Also near the $\overline{K}$ point, at binding energies of around 3 eV, the top of the π band of the underlying h-BN layer is still visible and well separated from the graphene band, confirming that the h-BN layer remains intact and that its band gap persists. For lower momenta the π bands of the two materials appear merged into one broad band, consistent with the observations by Usachov et al. [66] on the gold-intercalated g/h-BN/Au/Ni(111) stack. At the $\overline{\Gamma}$ point the π band bottom appears at a binding energy of 8.71 eV. This value is about 0.5 eV lower that the one found for g/h-BN/Au/Ni(111) [66].

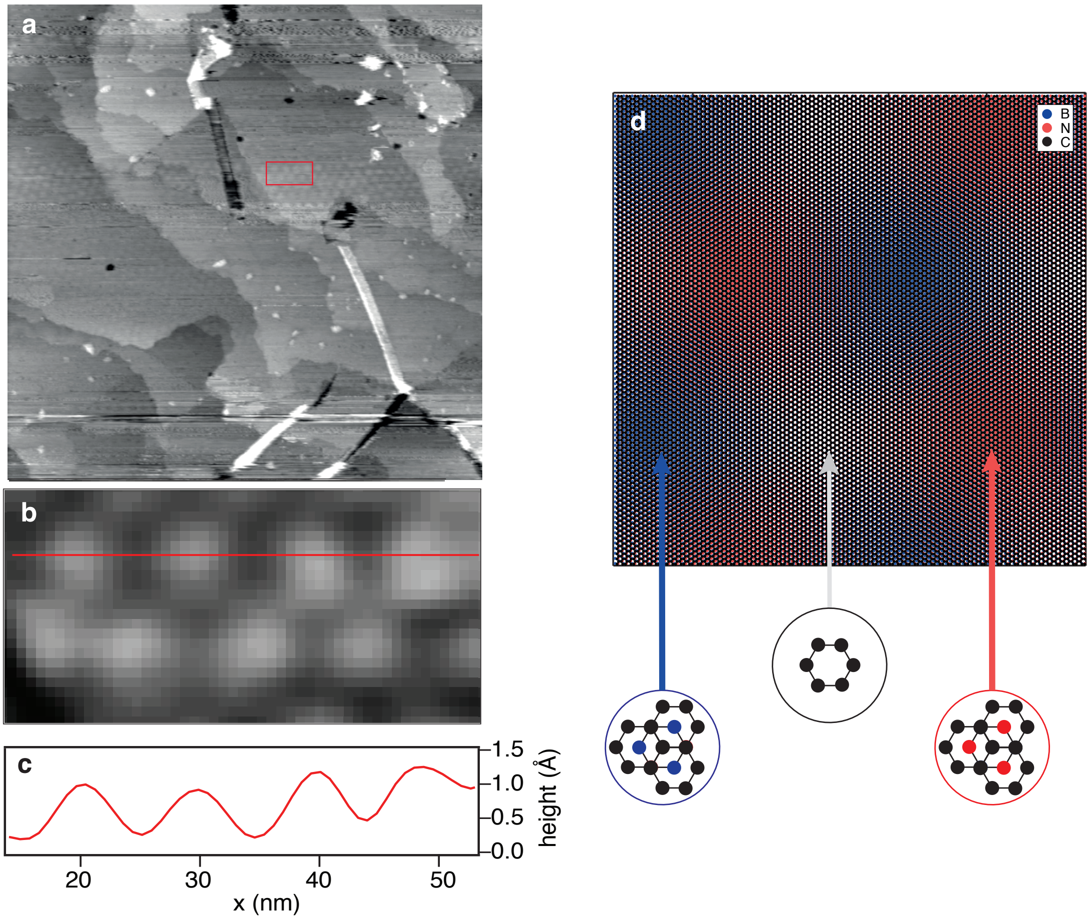

Figure 4.4: **Large scale moiré pattern formation** (a) STM topographic image of graphene grown on h-BN/Cu(111) (400 × 400 nm). The imaging parameters are $V_t = -1.0$ V and $I_t = 0.1$ nA. (b) shows a zoom into the moiré pattern observed in (a), with the according height profile along the red line given in (c). (d) Visualization of a moiré pattern resulting from the superposition of a graphene layer (black) with a lattice constant of 2.46 Å and a h-BN layer (B red, N blue) with a lattice constant of 2.50 Å, with the two lattice orientations fully aligned. The regions appearing blue result from C atoms covering B atoms, while in the red regions C atoms are on top of N atoms (see circular insets). In the black and white regions, the carbon atoms are on top of B and N atoms.

In the work by Usachov et al. [66] it was argued that the role of the intercalated Au was to decouple the h-BN film from the Ni(111) surface, allowing the h-BN layer to adjust its lattice constant in order to match the one of the graphene layer as much as possible. However, our structural analysis of the g/h-BN/Cu(111) stack suggests that the two lattice

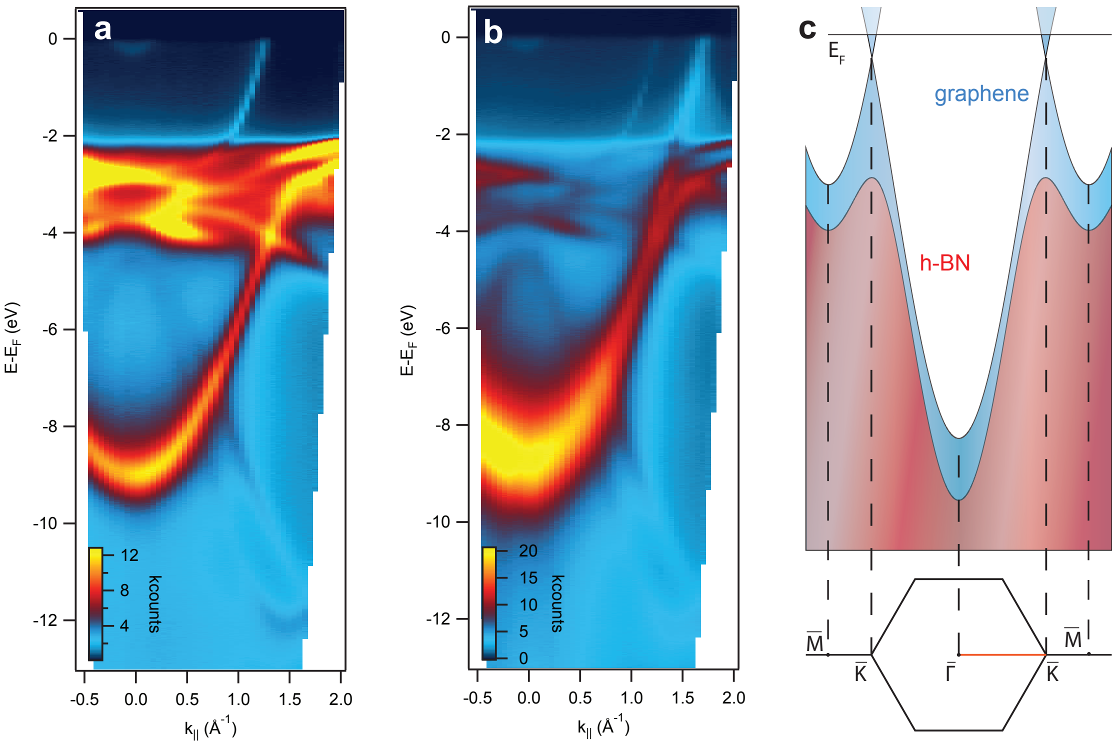

Figure 4.5: **Banddispersion of h-BN/Cu(111) and g/h-BN/Cu(111)** ARPES data of h-BN/Cu(111) (a) and of graphene on top of h-BN/Cu(111) (b), both measured along the $\overline{\Gamma K}$ direction of the two-dimensional Brillouin zone and excited with He IIα radiation. The schematic drawing in (c) illustrates the dispersion relations of the π bands associated with the h-BN and the graphene layers.

constants do not need to match in order to align the two lattices. Moreover, our ARPES data, like theirs, do not show any indication for gap formation that would be expected for a lattice matched g/h-BN stack [85].

We have therefore taken more detailed ARPES data in the vicinity of the $\overline{K}$ point (Fig. 4.6). These measurements still show no energy gap in the graphene π band, but a distinct kink in the dispersion and an intensity minimum around the crossing of the $\overline{K}$ point. Only one branch of the Dirac cone is observed. These are well known characteristics of a well ordered and gap-less graphene layer as observed in ARPES [27]. The first two are related to many-body effects in graphene upon photoemission, the last one is a photoemission matrix element effect. These same data can be used in order to analyse the effect of the incommensurate but well aligned growth of the graphene layer on top of the boron nitride

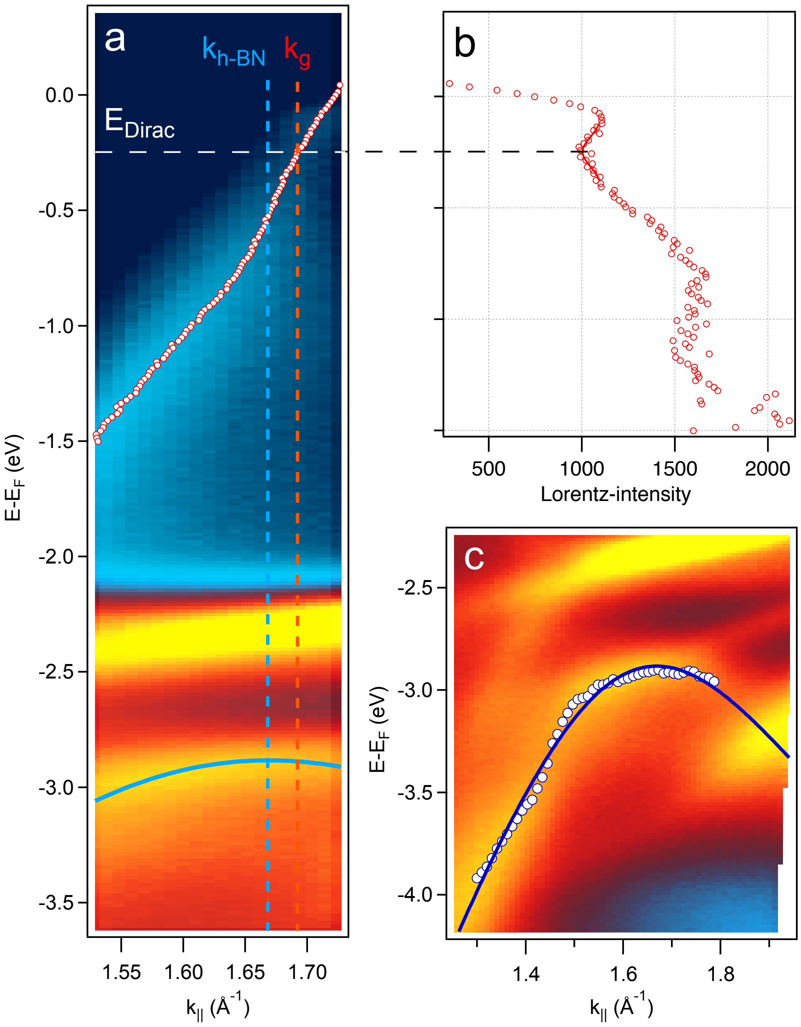

Figure 4.6: **Lattice mismatch and energy bands** (a) He IIα excited ARPES data along $\overline{\Gamma K}$ near the boundary of the Brillouin zone. Peak positions (dots in (a)) and intensities (b) of the graphene π band were determined by fitting Lorentzian curves for each momentum distribution curve. The Dirac point was determined by the minimum of photoemission intensity along the π band. The $\overline{K}$ point of h-BN is found at the maximum of the π band. (c) The dispersion of the h-BN π band (circles), obtained from Lorentzian fits to individual energy distribution curves, was fitted to the dispersion of a tight binding model (solid line) to precisely determine the band maximum.

layer. The two different lattice constants are reflected in different periodicities also in reciprocal space, and for entirely decoupled two-dimensional electron systems this should lead to slightly different sizes of Brillouin zones. We have extracted the positions of the $\overline{K}$ points of the two layers in the following way: For the fast dispersing π band of graphene Lorentzian functions were fitted for individual momentum distribution curves within a range of binding energies. The positions and intensities of each fit are shown in Fig. 4.6a and b, respectively. By comparison with the data of Bostwick et al. [27], the Dirac point, and therefore the $\overline{K}$ point, is found where the intensity shows a local minimum, which is at a binding energy of E_D= 0.248 ± 0.01 eV. Via energy dispersion curve this corresponds to a parallel momentum for the $\overline{K}$ point of $k_{\overline{K},g} = 1.693 \pm 0.005$ Å^{-1}. From this value a graphene lattice constant of $a_g = \frac{4\pi}{3k_{\overline{K},g}} = 2.47 \pm 0.01$ Å^{-1} is deduced. The level of doping is comparable to the intrinsic doping of a double layer of graphene formed on SiC(0001), where $E_D = 0.29$ eV was found [26].

The $\overline{K}$ point of the h-BN layer is located where the π band dispersion, measured in the same ARPES data set, reaches its maximum. It was determined by fitting Lorentzian curves to individual electron distribution curves (4.6c), avoiding nearby Cu 3d bands. A tight binding model, where only nearest neighbour hopping was taken into account, was fitted to these data points. A dispersion relation along the $\overline{\Gamma K}$ direction according to the equation $E(k) = E_0 - \frac{1}{2}\sqrt{(E_{gap}^2 + 4t^2(1 + 4 \cdot \cos(\frac{ka_{BN}}{2}) + 4 \cdot \cos^2(\frac{ka_{BN}}{2}))}$ led to a best fit where E_0 = -0.91 eV is the center energy of the gap, E_{gap} = -3.94 eV the energy width of the gap, $a_{BN} = 2.51 \pm 0.01$ Å the lattice constant, and $t = 2.68$ eV the hopping parameter. The lattice constant differs by 0.5% from the one of bulk h-BN which is 2.50 Å [61]. The corresponding $\overline{K}$ point of the h-BN layer is found as $k_{\overline{K},BN} = \frac{4\pi}{3a_{BN}} = 1.670 \pm 0.013$ Å^{-1}.

The mismatch observed in the photoemission data is therefore 1.4% which is close to the mismatch of two free standing layers of 1.6%. We thus find that the two systems are electronically decoupled, except for charge transfer into the graphene sheet, with each layer following its own periodicity also in reciprocal space. The emergence of new Dirac points in the band structure due to backfolding processes, involving moiré reciprocal lattice vectors, as previously seen on randomly oriented graphene flakes on h-BN by Yankowitz et al. [86], was not observed in the present work. This might be related to the good alignment of the graphene layer with respect to the h-BN layer, leading to very long moiré periodicities. Misorientation angles smaller then 0.5° yield reciprocal lattice vectors smaller then 0.05 Å^{-1} and are therefore within the experimental linewidths measured on our samples (Fig. 4.6a).

In conclusion, we have demonstrated a direct CVD growth of a g/h-BN stack on a Cu(111) surface. The graphene layer adopts the lattice orientation of the preformed h-BN monolayer and grows incommensurate with a lattice constant similar to that of graphite, which leads to a characteristic moiré pattern in STM images. XPS/XPD and ARPES data show that the underlying h-BN layer is not damaged during the graphene forming CVD process. The graphene π band does not show a band gap at the $\overline{K}$ point of the Brillouin zone that has been predicted for the commensurate system [85], where the equivalence of the two carbon atoms in the graphene lattice is lifted. The incommensurate growth effectively preserves this equivalence over large areas thanks to the very long coherence lengths of the electrons in graphene [87, 88].

Methods

All experiments were performed at room temperature in an ultra-high vacuum (UHV) system based on a user-modified Vacuum Generators ESCALAB 220 [17]. For x-ray photoelectron spectroscopy (XPS) studies a monochromatised Al K_α x-ray source was used, providing photons with an energy of $h\nu = 1486.6$ eV. ARPES data were measured with a microwave driven He plasma lamp equipped with a toroidal grating monochromator tuned to the He IIα line ($h\nu = 40.8$ eV). The STM experiments were carried out in a Park Scientific VPII instrument, attached to the same UHV system, using W tips. The Cu(111) single crystal was cleaned with repetitive cycles of Ar sputtering and annealing up to 1120 K, with intermediate oxygen exposures in order to remove carbon impurities. Single layers of h-BN were prepared by CVD of borazine at a pressure of $p = 5 \cdot 10^{-6}$ mbar, at a sample temperature of 1050 K. The thus formed layer was then usually characterized by LEED and ARPES, the latter for the appearance of the typical h-BN σ band appearing at normal emission [83]. CVD growth of the graphene layer was done using 3-pentanone ($C_2H_5COC_2H_5$) as precursor [75], supplied at a pressure of $p = 2.2$mbar and a substrate temperature of 1100 K, for a total exposure of about 10^9 L (1 Langmuir $= 1 \cdot 10^{-6}$ torr $\cdot$ s). Before introducing the 3-pentanone and borazine vapors to the UHV system, the stock was further purified by freezing/melting/pumping cycles.

Chapter 5

Graphene on h-BN Nanomesh

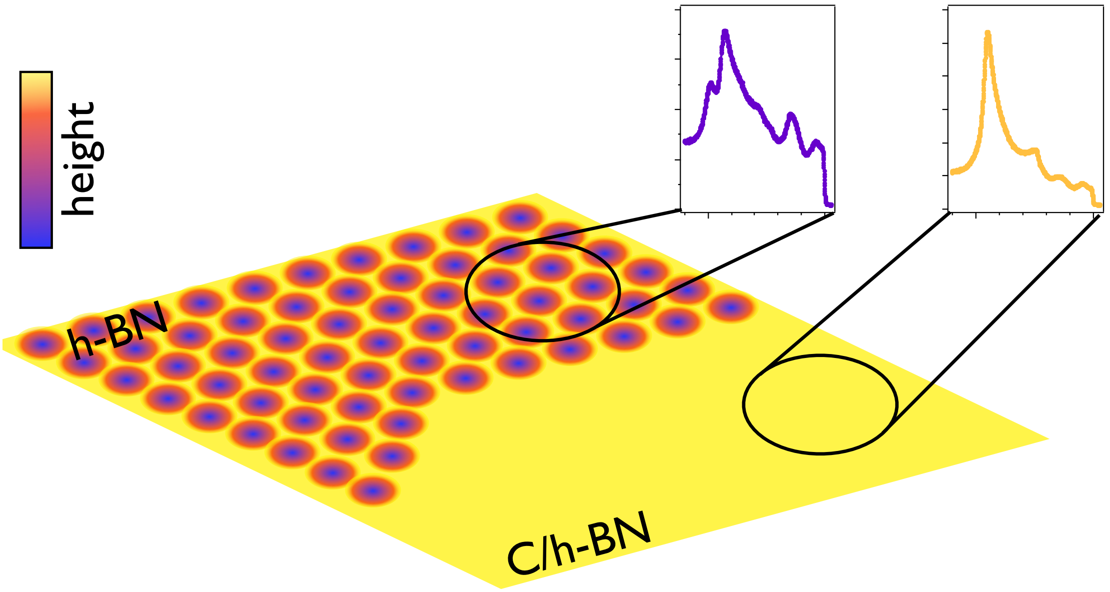

Abstract

The nanomesh is a h-BN monolayer on Rh(111). The lattice mismatch of h-BN and rhodium leads to a characteristic corrugation of h-BN. This Chapter describes a two step CVD process for graphene formation on h-BN/Rh(111). The process is schematically illustrated in the Figure below (see Fig. 5.1). In a first step, carbon dissolves in the Rh bulk. The h-BN layer gets decoupled from the Rh(111) surface. This is reflected in the electronic band structure, where the band splitting vanishes. In a second step, a graphene layer is formed on the flat h-BN layer. The graphene layer grows incommensurate and highly oriented. The formation of graphene/h-BN on rhodium opens the door to large area high quality heterostacks since Rh thin film single crystalline substrates are available in large dimensions.

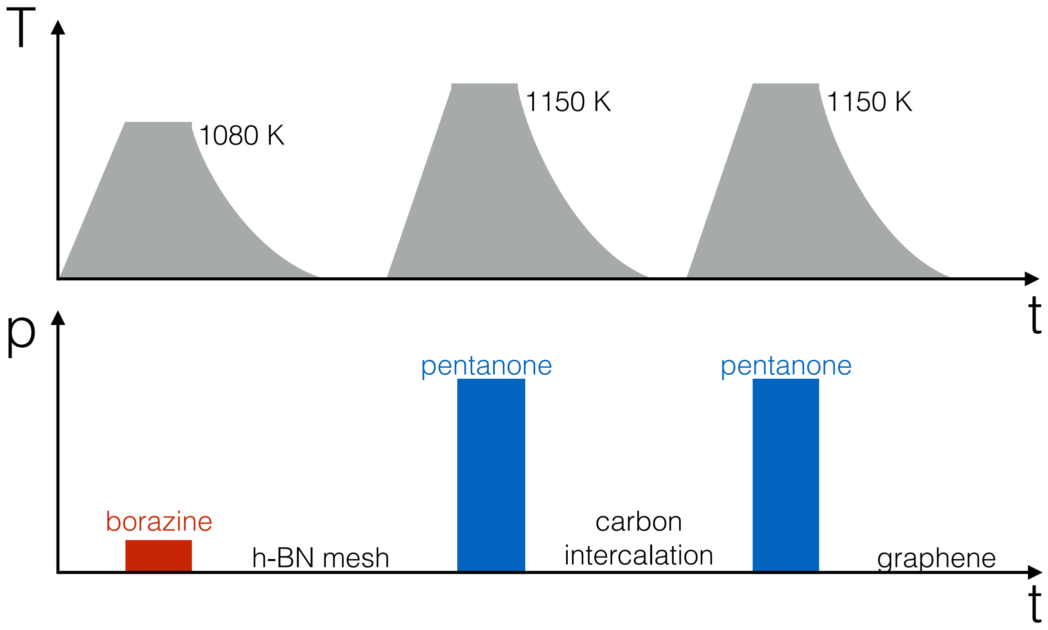

Figure 5.1: **Multi step formation process** Under exposure to borazine, a h-BN nanomesh is formed. Consecutive 3-pentanone exposures lead to first carbon intercallation between h-BN and the Rh surface as well as carbon diffusing inside the Rh bulk. A graphene layer is formed during the second 3-pentanone exposure.

Synthesis of single layer graphene on insulating substrates such as h-BN demands different process parameters than the synthesis on metal surfaces, since no metal catalyst is available during the formation process. As shown in Ch. 4, and by the Oshima group [22, 23, 65], the synthesis is possible under high pressure of carbon containing gases. However, the h-BN substrates used in these experiments were h-BN single layers, grown on either Ni(111) or Cu(111), where the h-BN layer shows little or no corrugation. Corrugated h-BN layers such as the h-BN nanomesh [45] may offer new phenomena such as substrate induced band gaps or highly preferential alignments. In addition, four-inch Si(111) wafers with high quality single crystalline Rh(111) films are available which are stable up to high process temperatures and can therefore provide high quality h-BN/Rh(111) substrates for supporting graphene.

The exposure of the hot Rh(111) surface (T=1080 K) to borazine (p $= 4 \cdot 10^{-7}$ mbar) results in the formation of a single h-BN layer [45, 89]. The lattice mismatch of h-BN and the Rh(111) surface leads to a corrugated superstructure with a periodicity of 3.2 nm [45, 89]. This can be observed in the appearance of additional spots in the LEED pattern, Fig. 5.3a. The main Rh diffraction spots are surrounded in a six-fold symmetric arrangement of superstructure spots corresponding to the 13x13 on 12x12 superstructure of the h-BN nanomesh on Rh(111).

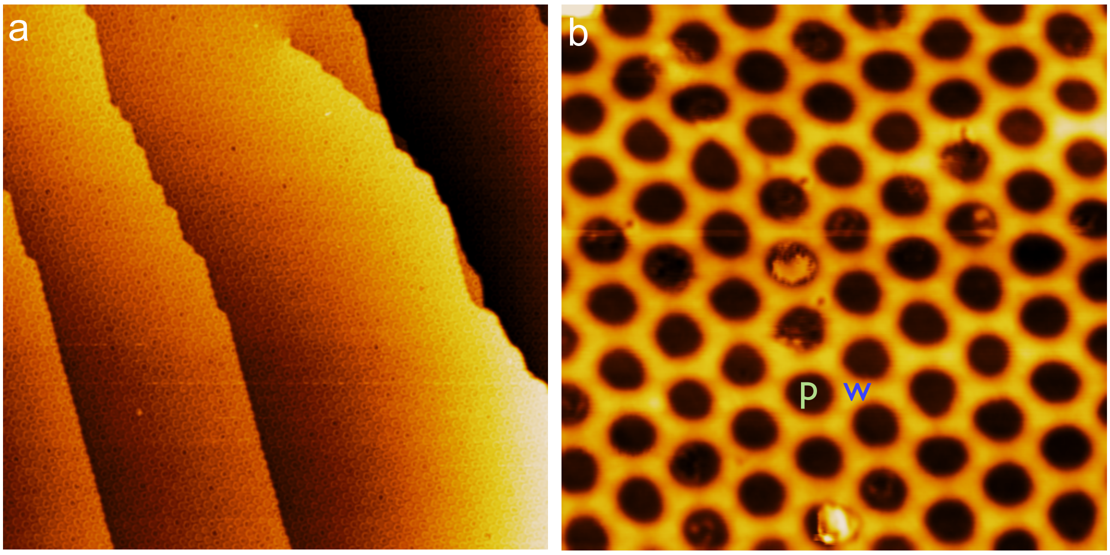

Figure 5.2: **Nanomesh** (a) STM image from a h-BN nanomesh on Rh(111). Tunneling parameters $I_t = 0.4V$, scanning field $200 \times 200nm$. (b) Low temperature STM image of h-BN nanomesh on Rh(111). Tunneling parameters $I_t = 0.4V$, scanning field $30 \times 30nm$. The pore sites "p" and the wire "w" are indicated.

Fig. 5.2 shows a STM image of the h-BN nanomesh on Rh(111). The corrugated surface consists of so called "wires", loosely bonded areas, where the spacing of the BN layer to the metal surface is larger than in the "pore" areas, where the BN layer is more strongly bonded to the surface. The topographic structure influences the electronic band structure. The $\sigma-$ and the $\pi-$bands are split (Fig. 5.10a, c). In normal emission, the $\pi_\alpha-$band is at a binding energy of 8.6 eV, while the more strongly bonded $\pi_\beta-$band is roughly 1.2 eV higher, at 9.8 eV.

Exposing the nanomesh at a temperature of 1150 K to 3-pentanone at a pressure of 2.2 mbar leads to a deposition of carbon. Fig. 5.4 shows photoemission spectra of B 1s, N 1s, Rh 3d, and C 1s core levels before and after 3-pentanone exposure, measured at normal emission. Comparing the peak intensities, normalized by photo-ionization cross sections, reveals the atomic ratios of the elements within the top layers. On a clean h-BN/Rh(111) surface the photoemission signals from B 1s and N 1s core levels correspond to a stoichiometric ratio of 1 : 1, while an atomic ratio of 0.22±0.01 is found for N : Rh and B : Rh.

After the subsequent exposure to 3-pentanone, a carbon peak corresponding to an atomic ratio $(N + B) : C$ of 0.83 is found. At a first glance, this suggests a complete carbon layer on top of the h-BN layer. However, the atomic ratio of the $(B + N) : Rh$ did not remain constant, but increased from 0.44 to 0.64. Furthermore, the absolute photoemission intensity of the B 1s core level has increased by 40%, and N 1s by 47%, while the emission of the Rh 3d core level from the substrate has grown by 30%. These findings are difficult to reconcile with a simple over-layer model. Nor can the change of the atomic ratio between the h-BN layer and the Rh substrate be explained by the different inelastic mean free paths inside a carbon film for the respective core levels, since the kinetic energy of Rh 3d photoelectrons lies between those of B 1s and N 1s.

Forward focusing via photoelectron diffraction could be a mechanism for enhancing photoemission intensities by an over-layer. To understand the described changes in the XPS signals, XPD patterns from the C/h-BN/Rh(111) surface were taken for B 1s, N 1s and C 1s core levels (Fig. 5.5). The B 1s and N 1s diffraction patterns mainly show six interference fringes resulting from in-plane scattering within the h-BN layer. Similar results were found for h-BN/Ni(111) [79]. Thus their angular distribution does not seem to be disturbed by the carbon layer, as previously reported for graphene on h-BN/Cu(111), Cha. 4 and[90].

In Fig. 5.5d, the photoemission intensity ratio of N 1s and C 1s core levels is shown for polar angles between 0° and 82° averaged over all azimuthal angles. Despite local maxima the ratio remains more or less constant, and does not indicate either carbon or nitrogen emission to be clearly dominant at grazing emission angles. In comparison to g/h-BN/Cu(111) where the the ratio C/N clearly shows that the top layer consists of carbon, the element distribution within the top layers remains unexplained.

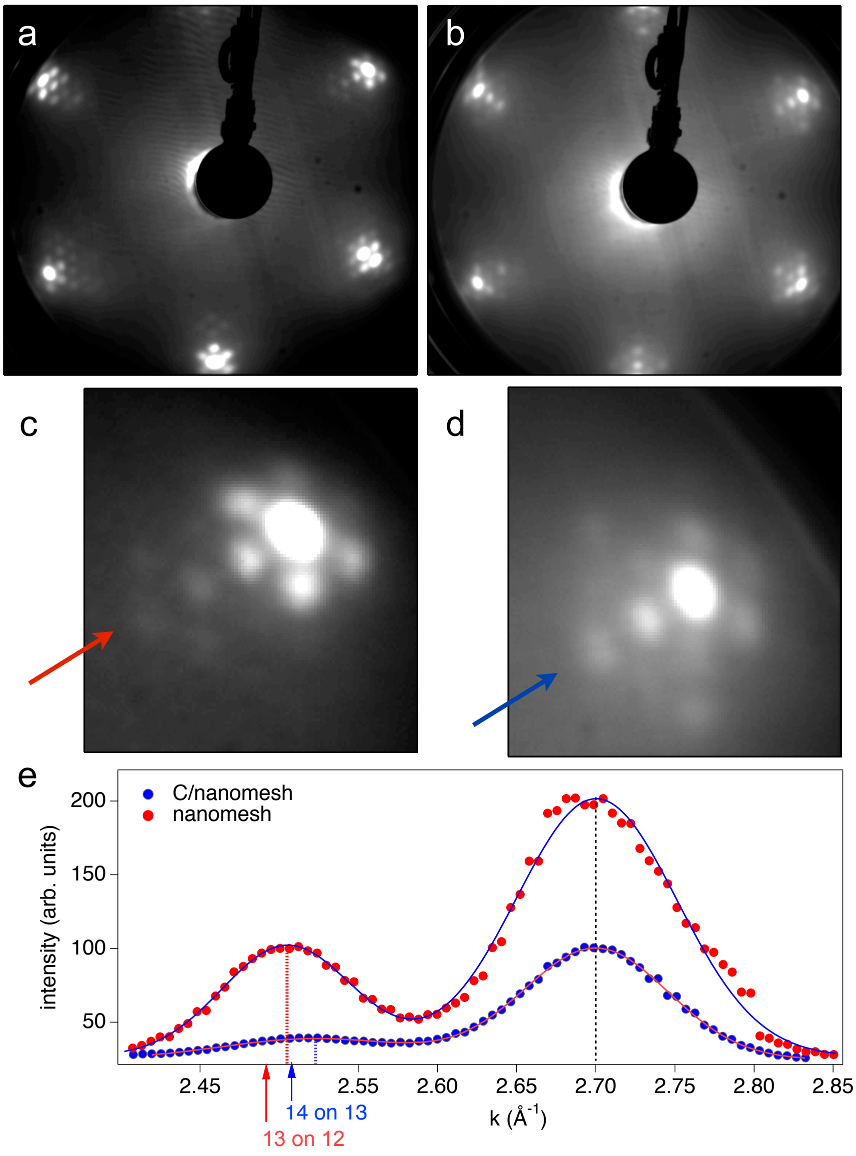

Figure 5.3: **LEED** Low-energy electron diffraction (70 eV) from h-BN/Rh(111) (a), and C/h-BN/Rh(111) (b). Close-up on a single group of diffraction spots for h-BN/Rh(111) (c) and C/h-BN/Rh (d). The arrows indicate the trace of the radial cut shown in (e) through the main diffraction spots containing the first order superstructure spots. To determine the peak positions, two Gaussians were fitted to the data with a linear background. The dotted lines show the positions of the Gaussians. The arrows indicate the theoretical positions for 13 on 12 and 14 on 13 superstructures. The shift of the diffraction spot fits the theoretical shift.

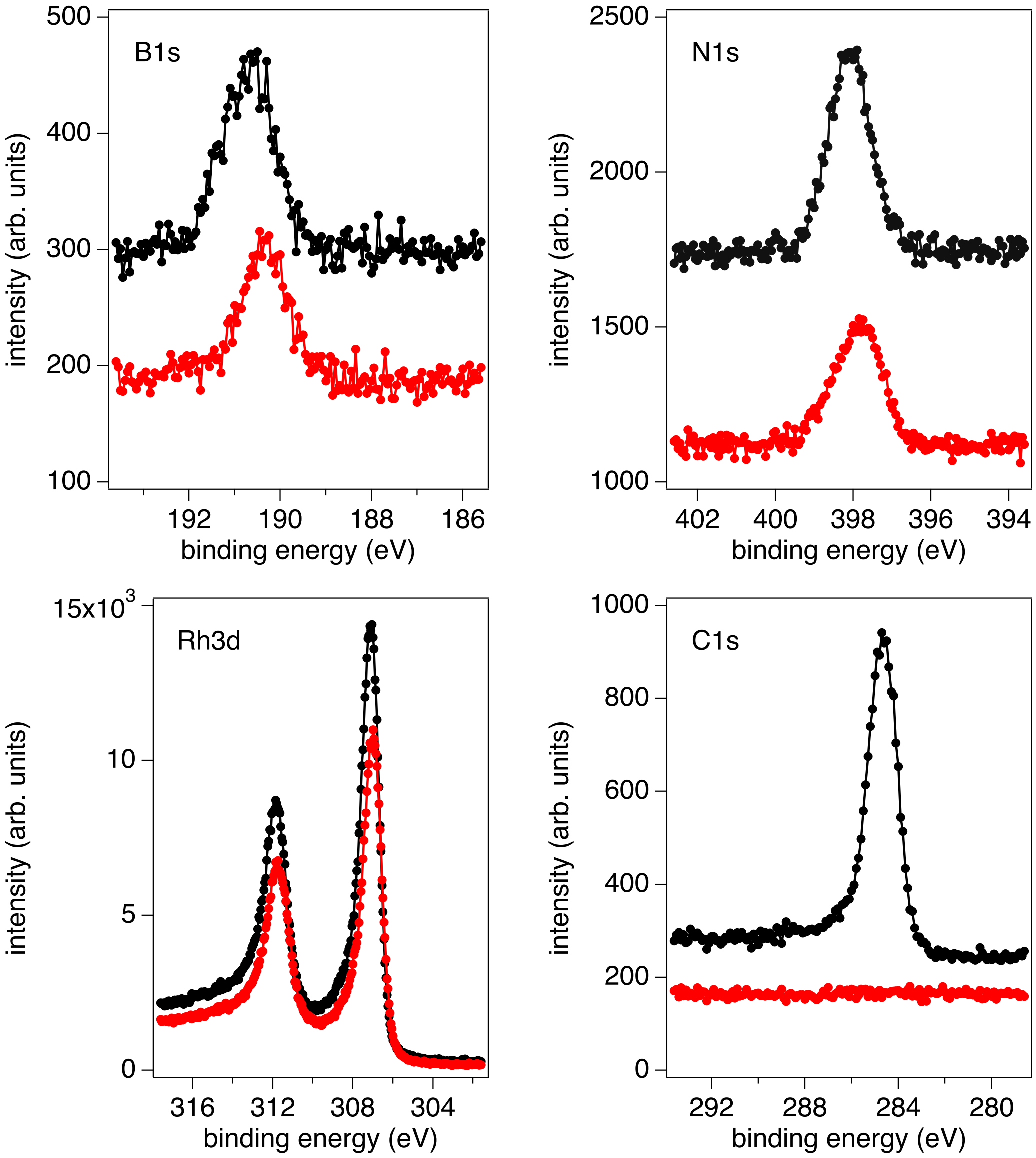

Figure 5.4: **Core level photoemission** Alk_α excited photoemission of B 1s (a), N 1s (b), Rh 3d (c), and C 1s (d) core levels from h-BN/Rh(111) (red) and C/h-BN/Rh(111) (black). All data have been measured at normal emission.

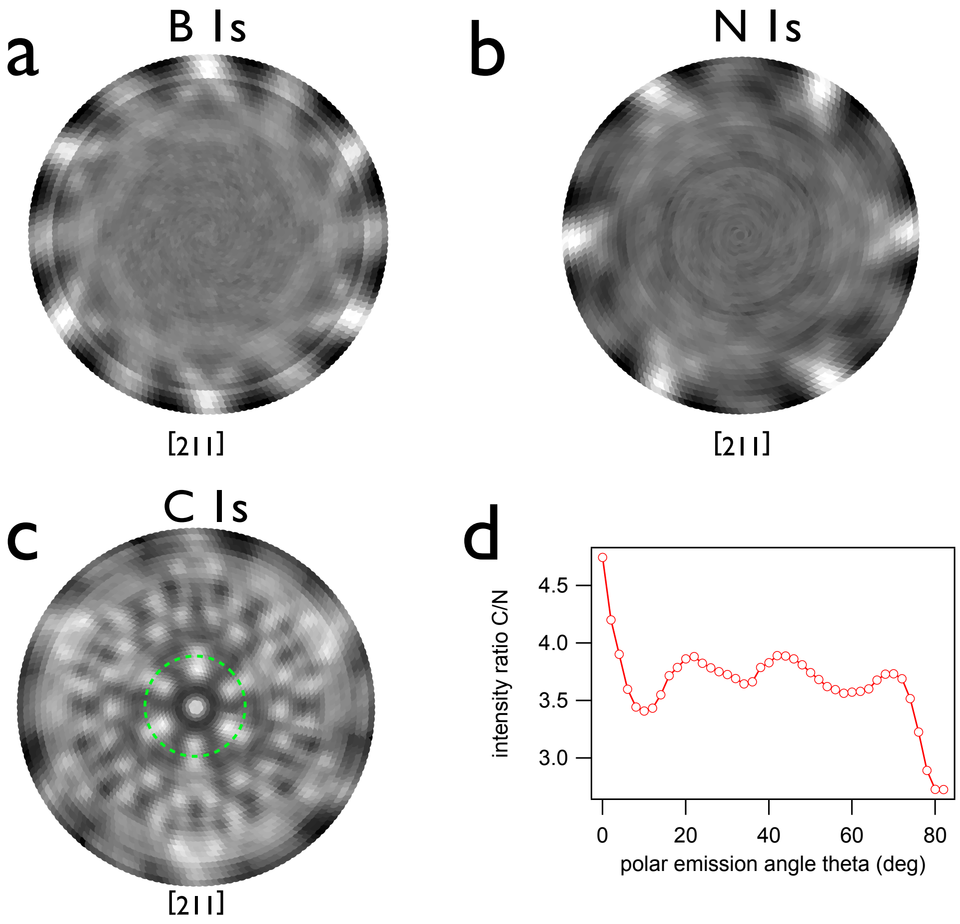

Figure 5.5: **X-ray photoelectron diffraction** Photoelectron diffraction patterns of B 1s (a), N 1s (b) and C 1s (c) core levels from C/h-BN/Rh(111). The data are displayed in a stereographic projection, ranging from normal emission to 82°. The data have been normalized with a Gaussian background. The green circle in (c) indicates a polar angle of 23°, corresponding to an inter-plane forward scattering angle in bulk graphite. (d) Azimuthally averaged photoemission ratio $I_{C1s} : I_{N1s}$ as a function of polar angle.

The C 1s core level shows a much more complex diffraction pattern: a strong forward focussing peak in normal emission ($\theta = 0°$) and six forward scatterers at $\theta = 23°$. In comparison to g/h-BN/Cu(111), were the diffraction shows strong in-plane scattering, these data seem to be dominated by scattering in a multi-layer structure. The polar angle of 23° where characteristic forward scattering peaks are observed is in agreement with the Bernal stacking and an inter-plane distance of 3.3 Å in bulk graphite. On the other hand, the carbon signal lacks the expected 6-fold symmetric interference fringes, which have their origin from in-plane scattering of the photoelectrons in a honeycomb lattice, which had been observed for graphene on h-BN/Cu(111) [90] and graphene on Rh(111) (Fig. 3.5). Therefore the adsorbed layer can not be of graphene type, at least not as a single layer.

In order to explain these findings, we assume a two-phase carbon model, with multi-layer graphite flakes on top of the h-BN layer and single carbon atoms dissolved in the top layers of the Rh substrate. **M**ultiple **S**cattering **C**luster (MSC) calculations for a graphite cluster containing three carbon layers with 31 atoms each (Fig. 5.6b) were carried out. In each layer, two central atoms, one from each sublattice, are used as emitters. The individual diffraction patterns from each layer were summed up, and the result is displayed in Fig. 5.6a.

The C 1s XPD pattern in Fig. 5.5c (shown for convenience also in Fig. 5.6f) can not be reproduced with either the simulated emission pattern of graphite (Fig. 5.6a) nor with the one from dissolved carbon (Fig. 5.6c) alone. But the sum of the two patterns, with a three times stronger weight for the graphene flakes (5.6e), reproduces the experimental finding rather well. These data therefore suggest a rather complex and inhomogeneous morphology for this system.

The diffraction pattern arising from single carbon atoms inside the Rh crystal is shown in Fig. 5.6c. These calculations were done with a **S**ingle **S**cattering **C**luster code [91]. The emitting atoms are located at the tetrahedral adsorption sites shown in Fig. 5.6c. The diffraction pattern from carbon occupying the octahedral adsorption site as sketched in Fig. 5.7a gives a different diffraction pattern (Fig. 5.7b). The sum of the pattern from the octahedral adsorption site and from graphite is shown in Fig. 5.7c. It does not resemble the experimental findings as good as the diffraction pattern from the tetrahedral site.

The increase of the photoemission signals of the B 1s, N 1s and Rh 3d core levels after the CVD carbon deposition still needs to be explained. One candidate mechanism could be forward scattering through carbon atoms. Fig. 5.8c shows a SSC simulation for a polar scan of Rh 3d photoemission from a clean Rh(111) cluster and from a carbon terminated cluster with C atoms in tetrahedral interstitial sites (Fig. 5.8d). In normal emission, the carbon enriched crystal shows a slightly higher intensity compared to the pristine Rh crystal. In normal emission, an increase of 13 % is observed. The discrepancy to the experimental finding of a 30 % increase remains unexplained at this point. A second candidate mechanism

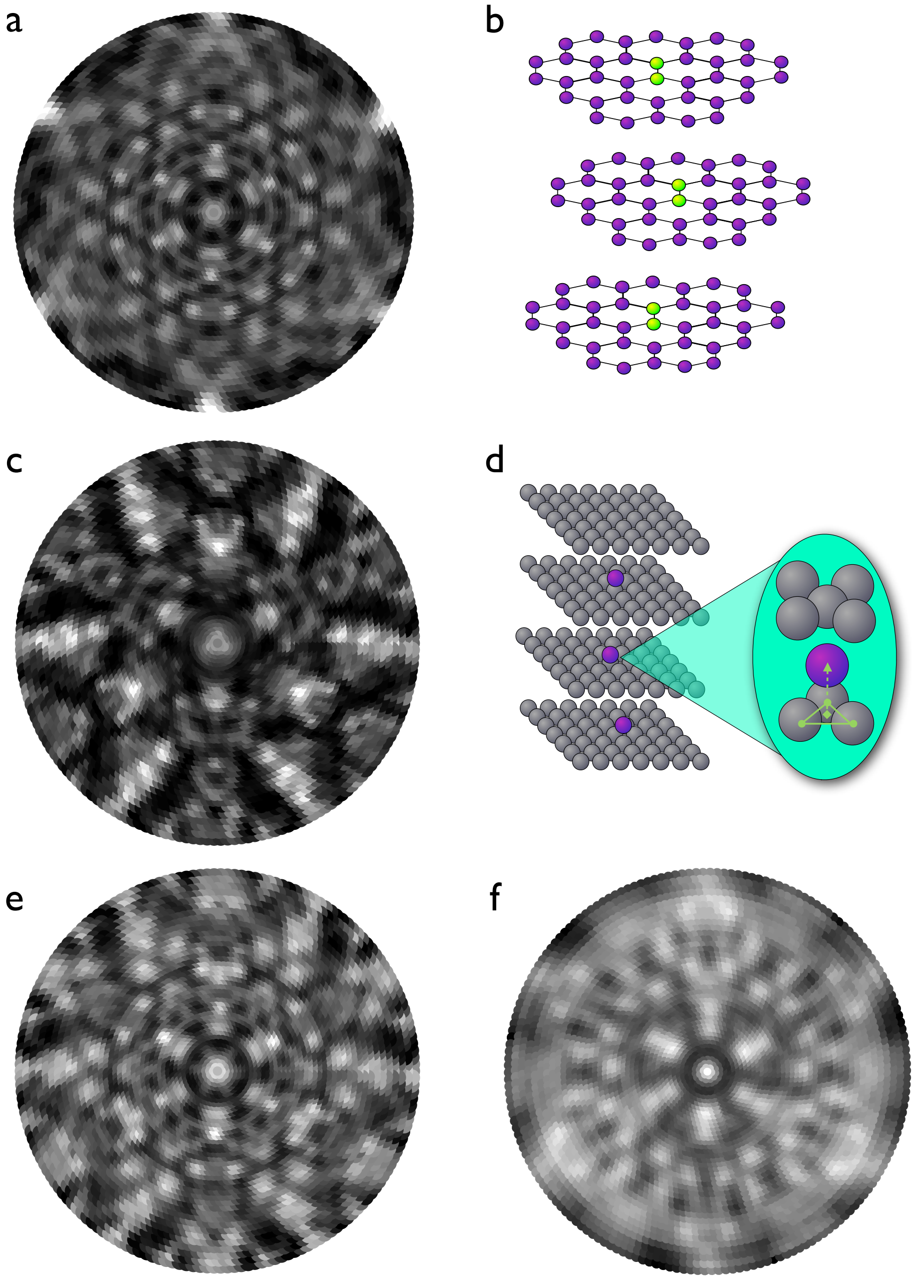

Figure 5.6: **Calculated diffraction patterns** Multiple scattering calculations for the C 1s core level from a three-layer Bernal stacked graphite cluster shown in (b). The data result from the sum of two emitters in each layer, one from each sublattice. The emitters are highlighted in green. The data are displayed in a stereographic projection, ranging from normal emission to 82°, and normalized with a Gaussian background. (c) Single scattering calculations for the C 1s core level from carbon atoms placed at tetrahedral sites inside a Rh cluster. The cluster is shown in (d) with the emitter positions shown in the scheme. The carbon atoms (purple) occupy the tetrahedral adsorption site, the center of the circumscribed sphere. (e) Diffraction pattern resulting from summing the patterns (a) and (c) in a ratio of (a) : (c) = 3 : 1. (f) Photoelectron diffraction patterns of C 1s core level from C/h-BN/Rh(111), for convenience shown again.

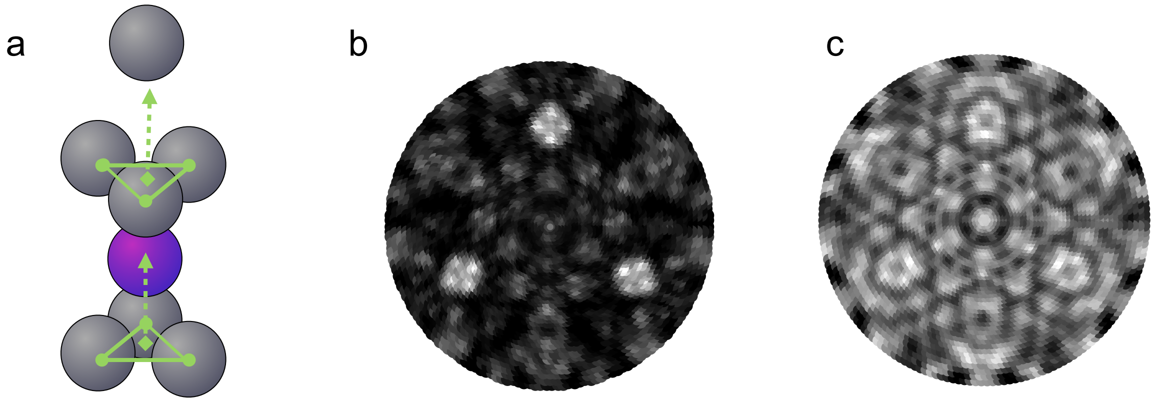

Figure 5.7: **Octahedral adsorption site** (a) Schematic position of the octahedral adsorption site. (b) Single scattering calculations for the C 1s core level from carbon atoms placed at the octahedral sites inside a Rh cluster. (c) Diffraction pattern resulting from summing the pattern (b) and that from graphite (Fig. 5.6a) in a ratio of $C_{graphite} : \mathrm{C}_{octa} = 3 : 1$.

is a possible change of the electron inelastic mean free path inside the carbon enriched rhodium crystal. An increase of the inelastic mean free path could explain the experimental findings.

The increase of the B 1s and N 1s signals shown in Fig. 5.4 could potentially be explained by the forward scattering of B 1s and N 1s photoelectrons when propagating through multi-layered graphite flakes covering parts of the surface. Fig. 5.8a shows a simulated polar angle dependent photoemission signal from a 3-layer scan of C 1s emission from a three-layer honeycomb cluster. Subsurface layers show an increased photoemission signal in normal emission due to forward scattering in the layers above. In an incommensurate system, these forward scattering directions are spread out over a large variety of polar emission angles due to the changing local registry of the layers.

This would completely smear out any forward scattering anisotropies for h-BN through graphite flake scattering processes, consistent with the B 1s and N 1s XPD data of Fig. 5.5, and it is not clear whether any enhancement would survive. In order to have a strong amplification effect, the flakes need to be small enough to mainly have an on top registry to the B and N atoms. An enhancement of the signal is seen in a polar angle range from 0° to 8°. This limits the graphite flakes to be very small, in the order of a few single carbon atoms.

Large area STM images show that a highly regular structure forms over the crystal terraces, Fig. 5.9a. The terraces are partially covered with residues, presumably the graphite flakes discussed earlier. This explains the mainly unchanged C 1s / N 1s ratio in the polar angle

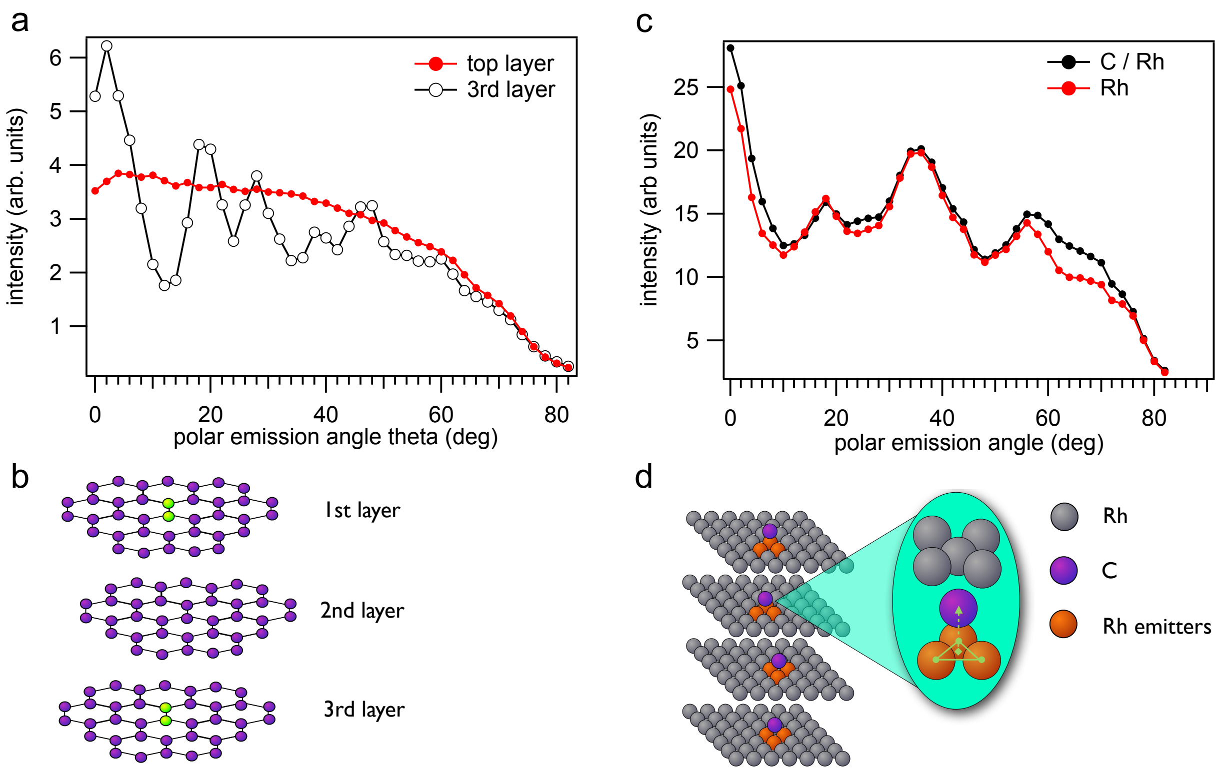

Figure 5.8: **Photoemission enhancement** (a) MSC simulation for C 1s core level photoemission from a three layer honeycomb cluster (b), showing polar scans for emitters placed in separate layers (commensurate stacking). Forward scattering increases the photoemission around normal emission for sub-surface layers. (c) SSC simulation for Rh 3d photoemission for a pristine Rh(111) cluster and for C/Rh(111) (cluster panel (d)) where carbon atoms at the tetrahedral positions increase the normal emission intensity due to forward scattering.

dependent XPS. In areas clear of residues, a regular hexagonal structure spreading over many terraces is found (Fig. 5.9b). This structure is shown in more detail in Fig. 5.9c. A periodicity of 3.6 ± 0.1 nm is extracted from the line profile which differs from the original nanomesh superstructure by 0.4 nm. The periodicity can be explained by a moiré resulting from a decoupled h-BN layer with reduced corrugation amplitude and the Rh(111) surface. Superimposing the surface lattice of Rh (a_{Rh} = 2.687 Å) with the lattice of h-BN (a_{BN} = 2.50 Å) leads to a moiré periodicity of 3.59 nm, corresponding to a matching of 14 x 14 h-BN unit cells on 13 x 13 Rh unit cells.

Carbon atoms dissolved in the Rh(111) crystal occupy tetrahedral surface and subsurface sites in the fcc lattice, as suggested by the comparison between SSC calculations and XPD measurements. The STM image in Fig. 5.9 (d) shows a region of the superstructure with atomic resolution. A periodic hexagonal lattice with a lattice constant of $a = 3.1$ Å is observed. A hypothetical model for this periodicity is shown in Fig. 5.9e. The C/Rh crystal is terminated by a carbon layer. The periodicity and structure is in agreement with a combination of atoms occupying hcp, fcc and on top adsorption sites on the top Rh layer.

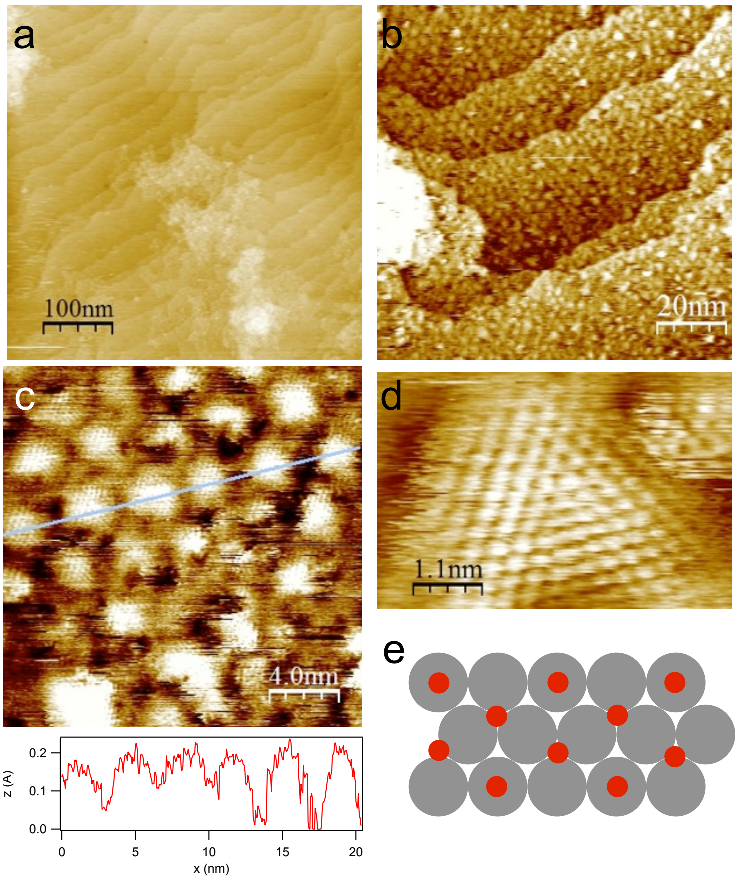

Figure 5.9: **STM** (a) large area survey (500 x 500 nm) showing the covered surface terraces and some irregular carbon residues. (b) 100 x 100 nm zoom-in showing uniform hexagonal superstructure formation over the whole terraces. (c) 20 x 20 nm close-up with a line profile, illustrating the moiré periodicity of 3.6 ± 0.1 nm. (d) close-up on a single moiré supercell. On this scale, the lattice has a periodicity of 3.1 Å. (e) model of the carbon reconstruction (red) on the Rh(111) surface (grey).

The change in the superstructure periodicity can be seen in the LEED data of Fig. 5.3e. At a close look, k_{BN} shifts from 2.505 ± 0.002 Å^{-1} to 2.523 ± 0.001 Å^{-1}. This corresponds to a change in the superlattice of 7.7%, which is in agreement with a superstructure change from 13 on 12 to 14 on 13 h-BN on Rh(111) unit cells.

The adsorption of carbon into the Rh bulk at high temperatures, as well as carbon segregating to the surface during the cool down process has been observed for Rh[92, 93] and other transition metals [92, 94]. Furthermore it has been observed that under formation of surface carbides, the interaction between the surface and adsorbents is modified [92].

The insertion of carbon into the subsurface of Rh(111) and between the top rhodium layer and h-BN, is also reflected in the electronic bands of the h-BN layer. When exposing the h-BN/Rh(111) surface at 1150 K to 3-pentanone at conditions as mentioned above, the more strongly bonded $\sigma_\beta-$ and the $\pi_\beta-$bands (Fig. 5.10) disappear, while the $\sigma_\alpha-$ and the $\pi_\alpha-$bands gain intensity (Fig. 5.10b).

A scenario of an intercalated carbon layer between the h-BN layer and the Rh(111) surface forming an intercalated graphene layer, would be a possibility to explain the intensity gain of the $\pi_\alpha-$band. An additional $\pi-$band resulting from that graphene layer with a large bandgap similar to the case of g/Ni(111) where the strong sublattice asymmetry opens a bandgap of 3.3 eV [21], would lead to an increase of the photoemission intensity of the $\pi_\alpha-$band of h-BN. However, this scenario can be excluded at this point. The XPD pattern, (Fig. 5.5c) lacks the interference fringes at grazing emission angles. Therefore, no graphene and no additional $\pi-$band is formed.

The enhancement of the photoemission signal from the $\alpha-$band can therefore only be explained by a degeneracy of the $\alpha-$and the $\beta-$bands in the h-BN layer. The intercalated carbon does not show a honeycomb structure, but weakens the coupling of the h-BN to the Rh(111) surface, such that the nanomesh pore regions become weakly bonded, as at the wire sites. This causes the $\pi_\alpha-$band and the $\pi_\beta-$band to collapse at the energetic position of the original $\pi_\alpha-$band. While h-BN/Cu(111), and h-BN/Ni(111) (data not shown) remain unchanged under the exposure of 3-pentanon under these conditions, the h-BN on Rh(111) undergoes changes in its electronic structure and topography. The h-BN layer looses its corrugated nanomesh character and becomes similar to flat h-BN systems such as h-BN/Cu(111).

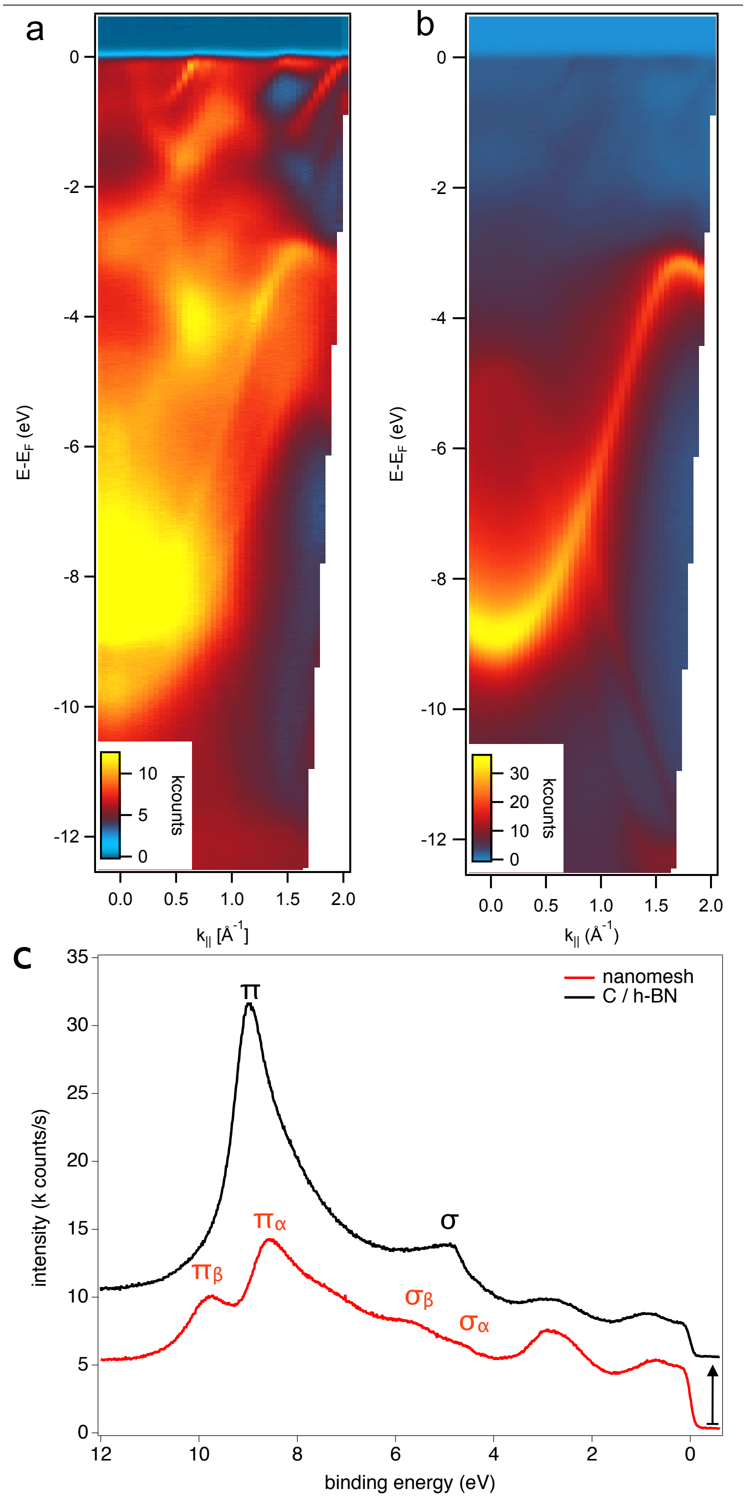

Figure 5.10: **Electronic band dispersion** ARPES data along the $\overline{\Gamma K}$ direction of the two-dimensional Brillouin zone of h-BN/Rh(111) (a) and C/h-BN/Rh(111) (b), excited with HeII_α radiation. (c) spectra in normal emission of h-BN and C/h-BN.

A second high pressure exposure of C/h-BN/Rh(111) leads to the growth of a new top layer of carbon. The change in the carbon top layer can be seen in the XPD pattern. The C 1s XPD pattern in Fig. 5.11 now shows interference fringes, similar to the N 1s pattern, being evident of carbon atoms arranged in a single layer honeycomb pattern. Similar to the case of g/h-BN/Cu(111), the N 1s pattern (not shown) does not exhibit any forward scattering peaks as it would be expected for a commensurate system of g/h-BN.

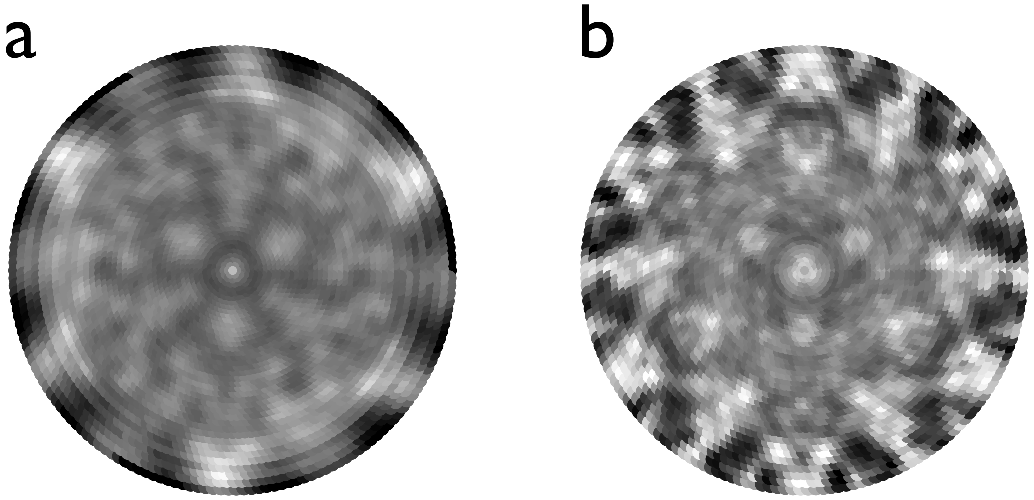

Figure 5.11: **X-ray photoelectron diffraction** (a) Photoelectron diffraction pattern of C 1s from graphene/h-BN/Rh(111). The data are displayed in a stereographic projection, ranging from normal emission to 82°. The data are normalized with a Gaussian background. (b) Simulated diffraction pattern resulting from the sum of a MSC simulated graphene layer and a SSC simulation from carbon dissolved in the Rh crystal.

The formation of the new graphene layer leads to the formation of an additional $\pi-$band as seen in Fig. 5.12. The newly formed band shows a linear dispersion relation when approaching the $\overline{K}$ point of the surface Brillouin zone, and can therefore be identified as a graphene $\pi-$band. Fig. 5.12b shows a detailed scan around the $\overline{K}$ point of the surface Brillouin zone. The graphene π-band does not show a bandgap close to E_F, even though the photoemission intensity is weak in this region due to matrix element effects [27]. The weak intensity of the graphene π-band, and the intersection of the graphene π-band and Rh bands, make the determination of the Dirac point impossible within these data.

To determine the positions of the Dirac point, constant energy surfaces were taken at different binding energies. Fig. 5.13a shows a series of constant energy surfaces as indi-

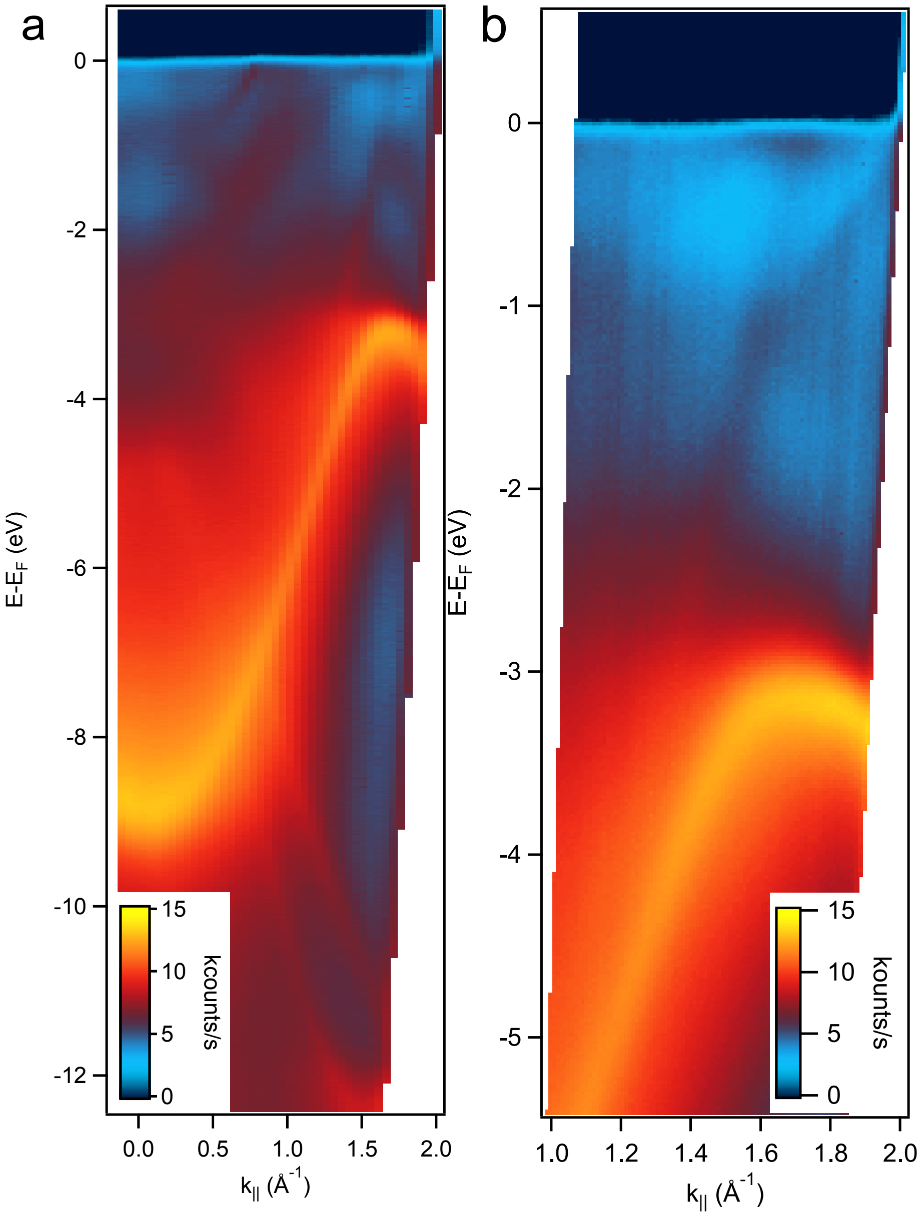

Figure 5.12: **Electronic band dispersion** ARPES data along the ΓK direction of the two-dimensional Brillouin zone excited with He II$_\alpha$ radiation of g/h-BN/Rh (111) (a). (b) shows a detailed scan at the border of the Brillouin zone.

cated in the scheme in Fig. 5.13b. The smallest width of the Dirac cone is observed at $E - E_f$= -0.21 eV. The cuts at $E - E_f$= -0.03 eV and $E - E_f$= -0.38 eV show significantly larger widths. Therefore it can be concluded that the Dirac point is located approximately at $E - E_f$= -0.2 eV. Despite the graphene layer growing incommensurate, similar to g/h-BN/Cu(111) or g/h-BN/Ni(111), the graphene layer is highly oriented. The Fermi surface, Fig. 5.13a shows six distinct Dirac points with a width of 11°. The contributions of domains rotated by 30° are below 10%. In Fig. 5.13d, a close up on a single Dirac cone at E-E$_f$= -1.23 eV is shown. The photoemission intensity distribution is not radial symmetric within the cone. The cone exposes a c-like intensity distribution where due to photoemission matrix element effects one branch of the cone is suppressed, when crossing the boundary from the first to the second Brillouin zone [95].

In conclusion, a two step CVD process is shown for growing graphene on h-BN/Rh(111). In a first step, carbon dissolves into the rhodium substrate, and weakens the interaction of the h-BN layer with the rhodium surface. The h-BN layer looses its corrugation and forms a moiré pattern. This can be seen on the one hand in the LEED pattern, where the size of the superstructure cell changes, and on the other hand in the electronic structure of the h-BN layer, where the corrugation induced band splitting vanishes. In a second high pressure exposure to 3-pentanone, a graphene layer is grown on top of the flat h-BN layer. The graphene band shows no bandgap at the $\overline{K}$ point of the Brillouin zone. This has been previously reported for incommensurate graphene/h-BN systems [90]. The graphene layer shows high azimuthal ordering.

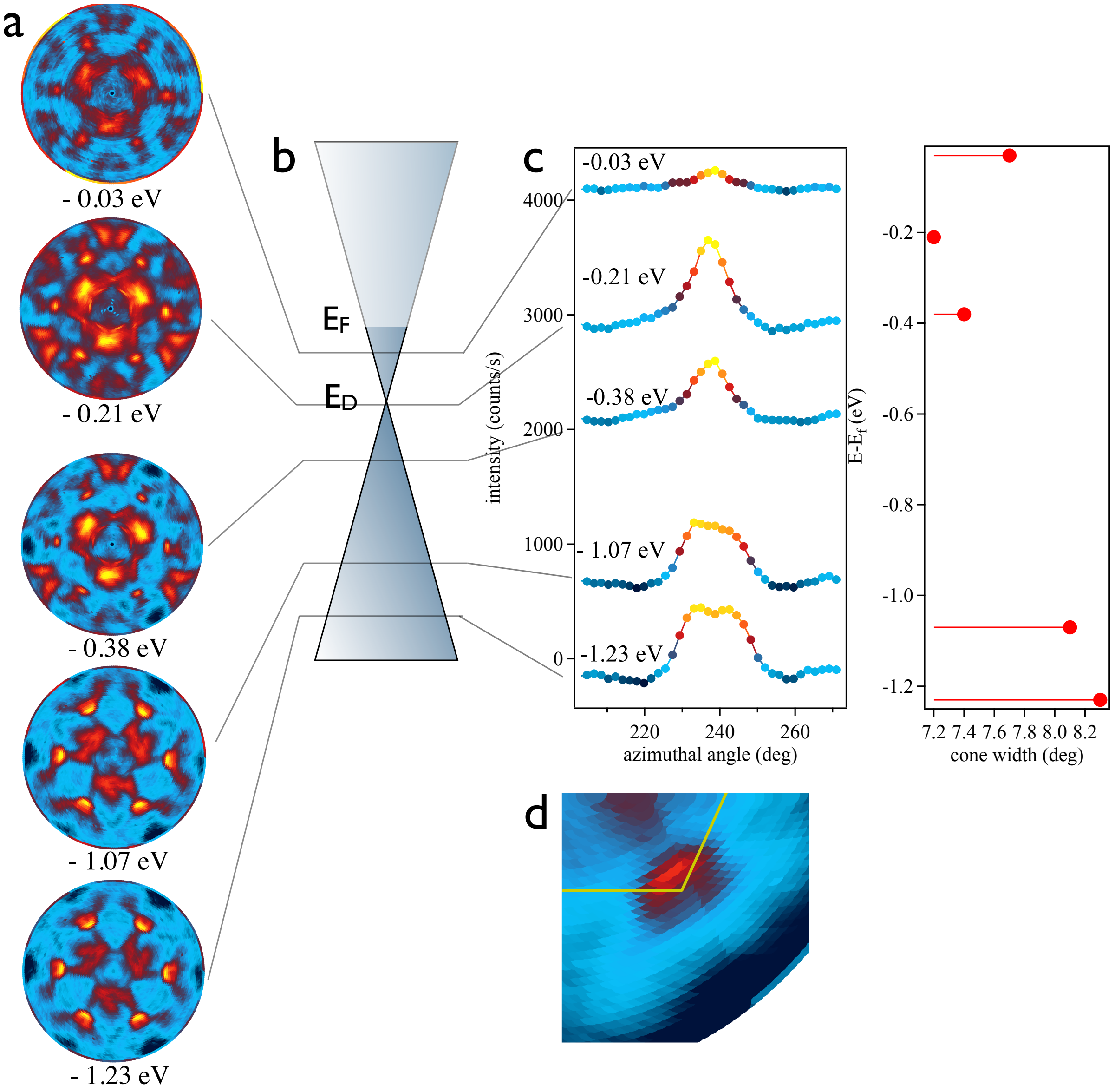

Figure 5.13: **Fermi Surface** a) Series of constant energy cuts through the Brillouin zone. (b) schematic illustration of the Dirac cone with the Dirac point approximately 200 meV below E_f. (c) azimuthal cuts through the Dirac cone at the indicated energies. The according width of the Dirac cone is shown in the right panel. (d) close up on a single Dirac cone at E-E_f= -1.23 eV. The destructive interference of the photoelectrons from the two sublattices gives the Dirac cone a C like shape [27].

Chapter 6

Conclusions and outlook

Conclusions

In this thesis, the formation process of graphene by CVD and its properties was investigated. Graphene growth on Rh(111), a transition metal, graphene on h-BN/Cu(111), which is an uncorrugated dielectric surface, and graphene on h-BN/Rh(111), a strongly corrugated dielectric surface were studied. The results show that the underlying substrate has strong effects on the graphene layer formation and its electronic and structural properties. While a catalytic CVD growth of graphene on a transition metal allows low gas pressures during the formation process, non-catalytic CVD processes demand higher process temperatures and pressures. With the introduction of 3-pentanone as a precursor, higher quality of graphene on Rh(111) was achieved. The resulting graphene layer is highly corrugated and forms a 12 x 12 on 11 x 11 superstructure.

Copper single crystals turned out to be an ideal substrate for graphene / h-BN heterostructures. On Cu(111) highly aligned graphene / h-BN heterostructures were grown. Both layers grow in an incommensurate fashion, meaning each layer keeps its intrinsic lattice constant. The lattice mismatch leads to formation of moiré patterns. The decoupling of the layers is reflected in the electronic band structure of the system. Two different Brillouin zones are observed for the two layers.

The formation of graphene on the corrugated h-BN nanomesh turned out to be not possible under similar preparation conditions. However, a three step CVD process leads to formation of a graphene layer on h-BN/Rh(111). After the growth of h-BN by CVD of borazine, a first carbon exposure leads to carbon absorption in the rhodium substrate and to a weakening of the interaction between rhodium and the h-BN overlayer. The corrugated h-BN layer relaxes and looses its corrugation. In a second CVD step, a graphene layers is grown on top of the h-BN layer. The resulting graphene layer shows high azimuthal ordering and no band gap similar to the g/h-BN/Cu(111) system. Our findings show that both copper and rhodium are good substrates to support graphene / h-BN heterostacks.

Outlook

By growing aligned and high quality graphene on single layer h-BN a first important step towards graphene electronics has been made. To further improve the isolation of graphene from the metal substrate, it is required to increase the thickness of the h-BN layer from single layer to multilayers. Therefore, a method for producing high quality large scale h-BN layers with well defined thickness needs to be found. First experiments show that this is possible with high pressure CVD processes. Exposing the Cu(111) surface to borazine at a pressure of 1.0 mbar at a temperature of 1120 K leads to formation of multilayer h-BN. This can be seen in the intensity gain of the h-BN $\pi-$ and σ bands compared to a single layer as well as the suppression of the d-bands of the copper substrate (Fig. 6.1a). The h-BN layers form crystals with a size up to 500 μm, which can be seen in the confocal optical microscopy image in Fig. 6.2. The azimuthal disorder of the h-BN crystals results in a ring in the LEED pattern in Fig. 6.1b. In a final step, a graphene layer grown on top of these multilayer films would bring a highly desired isolated graphene layer.

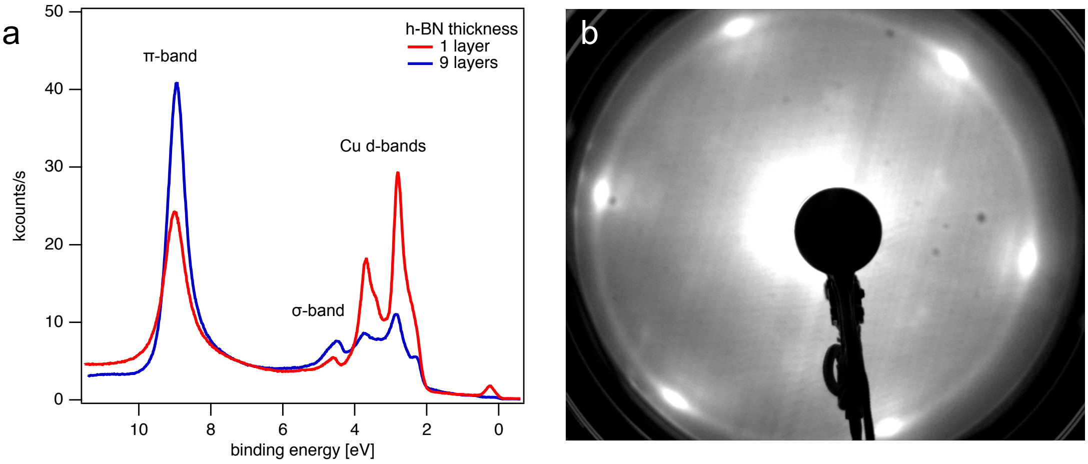

Figure 6.1: **Single and few layer h-BN** Normal emission photoemission spectra from single layer and multilayer h-BN on Cu(111) under HeIIα radiation. The Cu d-bands are suppressed with increasing thickness of the h-BN layer. Low energy electron diffraction from approx. nine layers on Cu(111) (b).

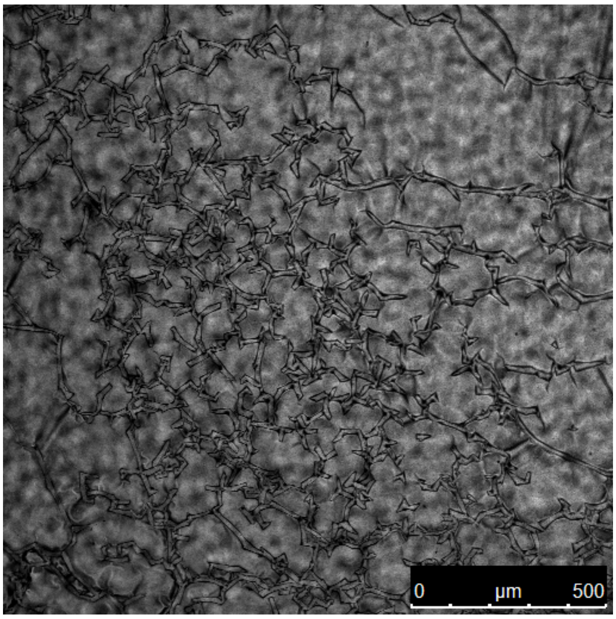

Figure 6.2: **h-BN grain size** Confocal optical microscopy image from an exfoliated multilyer h-BN of approximately 30 layers.

Bibliography

[1] Y M Lin, C Dimitrakopoulos, K A Jenkins, D B Farmer, H Y Chiu, A Grill, and Ph Avouris. 100-GHz Transistors from Wafer-Scale Epitaxial Graphene. *Science*, 327(5966):662–662, February 2010.

[2] Yanqing Wu, Yu-ming Lin, Ageeth A Bol, Keith A Jenkins, Fengnian Xia, Damon B Farmer, Yu Zhu, and Phaedon Avouris. nature09979. *Nature*, 472(7341):74–78, March 2011.

[3] K Novoselov, A Geim, S Morozov, and D Jiang. Electric field effect in atomically thin carbon films. *Science*, 306:666–669, 2004.

[4] Narain D Arora, John R Hauser, and David J Roulston. Electron and hole mobilities in silicon as a function of concentration and temperature. *IEEE transactions on Electron Devices,*, 29(2):292–295, 1982.

[5] Konstantin V Emtsev, Aaron Bostwick, Karsten Horn, Johannes Jobst, Gary L Kellogg, Lothar Ley, Jessica L McChesney, Taisuke Ohta, Sergey A Reshanov, Jonas Röhrl, Eli Rotenberg, Andreas K Schmid, Daniel Waldmann, Heiko B Weber, and Thomas Seyller. Towards wafer-size graphene layers by atmospheric pressure graphitization of silicon carbide. *Nature Materials*, 8(3):203–207, February 2009.

[6] A B Preobrajenski, May Ling Ng, A S Vinogradov, and N Mårtensson. Controlling graphene corrugation on lattice-mismatched substrates. *Physical Review B*, 78(7), August 2008.

[7] Charles E Mortimer. Chemie: Das Basiswissen der Chemie. 2010.

[8] J W Anthony, R A Bideaux, K W Bladh, and M C Nichols. *Handbook of Mineralogy.* Mineral Data Pub. (Tucson, Arizona, USA), 1990.

[9] Lev Davidovich Landau. On the theory of phase transitions. I. *Phys. Z. Sowjet.*, 11:26, 1937.

[10] PR Wallace. The band theory of graphite. *Physical Review*, 71(9):622–634, 1947.

[11] D P Divincenco and E J Mele. Self-Consistent Effective-Mass Theory for Intralayer Screening in Graphite-Intercalation Compounds. *Physical Review B*, 29(4):1685–1694, 1984.

[12] C Oshima, E Bannai, T Tanaka, and S Kawai. Carbon layer on lanthanum hexaboride (100) surface. *Jpn J Appl Phys*, 1977.

[13] J Wintterlin and M L Bocquet. Graphene on metal surfaces. *Surface Science*, 603(10-12):1841–1852, June 2009.

[14] A Nagashima, N Tejima, and C Oshima. Electronic states of the pristine and alkali-metal-intercalated monolayer graphite/Ni (111) systems. *Physical Review B*, 50(23):17487–17495, 1994.

[15] H Hertz. Ueber einen Einfluss des ultravioletten Lichtes auf die electrische Entladung. *Annalen der Physik und Chemie*, 267(8):983–1000, 1887.

[16] A Einstein. Über einen die Erzeugung und Verwandlung des Lichtes betreffenden heuristischen Gesichtspunkt. *Annalen der Physik und Chemie*, 322(6):132–148, 1905.

[17] T Greber, O Raetzo, TJ Kreutz, P Schwaller, W Deichmann, E Wetli, and J Osterwalder. A photoelectron spectrometer for k-space mapping above the Fermi level. *Review of Scientific Instruments*, 68:4549, 1997.

[18] G Binnig. Tunneling through a controllable vacuum gap. *Applied Physics Letters*, 40(2):178–180, 1982.

[19] FJ Himpsel, K Christmann, P Heimann, DE Eastman, and P Feibelman. Adsorbate Band Dispersions for C on Ru(0001). *Surface Science*, 115(3):L159–L164, 1982.

[20] A Nagashima, N Tejima, Y Gamou, T KAWAI, and C Oshima. Electronic-Structure of Monolayer Hexagonal Boron-Nitride Physisorbed on Metal-Surfaces. *Physical Review Letters*, 75(21):3918–3921, 1995.

[21] Yu Dedkov, A Shikin, V Adamchuk, S Molodtsov, C Laubschat, A Bauer, and G Kaindl. Intercalation of copper underneath a monolayer of graphite on Ni(111). *Physical Review B*, 64(3):035405, June 2001.

[22] A Nagashima, Y Gamou, M Terai, M Wakabayashi, and C Oshima. Electronic states of the heteroepitaxial double-layer system. *Physical Review B*, 54:13491, November 1996.

[23] C Oshima, A Itoh, E Rokuta, T Tanaka, K Yamashita, and T Sakurai. A hetero-epitaxial-double-atomic-layer system of monolayer graphene/monolayer h-BN on Ni(111). *Solid State Communications*, 116(1):37–40, 2000.

[24] E Rollings, G H Gweon, S Y Zhou, B S Mun, J L McChesney, B S Hussain, A V Fedorov, P N First, W A de Heer, and A Lanzara. Synthesis and characterization of atomically thin graphite films on a silicon carbide substrate. *Journal of Physics and Chemistry of Solids*, 67(9-10):2172–2177, September 2006.

[25] T Ohta. Controlling the Electronic Structure of Bilayer Graphene. *Science*, 313(5789):951–954, August 2006.

[26] S Y Zhou, G H Gweon, A V Fedorov, P N First, W A de Heer, D H Lee, F Guinea, A H Castro Neto, and A Lanzara. Substrate-induced bandgap opening in epitaxial graphene. *Nature Materials*, 6(10):770–775, September 2007.

[27] Aaron Bostwick, Taisuke Ohta, Thomas Seyller, Karsten Horn, and Eli Rotenberg. Quasiparticle dynamics in graphene. *Nature Physics*, 3(1):36–40, December 2007.

[28] X Z Yu, C G Hwang, C M Jozwiak, A Koehl, A K Schmid, and A Lanzara. New synthesis method for the growth of epitaxial graphene. *Journal of Electron Spectroscopy and Related Phenomena*, 184(3-6):100–106, 2011.

[29] Isabella Gierz, Jürgen Henk, Hartmut Höchst, Christian R Ast, and Klaus Kern. Illuminating the dark corridor in graphene: Polarization dependence of angle-resolved photoemission spectroscopy on graphene. *Physical Review B*, 83(12):121408, March 2011.

[30] AK Geim and KS Novoselov. The rise of graphene. *Nature Materials*, 6:183–191, 2007.

[31] Andrew J Pollard, Edward W Perkins, Nicholas A Smith, Alex Saywell, Gudrun Goretzki, Anna G Phillips, Stephen P Argent, Hermann Sachdev, Frank Mueller, Stefan Huefner, Stefan Gsell, Martin Fischer, Matthias Schreck, Juerg Osterwalder, Thomas Greber, Simon Berner, Neil R Champness, and Peter H Beton. Supramolecular Assemblies Formed on an Epitaxial Graphene Superstructure. *Angewandte Chemie International Edition*, 49(10):1794–1799, 2010.

[32] Xuesong Li, Weiwei Cai, Jinho An, Seyoung Kim, Junghyo Nah, Dongxing Yang, Richard Piner, Aruna Velamakanni, Inhwa Jung, Emanuel Tutuc, Sanjay K Banerjee, Luigi Colombo, and Rodney S Ruoff. Large-Area Synthesis of High-Quality and Uniform Graphene Films on Copper Foils. *Science*, 324(5932):1312–1314, June 2009.

[33] Frank Mueller, Hermann Sachdev, Stefan Huefner, Andrew J Pollard, Edward W Perkins, James C Russell, Peter H Beton, Stefan Gsell, Martin Fischer, Matthias Schreck, and Bernd Stritzker. How Does Graphene Grow? Easy Access to Well-Ordered Graphene Films. *Small*, 5(20):2291–2296, 2009.

[34] Bo Wang, Marco Caffio, Catherine Bromley, Herbert Fruechtl, and RenaId Schaub. Coupling Epitaxy, Chemical Bonding, and Work Function at the Local Scale in Transition Metal-Supported Graphene. *ACS Nano*, 4(10):5773–5782, 2010.

[35] M Sicot, S Bouvron, O Zander, U Rüdiger, YS Dedkov, and M Fonin. Nucleation and growth of nickel nanoclusters on graphene Moiré on Rh (111). *Applied Physics Letters*, 96:093115, 2010.

[36] A Nagashima, H Itoh, T Ichinokawa, C Oshima, and S Otani. Change in the electronic states of graphite overlayers depending on thickness. *Physical Review B*, 50(7):4756, 1994.

[37] I Pletikosic, M Kralj, P Pervan, R Brako, J Coraux, A T N'Diaye, C Busse, and T Michely. Dirac Cones and Minigaps for Graphene on Ir(111). *Physical Review Letters*, 102(5):056808, 2009.

[38] S Marchini, S Günther, and J Wintterlin. Scanning tunneling microscopy of graphene on Ru(0001). *Physical Review B*, 76(7):075429, August 2007.

[39] Yi Pan, Haigang Zhang, Dongxia Shi, Jiatao Sun, Shixuan Du, Feng Liu, and Hongjun Gao. Highly Ordered, Millimeter-Scale, Continuous, Single-Crystalline Graphene Monolayer Formed on Ru (0001). *Adv. Mater.*, 21(27):2777–2780, 2009.

[40] A L Vazquez de Parga, F Calleja, B Borca, M C G Passeggi, J J Hinarejos, F Guinea, and R Miranda. Periodically rippled graphene: Growth and spatially resolved electronic structure. *Physical Review Letters*, 100(5):056807, 2008.

[41] Peter W Sutter, Jan-Ingo Flege, and Eli A Sutter. Epitaxial graphene on ruthenium. *Nature Materials*, 7(5):406, April 2008.

[42] I Forbeaux, JM Themlin, and JM Debever. Heteroepitaxial graphite on 6H-SiC (0001): Interface formation through conduction-band electronic structure. *Physical Review B*, 58(24):16396–16406, 1998.

[43] Thomas Brugger, Sebastian Guenther, Bin Wang, J Hugo Dil, Marie-Laure Bocquet, Juerg Osterwalder, Joost Wintterlin, and Thomas Greber. Comparison of electronic structure and template function of single-layer graphene and a hexagonal boron nitride nanomesh on Ru(0001). *Physical Review B*, 79(4), January 2009.

[44] DG Castner, BA Sexton, and GA Somorjai. Leed and thermal desorption studies of small molecules (H2, O2, CO, CO2, NO, C2H4, C2H2 AND C) chemisorbed on the rhodium (111) and (100) surfaces. *Surface Science*, 71(3):519–540, 1978.

[45] Martina Corso, Willi Auwärter, Matthias Muntwiler, Anna Tamai, Thomas Greber, and Jürg Osterwalder. Boron Nitride Nanomesh. *Science*, 303(5655):217–220, 2004.

[46] FG Requejo, ELD Hebenstreit, DF Ogletree, and M Salmeron. An in situ XPS study of site competition between CO and NO on Rh(111) in equilibrium with the gas phase. *Journal of Catalysis*, 226(1):83–87, 2004.

[47] R Landers, G Kleiman, and SGC De Castro. High energy Auger satellites of the 4d transition metals. *Journal of Electron Spectroscopy and Related Phenomena*, 72:211–215, 1995.

[48] H Ma, Mario Thomann, Jeanette Schmidlin, Silvan Roth, MArtin Morscher, and Thomas Greber. Corrugated single layer templates for molecules: From h-BN nanomesh to graphene based quantum dot arrays. *Frontiers of Physics in China*, 5(4):387–392, 2010.

[49] HG Zhang, H Hu, Y Pan, JH Mao, M Gao, HM Guo, SX Du, T Greber, and HJ Gao. Graphene based quantum dots. *Journal Of Physics-Condensed Matter*, 22:302001, 2010.

[50] Z Klusek, W Kozlowski, Z Waqar, S Datta, JS Burnell-Gray, IV Makarenko, NR Gall, EV Rutkov, AY Tontegode, and AN Titkov. Local electronic edge states of graphene layer deposited on Ir (1 1 1) surface studied by STM/CITS. *Applied Surface Science*, 252(5):1221–1227, 2005.

[51] Marcella Iannuzzi and Juerg Hutter. Surface Science. *Surface Science*, 605(15-16):1360–1368, August 2011.

[52] Andrii Goriachko, Yunbin He, Marcus Knapp, Herbert Over, Martina Corso, Thomas Brugger, Simon Berner, Juerg Osterwalder, and Thomas Greber. Self-assembly of a hexagonal boron nitride nanomesh on Ru(0001). *Langmuir*, 23(6):2928–2931, 2007.

[53] P Sutter, R Cortes, J Lahiri, and E Sutter. Interface Formation in Monolayer Graphene-Boron Nitride Heterostructures. *Nano Lett*, 12(9):4869–4874, September 2012.

[54] Claire Berger, Zhimin Song, Xuebin Li, Xiaosong Wu, Nate Brown, Ce cile Naud, Didier Mayou, Tianbo Li, Joanna Hass, Alexei N Marchenkov, Edward H Conrad,

Phillip N First, and Walt A de Heer. Electronic Confinement and Coherence in Patterned Epitaxial Graphene. *Science*, 312(5777):1191–1196, May 2006.

[55] J Martin, N Akerman, G Ulbricht, T Lohmann, J H Smet, K von Klitzing, and A Yacoby. Observation of electron–hole puddles in graphene using a scanning single-electron transistor. *Nature Physics*, 4(2):144–148, November 2007.

[56] A Deshpande, W Bao, F Miao, C Lau, and B LeRoy. Spatially resolved spectroscopy of monolayer graphene on SiO2. *Physical Review B*, 79(20):205411, May 2009.

[57] Li Gao, Jeffrey R Guest, and Nathan P Guisinger. Epitaxial Graphene on Cu(111). *Nano Lett*, 10(9):3512–3516, September 2010.

[58] Sukang Bae, Hyeongkeun Kim, Youngbin Lee, Xiangfan Xu, Jae-Sung Park, Yi Zheng, Jayakumar Balakrishnan, Tian Lei, Hye Ri Kim, Young Il Song, Young-Jin Kim, Kwang S Kim, Barbaros Özyilmaz, Jong-Hyun Ahn, Byung Hee Hong, and Sumio Iijima. Roll-to-roll production of 30-inch graphene films for transparent electrodes. *Nature Nanotechnology*, 5(8):574–578, 2010.

[59] W Gannett, W Regan, K Watanabe, T Taniguchi, M F Crommie, and A Zettl. Boron nitride substrates for high mobility chemical vapor deposited graphene. *Applied Physics Letters*, 98(24):242105, 2011.

[60] L Britnell, R V Gorbachev, R Jalil, B D Belle, F Schedin, A Mishchenko, T Georgiou, M I Katsnelson, L Eaves, S V Morozov, N M R Peres, J Leist, A K Geim, K S Novoselov, and L A Ponomarenko. Field-Effect Tunneling Transistor Based on Vertical Graphene Heterostructures. *Science*, 335(6071):947–950, February 2012.

[61] W Paszkowicz, J B Pelka, M Knapp, T Szyszko, and S Podsiadlo. Lattice parameters and anisotropic thermal expansion of hexagonal boron nitride in the 10?297.5 K temperature range. *Applied Physics A: Materials Science & Processing*, 75(3):431–435, September 2002.

[62] Monica Pozzo, Dario Alfè, Paolo Lacovig, Philip Hofmann, Silvano Lizzit, and Alessandro Baraldi. Thermal Expansion of Supported and Freestanding Graphene: Lattice Constant versus Interatomic Distance. *Physical Review Letters*, 106(13):135501, March 2011.

[63] Kenji Watanabe, Takashi Taniguchi, and Hisao Kanda. Direct-bandgap properties and evidence for ultraviolet lasing of hexagonal boron nitride single crystal. *Nature Materials*, 3(6):404–409, May 2004.

[64] C. R. Dean, A. F. Young, I. Meric, C. Lee, L. Wang, S. Sorgenfrei, K Watanabe, T Taniguchi, P Kim, K. L. Shepard, and J. Hone. Boron nitride substrates for high-quality graphene electronics. *Nat Nanotechnology*, 5:722–726, September 2010.

[65] T Kawasaki, T Ichimura, H Kishimoto, A Akbar, T Ogawa, and C Oshima. Double atomic layers of graphene/monolayer h-BN on Ni (111) studied by scanning tunneling microscopy and scanning tunneling spectroscopy. *Surface Review and Letters*, 9:1459–1464, 2002.

[66] D Usachov, V Adamchuk, D Haberer, A Grüneis, H Sachdev, A Preobrajenski, C Laubschat, and D Vyalikh. Quasifreestanding single-layer hexagonal boron nitride as a substrate for graphene synthesis. *Physical Review B*, 82(7), August 2010.

[67] C Bjelkevig, Z Mi, J Xiao, and P Dowben. Electronic structure of a graphene/hexagonal-BN heterostructure grown on Ru (0001) by chemical vapor deposition and atomic layer deposition: extrinsically doped graphene. *Journal Of Physics-Condensed Matter*, 22:302002, 2010.

[68] Zheng Liu, Li Song, Shizhen Zhao, Jiaqi Huang, Lulu Ma, Jiangnan Zhang, Jun Lou, and Pulickel M Ajayan. Direct Growth of Graphene/Hexagonal Boron Nitride Stacked Layers. *Nano Lett*, 11(5):2032–2037, May 2011.

[69] Jiamin Xue, Javier Sanchez-Yamagishi, Danny Bulmash, Philippe Jacquod, Aparna Deshpande, K Watanabe, T Taniguchi, Pablo Jarillo-Herrero, and Brian J Leroy. Scanning tunnelling microscopy and spectroscopy of ultra-flat graphene on hexagonal boron nitride. *Nature Materials*, 10:1–4, February 2011.

[70] AB Preobrajenski, AS Vinogradov, and N Martensson. Monolayer of h-BN chemisorbed on Cu (1 1 1) and Ni (1 1 1): The role of the transition metal 3d states. *Surface Science*, 582(1-3):21–30, 2005.

[71] Sushobhan Joshi, David Ecija, Ralph Koitz, Marcella Iannuzzi, Ari P Seitsonen, Jürg Hutter, Hermann Sachdev, Saranyan Vijayaraghavan, Felix Bischoff, Knud Seufert, Johannes V Barth, and Willi Auwärter. Boron Nitride on Cu(111): An Electronically Corrugated Monolayer. *Nano Lett*, 12(11):5821–5828, November 2012.

[72] J H Scofield. *Theoretical photoionization cross sections from 1 to 1500 keV*. Lawrence radiation Laboratory., 1973.

[73] Wolfgang S M Werner. Electron transport in solids for quantitative surface analysis. *Surface and Interface Analysis*, 31(3):141–176, 2001.

[74] Cecilia Mattevi, Hokwon Kim, and Manish Chhowalla. A review of chemical vapour deposition of graphene on copper. *Journal of Materials Chemistry*, 21(10):3324, 2011.

[75] Silvan Roth, Juerg Osterwalder, and Thomas Greber. Synthesis of epitaxial graphene on rhodium from 3-pentanone. *Surface Science*, 605(9-10):L17–L19, 2011.

[76] Tanuma S. Electron Attenuation lengths. In David Briggs and John T Grant, editors, *Surface Science Analysis by Auger and X-Ray Photoelectron Spectroscopy*. IM Publications, West Sussex, U.K., September 2003.

[77] C S Fadley. Syncrotron Radiation Research: Advances in Surface and Interface Science. In R Z Bachram, editor, *Syncrotron Radiation Research: Advances in Surface and Interface Science*. Plenum, New York, February 1990.

[78] Jürg Osterwalder. Structural Effects in XPS and AES: Diffraction. In David Briggs and John T Grant, editors, *Surface Analysis by Auger and X-Ray Photoelectron Spectroscopy*. IM Publications, West Sussex, UK, January 2003.

[79] W Auwärter, TJ Kreutz, T Greber, and J Osterwalder. XPD and STM investigation of hexagonal boron nitride on Ni (111). *Surface Science*, 429(1-3):229–236, 1999.

[80] Tomohiro Matsushita, Fumihiko Matsui, Hiroshi Daimon, and Kouichi Hayashi. Photoelectron holography with improved image reconstruction. *Journal of Electron Spectroscopy and Related Phenomena*, 178-179:195–220, May 2010.

[81] Fumihiko Matsui, Tomohiro Matsushita, and Hiroshi Daimon. Photoelectron Diffraction and Holographic Reconstruction of Graphite. *Journal of the Physical Society of Japan*, 81(11):114604, October 2012.

[82] Kwanpyo Kim, Zonghoon Lee, Brad D Malone, Kevin T Chan, Benjamín Alemán, William Regan, Will Gannett, M F Crommie, Marvin L Cohen, and A Zettl. Multiply folded graphene. *Physical Review B*, 83(24):245433, June 2011.

[83] G Grad, P Blaha, K Schwarz, W Auwärter, and T Greber. Density functional theory investigation of the geometric and spintronic structure of h-BN/Ni(111) in view of photoemission and STM experiments. *Physical Review B*, 68(8):085404, August 2003.

[84] P Heimann, J Hermanson, H Miosga, and H Neddermeyer. D-Like Surface-State Bands on Cu(100) and Cu(111) Observed in Angle-Resolved Photoemission Spectroscopy. *Physical Review B*, 20(8):3059–3066, 1979.

[85] Gianluca Giovannetti, Petr A Khomyakov, Geert Brocks, Paul J Kelly, and Jeroen van den Brink. Substrate-induced band gap in graphene on hexagonal boron nitride: Ab initio density functional calculations. *Physical Review B*, 76(7):073103, 2007.

[86] Matthew Yankowitz, Jiamin Xue, Daniel Cormode, Javier D Sanchez-Yamagishi, K Watanabe, T Taniguchi, Pablo Jarillo-Herrero, Philippe Jacquod, and Brian J Leroy. Emergence of superlattice Dirac points in graphene on hexagonal boron nitride. *Nature Physics*, 8(5):382–386, March 2012.

[87] K S Novoselov, A K Geim, S V Morozov, D Jiang, M I Katsnelson, I V Grigorieva, S V Dubonos, and A A Firsov. Two-dimensional gas of massless Dirac fermions in graphene. *Nature*, 438(7065):197–200, November 2005.

[88] Yuanbo Zhang, Yan-Wen Tan, Horst L Stormer, and Philip Kim. Experimental observation of the quantum Hall effect and Berry's phase in graphene. *Nature*, 438(7065):201–204, November 2005.

[89] Simon Berner, Martina Corso, Roland Widmer, Oliver Groening, Robert Laskowski, Peter Blaha, Karlheinz Schwarz, Andrii Goriachko, Herbert Over, Stefan Gsell, Matthias Schreck, Hermann Sachdev, Thomas Greber, and Jürg Osterwalder. Boron Nitride Nanomesh: Functionality from a Corrugated Monolayer. *Angewandte Chemie International Edition*, 46(27):5115–5119, July 2007.

[90] Silvan Roth, Fumihiko Matsui, Thomas Greber, and Jürg Osterwalder. Chemical Vapor Deposition and Characterization of Aligned and Incommensurate Graphene/Hexagonal Boron Nitride Heterostack on Cu(111). *Nano Lett*, 13(6):2668–2675, June 2013.

[91] S Kono, S M Goldberg, NFT Hall, and C S Fadley. Chemisorption geometry of c (2 2) oxygen on Cu (001) from angle-resolved core-level x-ray photoemission. *Physical Review B*, 22(12):6085, 1980.

[92] Jingguang G Chen, Bernd Frühberger, Joseph Eng, Jr, and Brian E Bent. Controlling surface reactivities of transition metals by carbide formation. *Journal of Molecular Catalysis A: Chemical*, 131(1):285–299, 1998.

[93] Guocai Dong and Joost W M Frenken. Kinetics of Graphene Formation on Rh(111) Investigated by In SituScanning Tunneling Microscopy. *ACS Nano*, 7(8):7028–7033, August 2013.

[94] Kevin F McCarty, Peter J Feibelman, Elena Loginova, and Norman C Bartelt. Kinetics and thermodynamics of carbon segregation and graphene growth on Ru(0001). *Carbon*, 47(7):1806–1813, June 2009.

[95] Choongyu Hwang, Cheol-Hwan Park, David A Siegel, Alexei V Fedorov, Steven G Louie, and Alessandra Lanzara. Direct measurement of quantum phases in graphene via photoemission spectroscopy. *Physical Review B*, 84(12):125422, September 2011.

Acknowledgements

I would like to thank all the people who contributed to this work or helped along the way. First of all I would like to thank Jürg Osterwalder and Thomas Greber for giving me the opportunity to carry out this thesis. I profited a lot from your guidance, your great experience, and your constructive criticism. I'm thankful for Jürg's encouraging way of seeing the glass as half full instead of half empty, and Thomas's unconventional and cool ideas which lead me out of many dead ends.

Special thanks also go to Oliver Gröning for joining my PhD comity and his helpful inputs during this time.

I would like to thank the surface science group with all their present and former members, who helped my through my thesis. First off all, Matze for introducing me to a real lab for the first time, for hundreds of coffee breaks with thousand ideas, and for cheering me up when necessary.

I would like to thank the people I shared long beam times with, unfortunately we couldn't carry out all the cool experiments we had in mind. Thanks Adrian Hemmi, for showing me during our beamtime what a miserable life is and that mine is still better. Dominik Leuenberger for the probably best team work I've ever experienced, and Huanyao Cun for her endless endurance carrying out difficult experiments.

I like to thank the Laser Lab team, Luca, Michl, Adrian, and Hiro for the good time, lots of good talks about physics and unfortunately a lot about physical injuries. A very special thanks goes to Fumihiko Matsui. Dear Fumihiko, your input was great for the paper. Thanks also to the over motivated former master students and now PhDs Roland and Carlo. Thank you for the programming lesson Roland. Thank you Gerson for taking over ESCA, I think the machine is in good hands. The technical support from Thomas Kälin and Martin Klöckner made it possible to carry out this thesis, I'm very thankful for all this support. A special thanks goes to the Cophee people, Hugo, Bartosz, Fabian and Stefan for inspiring conversations.

At last, I would like to thank the whole physics institute for creating this nice place and environment during my time at Irchel.

Outside of physics I had good friends accompanying me during this time, Raph and Gion. Thank you guys for a great time.

Curriculum Vitae

Name	Silvan Roth
Birth	24.12.1979 in Olten (SO), Switzerland
Nationality	Swiss

Education

since 10/2009	PhD studies of *“Graphene on Metal Surfaces and Hexagonal Boron Nitride”* in the Surface Physics Group of Prof. Dr. J. Osterwalder, University of Zurich, Switzerland
07/2008	Master of Science degree in Physics, University of Zurich, masters thesis: *“Time-resolved Two-Photon Photoemission on Tertamantane Monolayers’”*
09/2007	Bachelor of Science degree in Physics, University of Zurich, bachelor thesis: *“Alignment and Characterisation of an Optical Parametric Amplifier”*
2006 - 2008	Advanced studies in theoretical and experimental physics, University of Zurich
2002 - 2006	Undergraduate studies in physics, mathematics and astronomy, University of Zurich
03/2001	Eidgenössische Matura, Typus-C

Working Experience

10/2009 - 12/2013	Research assistant in the group of Prof. Dr. Jürg Osterwalder, University of Zurich
09/2008 - 09/2009	Research assistant for fiber laser development and laser material processing at inspire AG, Zurich
09/2008 - 09/2009	Lecture assistant and Tutor for laboratory courses and problem solving classes, Physics Institute, University of Zurich
since 2013	Referee for ACS Nano of the American Chemical Society

Publications

1. **S. Roth**, F. Matsui, T. Greber, and J. Osterwalder, *Chemical Vapor Deposition and Characterization of Aligned and Incommensurate Graphene/Hexagonal Boron Nitride Heterostack on Cu(111)*, Nano Lett. **13**, 2013
2. **S. Roth**, J. Osterwalder and T. Greber, *Synthesis of epitaxial Graphene on Rhodium from pentanon*, Surface Science **605**, 2011
3. **S. Roth**, D. Leuenberger, J. Osterwalder, J.E. Dahl, R. M. K. Carlson, B. A. Tkachenko, A. A. Fokin, P. R. Schreiner, and M. Hengsberger *Negative-electron-affinity diamondoid monolayers as high-brilliance source for ultrashort electron pulses*, Chemical Physics Letters **495**, 2010
4. H. Cun, M. Ianuzzi, A. Hemmi, **S. Roth**, J. Osterwalder, and T. Greber *Immobilizing Individual Atoms beneth a Corrugated Single Layer of Boron Nitride*, Nano Letters **13**, 2013
5. D. Leuenberger, H. Yanagisawa, **S. Roth**, J.H. Dil, J.W. Wells, P. Hofmann, J. Osterwalder, and M. Hengsberger *Excitation of coherent phonons in the one-dimensional Bi(114) surface,* Physical Review Letters **110**, 2013
6. L. Castiglioni, M. Greif, D. Leuenberger, **S. Roth**, J. Osterwalder, and M. Hengsberger *Time-Resolved Photoelectron Spectroscopy to Probe Ultrafast Charge Transfer and Electron Dynamics in Solid Surface Systems and at Metal- Molecule Interfaces*, CHIMIA International Journal for Chemistry **65**, 2011
7. D. Leuenberger, H. Yanagisawa, **S. Roth**, J.Osterwalder, and M. Hengsberger *Disentanglement of electron dynamics and space-charge effects in time-resolved photoemission from h-BN/Ni(111)*, Physical Review B **84**, 2011
8. M.Greif, L. Castiglioni, A. Seitsonen, **S. Roth**, J. Osterwalder, and M. Hengsberger *Photoelectron diffraction in the x-ray and ultraviolet regime: Sn-phthalocyanine on Ag(111),* Physical Review B **87**, 2013
9. H. Enriquez, A. Mayne, A. Kara, S. Vizzini, **S. Roth**, B. Lalmi, A. P. Seitsonen, B. Aufray, T. Greber, R. Belkhou, G. Dujardin, and H. Oughaddou, *Adsorption of silicon on Au(110): An ordered two dimensional surface alloy*, Appl. Phys. Lett.**101**, 2012
10. H. Ma, M. Thomann, J. Schmidlin, **S. Roth**, M. Morscher, T. Greber, *Corrugated single layer templates for molecules: From h-BN Nanomesh to Graphene based Quantum dot arrays,* Front. Phys. China, **5**, 2010